Modelling polycrystalline materials and interfaces

Jonathan Bean

PhD

University of York
Physics

August 2017

Abstract

Polycrystalline materials are ubiquitous and dominate the synthetic and natural worlds. They are characterised by the presence of defects such as grain boundaries in the crystal structure. Grain boundaries can significantly influence underlying electrical, magnetic and mechanical properties of materials.

In this thesis interatomic potentials have been used to model grain boundaries in Fe, Cu and Ni. A high throughput computational approach is employed to determine the atomic structure, formation energy and excess volume of a large number of tilt grain boundaries in Fe, Cu and Ni. There is a systematic difference of $\sim$0.2 Å between the excess volumes in Cu and Ni which is in agreement with experiment. It is predicted that the differences in the elastic moduli may give rise to larger differences in excess volume than expected.

Novel plan-view high-resolution transmission electron microscopy and first principles calculations have been employed to provide atomic level understanding of the structure and properties of grain boundaries in the MgO barrier layer of a magnetic tunnel junction. Transmission electron microscopy images reveal grain boundaries in the MgO film including (210)[001] symmetric tilt grain boundaries and (100)/(110)[001] asymmetric tilt grain boundaries amongst others. First principles calculations show how these grain boundaries are associated with locally reduced band gaps (by up to 3 eV).

The knowledge from the modelling of Fe, Cu, Ni and MgO is used to study interfaces of Fe and MgO to further understand magnetic tunnel junctions. The orientational relationship between the Fe and MgO is not known explicitly. Density functional theory is used to predict the energetic stability of Fe/MgO interfaces in different orientational configurations. It is found that the most energetically favourable interface between Fe and MgO is when the atomic columns are in registry.

If you don't sell something that doesn't exist,

it will never exist.

Salesperson's paradox
S. McCamley

This thesis is dedicated to all
of the people who have believed
in me over the years.

Contents

List of Figures

Acknowledgements

First and foremost I must thank my supervisor Keith McKenna, he has been like a rock and gone above and beyond what he needed to do in order to for me to succeed. I cannot produce the words necessary to thank him for his kindness and support over the last 4 years. I would also like to thank Rex Godby for interesting physics conversations in the senior common room and for listening to me in times of need. My thanks also go out to Phil Hasnip and Matt Probert for helping me with CASTEP and for organising interesting condensed matter theory seminars. In York each PhD student is given a thesis advisory panel (TAP) to provide challenge and to provide a different research perspective on each students research. My TAP member was Christopher Ridgers who is usually placed in the York plasma institute. He provided a unique insight into my research and helped me understand the structure of a thesis.

During my PhD I have held several positions where I have required to inter-act with the administration staff more than usual and I would like to thank the individual members as they were always kind and helpful to me. In the finance office there is Anne Stroughair who managed most of the payments both for teaching and purchases. She also let me use the fridge to store things for the postgraduate gatherings. There is also Tami who manages most of the undergraduate teaching. Tami has an encouraging view on management and promotes positive working values in the department. I would also like to thank Jacqui, Jane, Judith, Erica and Lauren. These guys are the lifeblood of the department and would not operate without them. I must also thank John Pasley and Mike Bentley for giving me the role of graduate teaching coordinator, a role I thoroughly enjoying doing. Also now Erik and James are taking over. I would like to thank Steve Biggs and Nicola Farthing for

taking up the mantle of postgraduate representation they are both doing a great job! I must thank/ apologise to Sarah Thompson and Alison Laird who I inundated with questions and ideas for the department, they always had time for me and other postgraduates. I cannot leave out Lydia Aarons who was the previous postgraduate administrator. Lydia was a lovely woman who was always kind and supportive. Her presence is missed in the department. I would also like to thank the guys in stores (Warren and Chris) who always were on hand to sort any stationary and other office supply related issues. I would like to thank Phil Lightfoot who is the graduate training coordinator and previous postgraduate teaching coordinator. He is an excellent Lecturer and extremely dedicated to his work. I would also like to convey my appreciation to WorMzy, Simon Hart and Matt Pickin for IT support. WorMzy is a boss with Linux, I'm pretty sure he has made commits to the Linux Kernel. I must also thank Christian Diget for letting me do my skydiving talk at the teachers conference and engaging in interesting conversations in the senior common room.

I would like to thank Richard Evans and Roy Chantrell whom I have been collaborating with for the past two years. They always provide for a stimulating discussion and have new perspectives on things. I would also like to thank my collaborators in Japan including Mitsuhiro Saito, Atsufumi Hirohata for financing the trip and the other guys in Japan for providing me with an amazing opportunity. I would like to specially thank Mitsuhiro Saito who came up specially to see me in Sendai when I was in Japan. I did also have the privilege of walking past Kevin O'grady's office everyday. I also wish to thank my colleagues and friends from office N001 for physics related and non-physics related discussion, and for each contributing to such a warm and positive working environment.

I would also like to thank my wonderful friends in which there are many including: Doris, Paolo, Cleany, Liz and co Layi and co, Jenny, Stu, Ollie, Louis, Rupert, Mike and the Jack. I would also like to thank the various sports teams I was part of including: Fencing, Archery, Football, Badminton, MMA, Chess, Skydivers and climbing. The McKenna research group has

Declaration

I declare that all the work is my own except transmission electron microscopy images and transmission electron microscopy image simulations which have been performed by Mitsuhiro Saito, Shunsuke Fukami, Hideo Sato, Shoji Ikeda, Hideo Ohno and Yuichi Ikuhara in Japan. I declare that this thesis is a presentation of original work and I am the sole author. This work has not previously been presented for an award at this, or any other, University. All sources are acknowledged as References.

List of publications

1. Bean, J. J., McKenna, K. P. (2016). Origin of differences in the excess volume of copper and nickel grain boundaries. Acta Materialia, 110, 246257. https://doi.org/10.1016/j.actamat.2016.02.040

2. Bean, J. J., Saito, M., Fukami, S., Sato, H., Ikeda, S., Ohno, H., Ikuhara, Y., McKenna, K. P. (2017). Atomic structure and electronic properties of MgO grain boundaries in tunnelling magnetoresistive devices. Scientific Reports, 7(January), 45594. https://doi.org/10.1038/srep45594

Chapter 1

Introduction

1.1 Polycrystallinity

Our current model of the microscopic Universe theorises elementary particles of matter such as the electrons and the quarks as the smallest building blocks. These building blocks interact through forces mediated by other particles known as the gauge bosons; such as the $W^{\pm}, Z^0$, photons and the gluons. These forces are known as the weak, electromagnetic and the strong forces respectively and enable the formation and destruction of larger structures known as atoms. This description is known as the standard model and encompasses the theories of quantum mechanics and quantum field theory. These beautiful theories are the most accurate and testable descriptions of nature created to date. In contrast to understanding isolated particles and atoms the physics of materials concerns itself with understanding atomic superstructures. Superstructures are large collections of atoms (often 10^{23} and greater). Superstructures form everyday things in our local environment such as trees, laptops, cars and houses. Materials physics represents a completely different kind of challenge to the physicist as the goal is not to explain everything with a single equation (a theory of everything) but to provide insight with the knowledge that symmetry has been violated. In other words if armed with only the equations of nature predicting the properties of materials would be impossible. Materials physics has impacted our society significantly in the past century, with a significant proportion of Nobel prizes in physics and chemistry being awarded [1, 2]. Materials physics attracts a significant amount of research investment via government funding agencies and multi-national companies [3–5].

Materials span the range between perfectly amorphous and perfectly crystalline. Although this thesis is not concerned with amorphous materials a brief discussion will be given. Perfectly amorphous materials are collections of atoms and/or molecules which exhibit no long range order[1]. This is interesting because although there may be symmetry locally there are global properties which are characteristic of this material class. Although the atomic arrangement of the atoms appears to be random, it is possible to analyse these materials using the radial distribution function $g(r)$. The radial distribution function is the probability of finding another atom as a function of radial distance (See Fig. 1.1). The radial distribution function shows that there are certain bond orders which are preferred, such as the first nearest neighbour distance. The reader is directed to [6] for more information on amorphous materials.
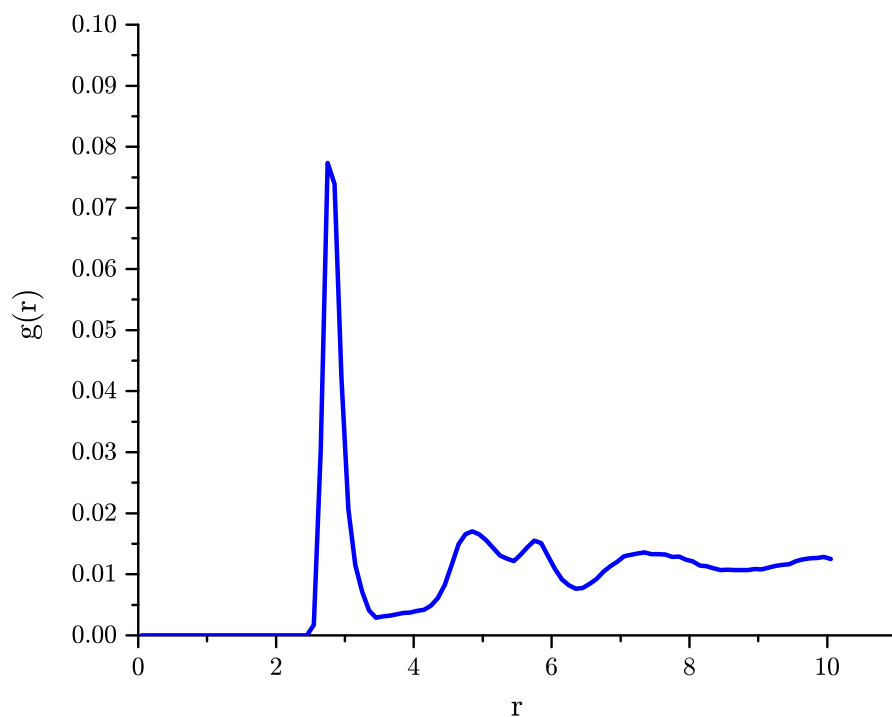
Figure 1.1: Radial distribution function for metallic glass ZrCuAg. Result of MD simulation for 16000 particles in cubic supercell with periodic boundary conditions.

[1]Usually of the order of over 5 Å.

A concept known as a Bravais lattice is used to describe crystalline materials. The Bravais lattice specifies a periodic repetition of points in space. Mathematically the Bravais lattice is given as $\mathbf{R} = n_1\mathbf{a}_1 + n_2\mathbf{a}_2 + n_3\mathbf{a}_3$, where $\mathbf{a}_i$ are any three lattice vectors not in the same plane and n_i are integers which specify the lattice position. A unit cell can be then defined as a volume which if translated by any of the Bravais lattice vectors does not cause any overlapping with subsequent regions. To complete the description of a crystal a basis is introduced which describes what atoms and/or molecules are present in the unit cell and at which fractional positions.

This thesis is concerned with two main types of crystals which are atomically bonded in very different ways: metals (metallic bonding) and metal-oxides (ionic bonding)[2]. In metals the electronic structure is described as positive charges (ions) in a lattice which are surrounded by a sea of delocalised electrons. In metals there is no band gap, which means that electrons are free to move between states above and below the Fermi energy (the highest occupied state at 0K). In metals electrons are free to move between atoms, this gives rise to high electrical and thermal conductivity. Ionic crystals contain two or more elements. In an ionic crystal a more stable energetic configuration is be found via polarisation of the elements into positive and negative ions. Ionic bonding arises from the electrostatic (Coulomb) potential between positive and negative ions in a crystal. The attractive force between the positive and negative charges is balanced by the repulsive force between the orbital electrons and the repulsion between similar ions.

Rather than containing an infinite periodic arrangement of lattice points and a basis real crystals contain a series of arbitrarily orientated crystals known as grains. Materials formed from grains are known as polycrystalline and the interfaces between the grains are known as grain boundaries (GBs). The size of the grains can vary quite significantly from a few cms to tens of nms. Predictably the properties of materials can change quite significantly between these two length scales. For example as the grains are made smaller the strength of the material increases [7–10]. The Hall-Petch equation describes how the strength of a material changes with grain size,

---

[2]It is possible for either metallically or ionically bonded crystals to posses covalently bonded properties.

$$\sigma_0 = \sigma_i + \frac{k}{\sqrt{D}}, \tag{1.1}$$

where σ_i is the frictional stress (the resistance to dislocation motion), σ_0 the strength of a metal, k is the strengthening constant specific to each material and D is the grain size. Interestingly as metals are made nanocrystalline (grains are of the order of nanometres in length) this behaviour appears to invert resulting in a softening of a material [11].

Fig. 1.2 shows an example of a commonly occurring polycrystalline material. The image is taken with an optical digital single-lens reflex (D-SLR) camera. The material is known as hot dip galvanized steel with zinc as the galvanizing agent, it is commonly used for lampposts and railings. The grains also known as spangles are comprised of pure zinc in eta (η) phase. A very thin layer of ZnO forms on the zinc when exposed to the atmosphere protecting the zinc underneath from further corrosion [12].

Figure 1.2: Image of a zinc galvanized steel sheet taken with a digital single-lens reflex camera. Large grain boundaries (~ 0.5 cm) are visible from the difference in reflection at the surface of the metal.

Important advances in the study of polycrystallinity were achieved by Henry Clifton Sorby who was one of the first scientists to optically image metals. In Clifton's experiments metals such as copper and steel were initially etched, polished then imaged using an optical microscope [13,14]. The etching removes the oxide layer which forms on most metals. The oxide layer does not necessarily grow epitaxially on the metal and hence grains in the metal can be hidden. The experiments revealed GBs, dislocations and other defects. In optical microscopy there is a fundamental limit to the resolution arising from the level of diffraction which occurs when atoms are bombarded by an incident light beam. The resolution limit of optical microscopy means that atomic structures cannot easily be resolved. This limit is given with respect to the size of the smallest feature d and can be approximated using the following formula,

$$d = \frac{\lambda}{2NA},$$ (1.2)

where λ is the wavelength of the incoming ray and NA is the numerical aperture of the lens[3]. The only way the resolution can be increased using photons is to decrease the wavelength of the incident beam. As the wavelength becomes small the incident particles will begin to pass right through the sample without interaction (such as high energy gamma rays). To solve this problem rather than using photons, electrons can be used. The wavelength of an electron (λ_e) is given as,

$$\lambda_e = \frac{h}{\sqrt{2m_e E \left(1 + \frac{E}{2m_e c^2}\right)}},$$ (1.3)

where h is Planck's constant, E is the electron energy and m_e is the rest mass of the electron. Electron microscopes have been shown to be able to resolve structures down to 60 pm [15]. In atomic modelling it is of vital importance to compare to experiments in order to validate results. Electron microscopy is the perfect partner to computational calculations since it can atomically resolve structures of many materials and devices. Using scanning transmission electron microscopy (STEM) it has been possible to atomically resolve dislocations, interfaces and GBs in MgO thin films [16–18].

---

[3]The numerical aperture is a measure for how much light a given lens can receive.

A first course in solid state physics may give the impression that materials are more perfect than they really are. The idea of a single crystal may come from our human belief that perfection can be achieved. It is actually a general observation that most materials are in fact polycrystalline with only a small number of materials being single monocrystalline or amorphous. To demonstrate why materials are polycrystalline an Atomix is shown in Fig. 1.3. Atomix is a piece of art created originally by François Dallegret in 1963 which I recreated to showcase the problem of polycrystallinity to the general public. It consists of 10,000 ball bearings one ball bearing deep encased in perspex. When the Atomix is illuminated one can see the existence of the granular structure. No matter how hard you try it is impossible to get all of the atoms to line up as a single crystal. Using different shapes such as a hexagon or a circle can change the nature of the grains in the structure.

Figure 1.3: Atomix: 10,000 steel ball bearings encased in a perspex block simulates the polycrystalline nature of materials. The numbers of bearings by height, depth and width are approximately 100×1×100 respectively.

In well designed experiments it is possible to control the production processes of materials so precisely that monocrystalline materials can be created. An example of creating an almost defect free material is the famous iron whisker. An iron whisker is formed by carefully growing iron atoms layer by layer to ensure that it is almost defect

free. This results in an extremely high tensile strength and high elasticity but can only be made in small quantities [19]. It is not easy to manufacture materials at industrial scales without defects[4] but it is possible to control the nature of defects and how they interact with each other to tune the properties of materials. In this light near-single crystals can be produced at an industrial scale in the manufacture of aeroplane turbine blades. In the manufacturing process of the turbine blades molten material is put through a grain selector which forces the material into a single crystallographic orientation. The resulting material is very strong and elastic [20, 21]. Monocrystallinity is important for this application as turbines undergo intense heat and stress whereby failure would result in catastrophe. The removal of the GBs increases the creep life and the melting temperature as GB strengthening elements can be removed. The single crystals present in turbine blades usually contain other phases and precipitates.

It is an inevitability that defects will occur so it is a requirement that scientists understand how these defects affect mechanical and electrical properties. In many cases defects such as GBs are the reason for failure or diminished properties in materials. The industrial drive to miniaturise components such as transistors is dependent on understanding these defects since as devices become smaller the effect of the defects on the structure becomes more and more significant. Minimisation also brings a further problem as it becomes more difficult to perform accurate experimental measurements on smaller and smaller devices. Computational calculations are required to provide insights into the geometric, mechanical, electronic and magnetic properties.

There has been a significant amount of activity around the material graphene with claims that this material could be used in a space elevator. Evidently this raises the problem with comparing predictions and measuring capabilities. It is almost impossible to create a significant length of graphene which is defect free. As soon as defects appear in any significant number the wonder properties of this material rapidly decrease [22]. It has also been shown what happens when the properties of GBs are not considered. In 1969 a turbine rotor failed during an over speed test at Hinkley point A nuclear reactor. The reason for the failure was down to transport of phosphorus towards the GBs which embrittled the chromium steel causing it to fail [23–26]. Embrittling of steel can have disastrous consequences. In the sinking of the titanic it is thought that the low fracture toughness of the steel used embrittled the material [27, 28].

---

[4]With some exceptions like silicon wafer.

1.2 Computational modelling of materials

In many situations it is extremely difficult and sometimes impossible to perform experiments which are informative. For example probing the mechanical and electronic properties of atomically buried structures within transistors or the complex processes which occur in nuclear reactors. The reason why experiments are not often informative can be down to the inability to probe a region of interest, insufficient resolution or a large degree of experimental noise. It is possible to use computational modelling to both understand experiments further and provide explanations for circumstances when experiments cannot be performed.

To model materials first a description of the interactions between the atoms in a system of interest should be defined. Most computational methods describe the interactions between the atoms via an interatomic potential (classical) or by solving an approximate form of the many body Schrödinger equation (quantum mechanical). One method which uses an interatomic potential is called the embedded atom method (EAM). The EAM is a classical total energy method which postulates a functional form which describes the potential energy between the atoms as a function of atomic separation. The EAM is usually parameterised against experimental measurements such as the lattice constant, elastic moduli, phonons and vacancy formation energies [29, 30]. The EAM has been shown to work well for the modelling of metals [31–34]. The two quantities which can be extracted from classical simulations are the total energy and the optimised atomic positions. From the total energy and atomic positions a large range of properties such as the formation energies of defects, strain, tensile strength and elastic moduli can be determined. One of the problems with interatomic potentials is that the degree of transferability is very low e.g. the EAM cannot easily be used to compute properties of metals and metal-oxides simultaneously. Although more complex forcefields such as the charge optimised many body (COMB) potential exist, they have not been shown to be completely reliable and require more development [35]. Classical simulations are limited by the total number of atoms which can realistically be represented but can still model large defect structures including GBs. Quantum mechanical methods such as density functional theory (DFT) approximate the Schrödinger equation. DFT is far more transferrable than interatomic potentials in that it does not need to be parameterised so can model systems such as the Fe/MgO interface extremely well. DFT gives access to more

information such as the density of states, band structure and more so many materials properties can be compared to experiment [36, 37]. The big drawback to quantum mechanical methods is that they are very computationally expensive so large structures cannot be simulated.

After the description of the atomic interactions has been completed and validated a representative model of a system of interest should be created. Symmetry is an important consideration as it allows the simplification of a problem to only the irreducible variables. A careful balance to ensure that and system is well described physically and computational feasibility needs to be considered when creating models.

The final step is to optimise the geometric positions of the atoms. During the optimisation process the atomic positions and/or simulation cell is adjusted to lower the total energy of a system towards a minimum. After the optimisation process is completed the physical properties can be calculated. Although the process of modelling materials at first glance appears to be simple it is a challenging task to design simulations to provide useful insights. Simulations should be rigorously tested to ensure that the interatomic bonding between the atoms accurately describes the physics of interest. The models created also need to be sufficient to test the quantity of interest. Many computational simulations are compared to experiment or less approximate methods (such as DFT) to validate them. Computational studies are only limited by the accuracy of the equations used to describe the interactions between atoms and the number of degrees of freedom.

1.3 Aims of this thesis

The aim of this thesis is to model a range of different polycrystalline materials using classical and quantum mechanical methods. Insights from the models are then used to inform and explain experimental observations in the context of excess volume measurements in metals and magnetic tunnel junctions which are comprised of metals and metal-oxides.

A key property in understanding GBs is the excess volume which is thought to influence the degree of segregation and resistivity of metals [38–41]. The excess volume is defined as the increase in volume per unit area. Understanding the excess volume is extremely important in materials design and in applications such as nuclear reactors. The excess volume however is extremely difficult to measure experimentally and only a

handful of metals (Cu and Ni) have been directly measured [42, 43]. Previous computational studies have explored the excess volume of GBs but an atomistic interpretation of the excess volume is currently missing [44]. In fact there are relatively few computational studies which focus on the excess volume of GBs in general. In the first results chapter (chapter 4) the differences between the excess volume (a property of GBs see Sec. 2.1.3) of symmetrical tilt GBs in Fe, Cu and Ni is investigated. For each metal stable structures for symmetrical tilt GBs are found using the EAM. From the stable structures the excess volume is determined. DFT is used for a small subset of GBs to validate the models. The EAM results may be aggregated to compare against experimental measurements of the excess volume for Cu and Ni. This computational and experimental comparison reveals that the gradients of the interatomic potentials away from equilibrium can largely influence the excess volumes of Cu and Ni.

A key application relevant to this thesis where the understanding of GBs and polycrystallinity is paramount is in magnetic tunnel junctions. A magnetic tunnel junction (MTJ) is an electronic device that either inhibits or promotes the tunnelling of electrons through a non-magnetic insulating barrier dependent of the magnetisation of two surrounding ferromagnets [45–47]. An example MTJ stack structure is shown in Fig. 1.4.
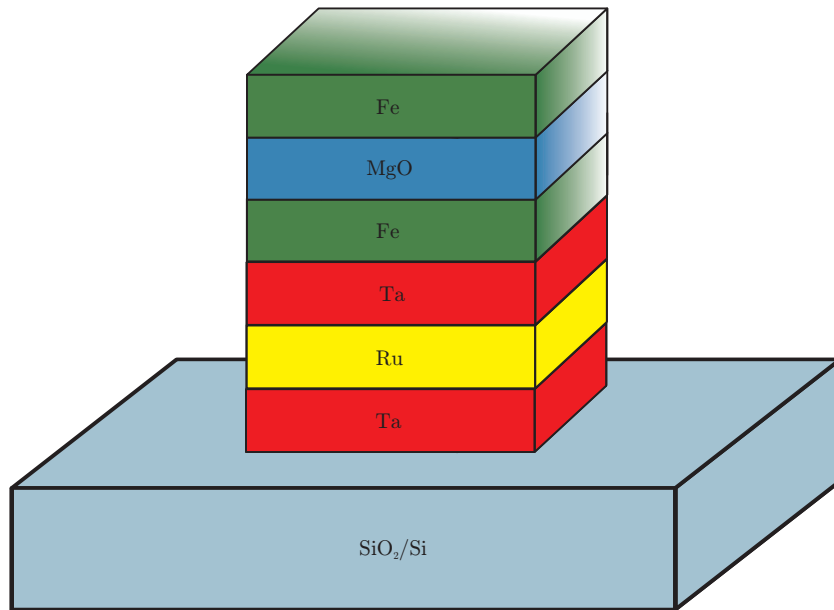
Figure 1.4: Schematic showing the stack structure of a simple Fe/MgO/Fe magnetic tunnel junction.

An MTJ can be described by a two current model where the spin currents of the spin up and spin down electrons conduct in parallel. When the magnetisation of both ferromagnets are parallel the conductance is given as $G^P = G^{\uparrow\uparrow} + G^{\downarrow\downarrow}$ as the spin up electrons are transferred from a spin up region to a spin up region whereas when the magnetisation of one ferromagnet is anti-parallel the conductance is $G^{AP} = G^{\downarrow\uparrow} + G^{\uparrow\downarrow}$. In the anti-parallel state the conductance will be lower as the electrons in both conducting channels find themselves in a region of opposite magnetisation. MTJs form the basis of a new memory called spin transfer torque magnetic random access memory (STT-MRAM). STT-MRAM uses a spin torque generated by spin polarised electrons which are injected into the MTJ to change the magnetic alignment of the ferromagnetic electrodes thereby switching the conductance state. MTJs are non-volatile, have high switching speeds and are likely to offer many improved benefits over existing memory technologies [48, 49]. As memory is the currently the largest bottleneck in modern day computing increased switching speed could improve computational performance. The performance of MTJs is often characterised by the tunnelling magneto-resistance (TMR) [49, 50]. Theoretically the formula to determine the TMR is given as,

$$\text{TMR}_{\text{eff}} = \frac{G^{\text{P}} - G^{\text{AP}}}{G^{\text{AP}}}. \tag{1.4}$$

For a magneto-memory to be viable it requires a high value of the TMR.

Julliere performed the first experiments which illustrated the TMR effect, these were conducted on an Fe/GeO/Co interface [51]. Julliere's experiments were performed at 4.2 K and only demonstrated an effect of 14%. At a such a low temperature it would be difficult to create useable memory devices. Higher magneto-resistances have been detected using Al_2O_3 as the insulating barrier [52]. Even higher magneto-resistances have been found using Fe as the electrodes and MgO as the insulating barrier as shown by Yuasa, Parkin and Zhang [53–55]. The best devices in the world currently use FeCoB as the electrodes and have detected TMRs as large as 604% in MTJs at room temperature [56].

In the second results chapter (Chapter 5) STEM images of the MgO layer within magnetic tunnel junctions captured by our collaborators in Japan have been analysed. The novel plan-view images atomically resolve the MgO layer revealing the polycrystalline nature of the MgO films. The STEM images are used to build theoretical models

of MgO GBs within the MTJ. Although it has been speculated that the presence of GBs may diminish the insulating properties of the films an atomistic explanation of this is currently missing. DFT calculations are performed on the optimised MgO GB structures and the density of states is extracted. It is predicted that the band gap of the MgO will be reduced at GBs. The reduction in band gap is likely because the local electrostatic potential is diminished at the GB due to reduced symmetry. Thus the GB behaves like an electron trap which promotes GB states at the bottom of the conduction band. A reduction in the band gap of MgO may cause short circuit tunnelling paths through the device. Short circuit tunnelling paths could be diminishing the TMR of devices.

In the final chapter (Chapter 6) interfaces between Fe and MgO are investigated to understand the relationship between interface orientation and energetic stability. Four different scenarios are investigated to understand the orientational relationship between GBs in Fe and/or MgO. It is predicted that the most stable interfaces will be those where the Fe and MgO atomic columns are in registry as repulsive forces arise from the Fe-Mg bond are smaller in these cases.

Chapter 2

Background

In modern materials physics the underlying behaviour of material properties is often controlled by the presence, formation and motion of defects. There are many types of defects which may be present in polycrystalline materials which can be classified by their dimensionality e.g. 0D (point defect), 1D (dislocation), 2D (GB), 3D (void). To highlight the popularity of the study of polycrystallinity a Google N gram search has been performed. A Google N gram calculates the relative frequency distribution of words (grams) in 4% of books published between 1500 and 2008 [57]. Google N gram also looks for stems of words and adds them to the distribution e.g. a search for polycrystalline also will contain polycrystallinity. Google N gram searches have the option to be case sensitive or case insensitive. A gram is a word hence N gram where N is an integer (so N words) thus making it possible to search for phrases. The result of searching for the grams: thin film, grain boundary and polycrystalline is shown in Fig. 2.1.
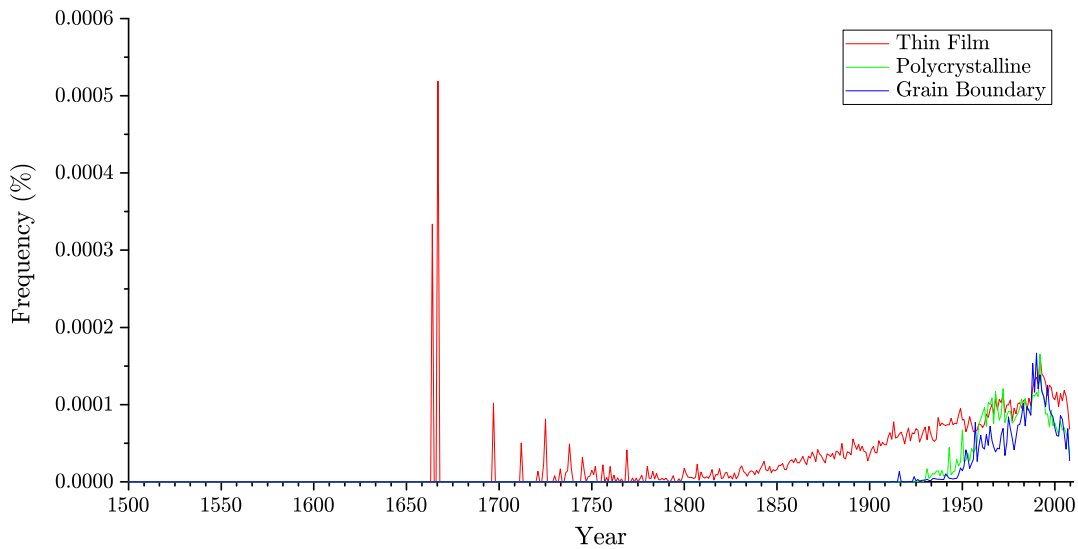
Figure 2.1: Google N gram case insensitive search showing the time dependence of the relative popularity of the grams: thin film, grain boundary and polycrystalline in 4% of books published between 1500 and 2008.

It is noted that there are large spikes which appear in the late 1600s. This is an anomaly of the dataset as the types of people who could read and write and their nature was very different thus the types of books published were different. The Google N gram suggests that the study of polycrystalline materials, defects and GBs first started between 1940 and 1950. An academic literature search confirms the Google N gram result (see Fig. 2.2). The first paper appears in 1920s by R. S. Archer with a flurry of other works by Miller, Zener and Mott to name a few [58–61]. The study of polycrystallinity has expanded since 1950 with rapid progress in experimental characterisation, theoretical models and computational simulation. There have been a plethora of different theoretical and experimental techniques which have been developed and implemented to understand and model polycrystalline materials. These include experimental characterisation using electron microscopy techniques such as electron energy loss spectroscopy to understand the chemical composition of samples or scanning tunnelling microscopy (STM) to probe surfaces [17, 62]. There are also theoretical methods which allow static and dynamical properties of materials to be predicted such as DFT or the EAM.
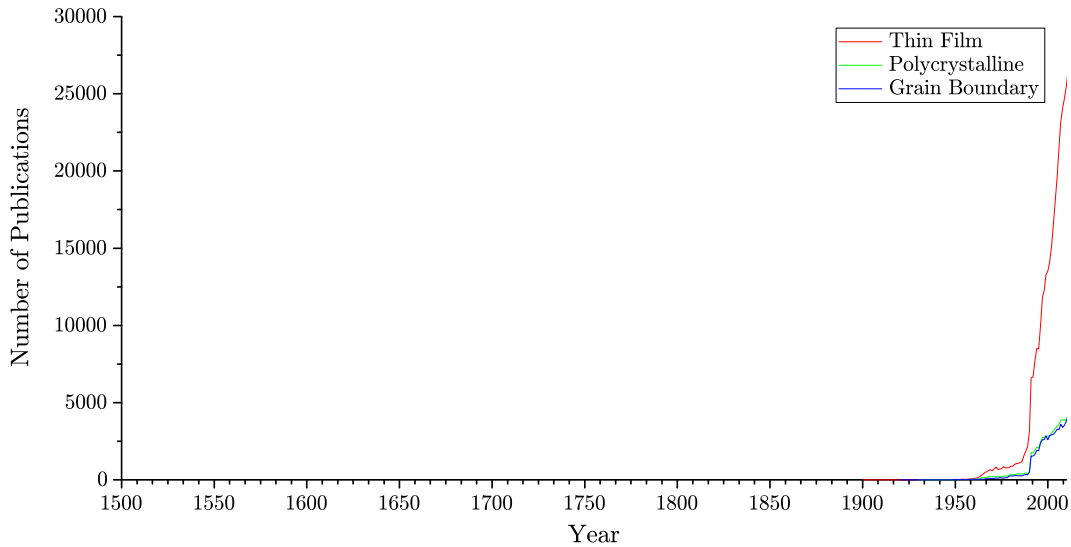
Figure 2.2: Web of Science academic literature search for the keywords: thin film, grain boundary and polycrystalline by number of publications per year.

In this chapter background information related to the results chapters will be discussed. This in effect is a literature review of polycrystallinity and its consequences in applications. As this thesis is concerned with the atomistic modelling of GBs a detailed discussion of finite element and continuum models will be omitted but the popular methods will be discussed as they are relevant even to atomistic modelling.

The chapter is structured into three parts. The first reviews the geometrical definition of GBs (Sec. 2.1.1). The second details the theoretical and experimental work undertaken on metals related to this thesis (Sec. 2.2). The final section describes some of the theoretical and experimental work which has been done on metal-oxides (Sec. 2.3).

2.1 Modelling polycrystallinity

2.1.1 Geometric definition of grain boundaries

Most materials are polycrystalline and are constructed from an assembly of crystallographic grains. Individually the arrangement of atoms within grains can be described using a Bravais lattice supplemented with basis (see Sec. 1.1) [63]. Mathematically it has been shown that there are 14 distinct Bravais lattices (in 3D) [64]. The materials considered in this thesis are body centred cubic (bcc) or face centred cubic (fcc). The

conventional bcc crystal system contains two basis atoms; one at the corner of the unit cell and one at the centre (see Fig. 2.3a). The conventional fcc crystal system contains four basis atoms; one at the corner of the unit cell and three on the faces of the cube (see Figs. 2.3b & 2.3c). The difference between bcc and fcc phases is based on the difference in distance between the nearest neighbours of the two structural phases ($NN_{\text{bcc}} = \frac{\sqrt{3}}{2}a_{\text{bcc}}$ and $NN_{\text{fcc}} = \frac{\sqrt{2}}{2}a_{\text{fcc}}$). Note the difference in the lattice constants of the fcc and bcc phases. In many computational calculations periodic boundary conditions (PBCs) are used. PBCs create an infinite representation from a smaller model of a system. Using PBCs is advantageous as it is possible to easily create a system of one Cu atom which is repeated periodically in all directions becoming effectively infinite, significantly reducing the number of degrees of freedom in a system. The big drawback of PBCs is that the interacting periodic images may introduce unphysical effects as it constrains the possible number of ways a system can relax. The interaction of periodic images is important for defect calculations but unimportant for bulk calculations.
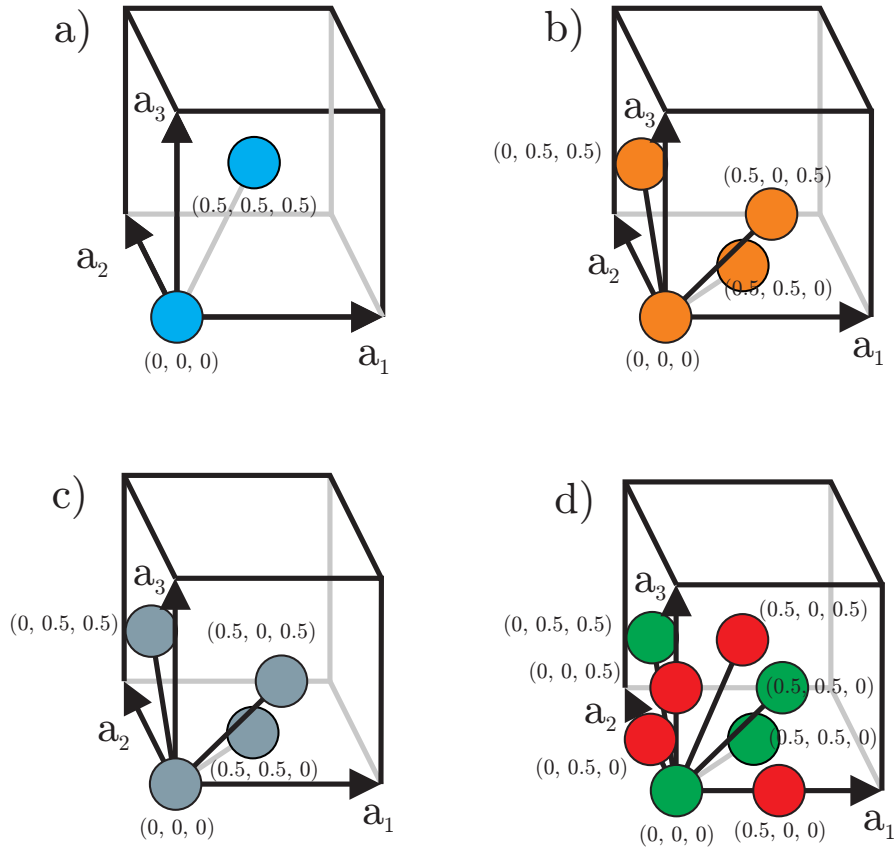
Figure 2.3: Conventional unit cells of four materials studied in this thesis. The numbers in parenthesis indicate the fractional coordinates of the atoms in the cell. The lattice vectors $\mathbf{a}_i$ are defined by the arrows in the figure. a) A Fe unit cell in a body centred cubic (bcc) configuration. b) A Cu unit cell in a face centred cubic lattice (fcc) configuration. c) A Ni unit cell in a face centred cubic (fcc) configuration. d) An MgO unit cell in a face centred cubic (fcc) configuration, the red atoms are O and the green atoms are Mg. The conventional unit cells shown completely specify a commensurate lattice.

In this thesis the focus is primarily on GB interfaces which are 2D defects that form at the interface between connected grains [63]. The simplest type of GB interface is a bicrystal which is a planar interface between two crystals of arbitrary relative orientation. In all bicrystals there are five macroscopic degrees of freedom which can be specified by two vectors $\mathbf{n}_1$ and $\mathbf{n}_2$, and an angle θ. The vectors $\mathbf{n}_1$ and $\mathbf{n}_2$ each contain two irreducible

degrees of freedom[1] while θ possesses one degree of freedom which describes how much $\mathbf{n}_2$ can be rotated about a common tilt axis (see Fig. 2.4). θ is defined such that the two vectors $\mathbf{n}_1$ and $\mathbf{n}_2$ share a common tilt direction ($\mathbf{m}_1$). The common tilt direction is defined as the cross product ($\mathbf{m}_1 = \mathbf{n}_1 \times \mathbf{n}_2$) between $\mathbf{n}_1$ and $\mathbf{n}_2$. A common tilt angle can be defined for any two vectors except when they are parallel, in the parallel case solutions exist but are not unique.
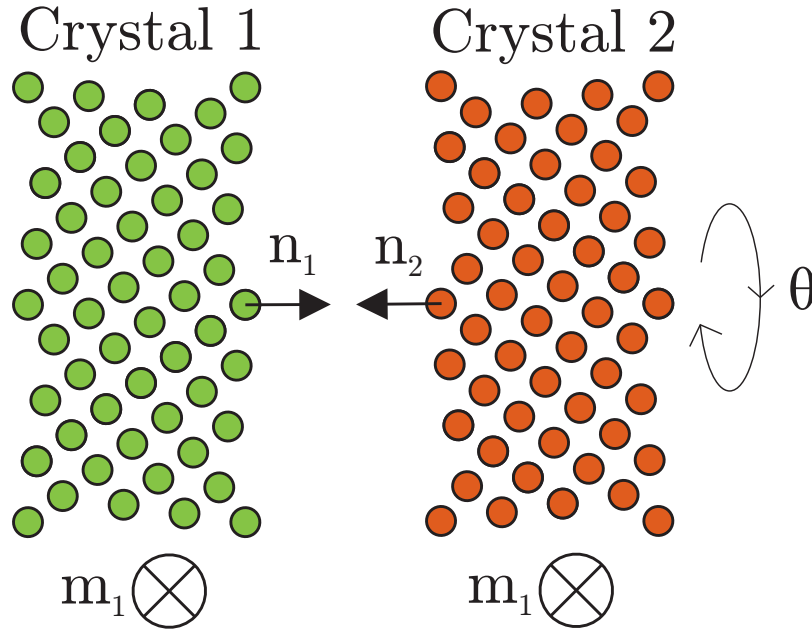
Figure 2.4: Schematic showing how the five different macroscopic degrees of freedom of a bicrystal system $\mathbf{n}_1$, $\mathbf{n}_2$ and θ are related. The $\mathbf{m}_1$ direction is common to both $\mathbf{n}_1$ and $\mathbf{n}_2$ and is how θ is defined.

The microscopic degrees of freedom are a translation vector between the two crystals parallel to the GB and a vector which describes where the crystal is truncated for non-monatomic crystals. For example, in the case of MgO (111) the crystal could be truncated either on oxygen or on magnesium. The microscopic degrees of freedom are non-separable from the macroscopic degrees of freedom and cannot easily be determined *a priori*, however they are important to consider when building bicrystals. When the angle $\theta = 0$ GBs are known as tilt GBs. There are two main types of tilt GBs: symmetric

---

[1]Although Miller indices contain three degrees of freedom they can be completely specified by transforming them to spherical polar coordinates with only two degrees of freedom (the polar angle and the azimuthal angle).

tilt GBs (STGBs) and asymmetric tilt GBs (ATGBs). STGBs are those with the same rotation about the tilt axis. ATGBs are those with different rotations about the tilt axis. Tilt GBs are usually arranged from structures known as structural units (SUs). The structural units are essentially chains of dislocation cores which distribute the strain across the interface. There is not a unique way for the dislocation cores to be defined and each GB can allow many different combinations of dislocation cores to be present (explained in more detail in Sec. 4.2.2). Whereas when $\theta \neq 0$ GBs are known as twist GBs. Twist GBs often do not have dislocation structures which resemble a recognisable pattern [65–68]. GBs will often reconstruct to a system of dislocations which have the lowest energy. Although in real devices thermal effects can allow for the co-existence of different dislocations and SUs.

2.1.2 Computational modelling of grain boundaries

Symmetric tilt GBs are two-dimensional extended defects that form at the interface between two grains which are rotated in opposite directions about a common tilt axis. The misorientation of symmetric tilt grain boundaries can be defined by computing the dot product between the smallest vector perpendicular to the tilt axis ($\phi = cos^{-1}\left(\frac{n_1 \cdot a_1}{|n_1||a_1|}\right)$) where a_1 is the smallest vector perpendicular to the tilt axis. The two grains can then be defined relative to each other in the following way $n_1 = R(2\phi)n_2$ where R is a rotation matrix and ϕ is the misorientation (the tilt angle). Thus a shorthand can be employed to simplify the specification of the interface. The crystallographic orientation of the GB can be fully defined by specifying the crystallographic plane parallel to the GB $\mathbf{n}_1 = (hkl)$, the tilt axis direction $\mathbf{m}_1 = [mno]$, $\theta = 0$ and is usually denoted in the form $(hkl)[mno]$. Here, the atomic structure of such GBs in three-dimensionally periodic supercells are shown in Fig. 2.5a. To make the supercell periodic in the direction parallel to the GB plane two identical GBs are introduced. It is ensured that the separation between the GBs is sufficiently large that mutual elastic interactions are small and can be safely neglected in prediction of GB properties (GB separations of 30 Å are more than sufficient).
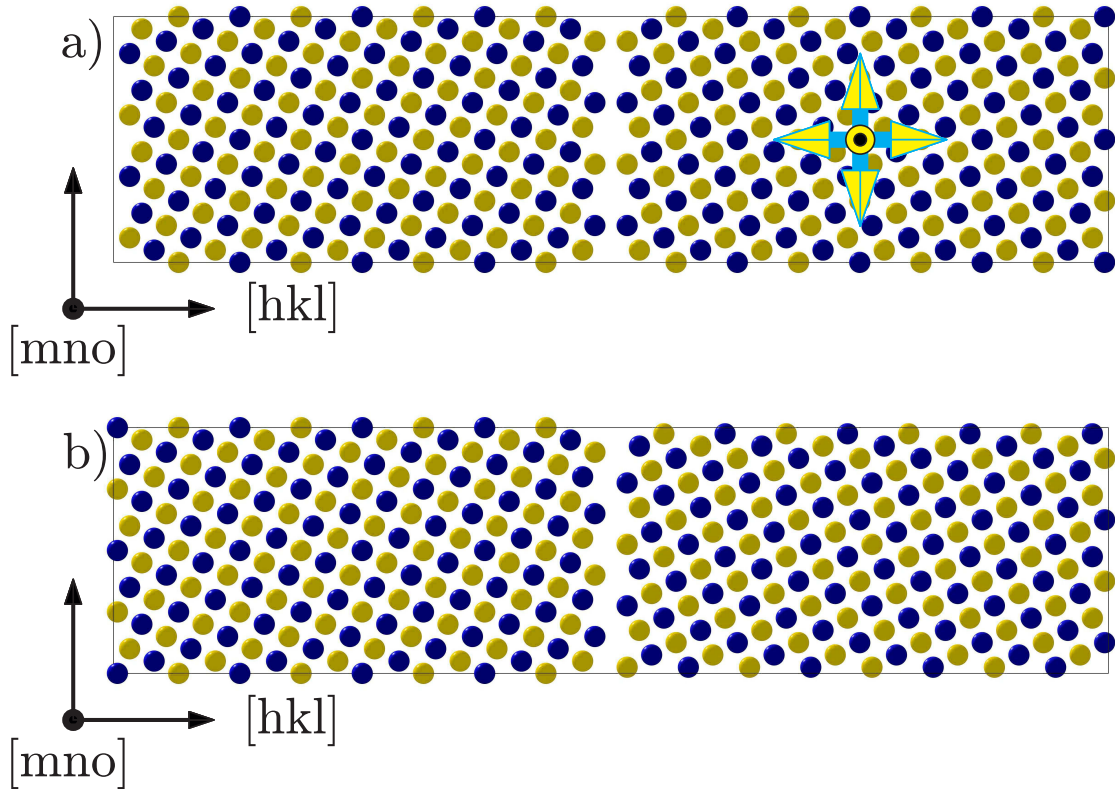
Figure 2.5: A typical bicrystal supercell in an fcc material. The yellow and blue atoms indicate atoms in different planes perpendicular to the tilt direction $[mno]$. a) Initially two mirror symmetric grains are placed in the simulation cell. The yellow arrows indicate the directions in which the right grain is to be translated. b) An example of a configuration obtained after one crystal is translated with respect to the other.

While the crystallographic orientation of the grains in the supercell are fully defined by the GB type – $(hkl)[mno]$ – it is not known *a priori* how the grains should be positioned with respect to each other. In particular, it is known that grains can exhibit rigid body translations where one grain is translated with respect to the other in the plane parallel to the GB (see Fig. 2.5b). To find the most stable GB structure total energy calculations on supercells of the type shown in Fig. 2.5 are performed. Depending on the elemental composition of the supercell DFT or classical simulation code can be used to optimise the cell and/or atomic positions and calculate the total energy of the system.

To identify the most stable GB structure for a given orientation many initial structures corresponding to different relative translations of one grain with respect to the

other are systematically generated. This approach is called the γ surface approach and has been employed by authors such as Mike Finnis [69]. Translations are performed in steps over a range of half of the supercell length in the periodic directions $[mno]$ and $[hkl] \times [mno]$ (the vector orthogonal to (hkl) and $[mno]$) and between a similar range in the GB normal direction (hkl). Following crystal translation, if any two atoms are closer than $0.1a$ (where a is the lattice constant) one is deleted to obtain a more realistic starting configuration for geometry optimisation. The optimum grid size was found to be 1.0 Å parallel to the GB plane and 0.5 Å in the GB normal direction. Such a grid size offers computational speed and possess sufficient resolution to find stable structures. This algorithm generates many initial structures corresponding to different grain terminations, relative grain translations and atomic configurations near the interface. The initial structures generated using the procedure outlined above are fully optimised with respect to relaxation of all ions and the length of the supercell perpendicular to the GB [70–72]. The method of optimisation varies between the simulation packages. The different optimisation methods are explained in Sec. 3.1. In the case of heterogeneous interfaces a similar procedure to find the lowest energy interfaces is performed with the difference that translations are not performed in the direction parallel to the interface to maintain interface stoichiometry.

If two lattices of different orientation are overlapped there will be certain points in lattice 1 which coincide exactly with some lattice points of lattice 2. This overlapping structure is called a coincidence site lattice (CSL) and is a superstructure of lattices 1 and 2 (see Fig. 2.6). Using the number of lattice points in the CSL and the number in the unit cell of the generating lattice a Σ value can be defined. Σ is the unit cell volume of the CSL in units of the unit cell volume of the elementary cells of the crystals. If even the Σ value can be divided by a factor of two to reduce it and maintain the same periodicity thus always should be odd. Using the CSL method it is easy to visualise and construct the smallest possible repeating GB supercell for the generating lattices [73].
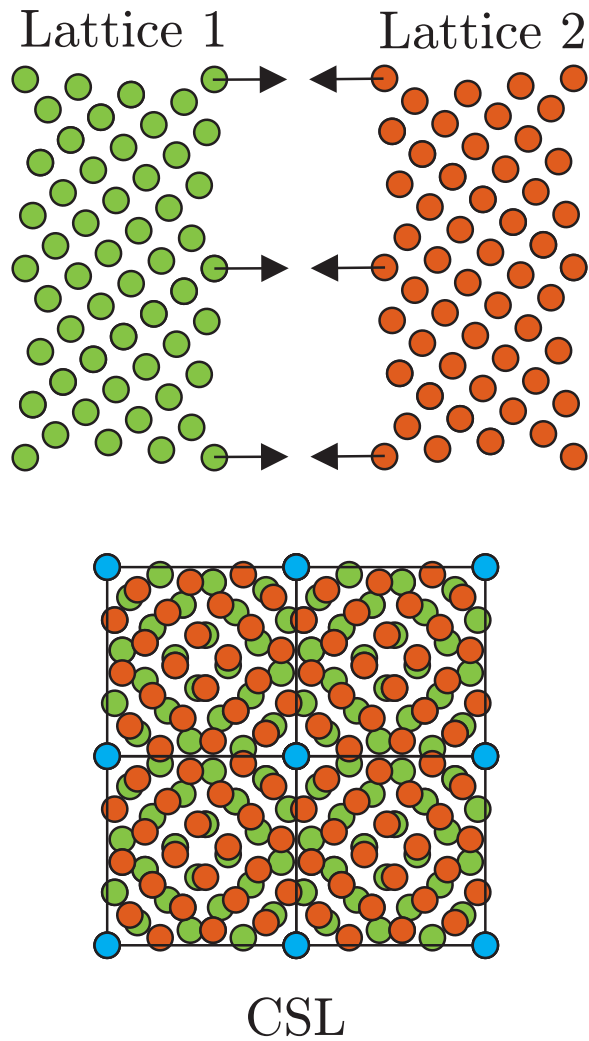
Figure 2.6: Schematic showing how the coincidence site lattice is created from two lattices of differing orientation. The superpositions of the two lattices creates a superstructure. The coincidence site lattice is defined within the confines of the blue circles.

Alternative to the supercell approach and the CSL approach it is possible to specify two crystallographic regions e.g. in the Minimum Energy Technique Applied to Dislocations Interfaces and Surfaces Energies (METADISE) code which are chosen to be optimised [74]. During minimisation the atoms within region 1 are relaxed, while the positions of the atoms in region 2 are held fixed[2] (see Fig. 2.7). The METADISE ap-

---

[2]Though its centre of mass may move.

proach reduces the number of degrees of freedom in the system for faster optimisation. The energy of the system can be written down as $U_{latt} = U_1 + U_2$, where U_1 is the energy of region 1 and U_2 the energy of region 2. In METADISE grain boundaries, defects and surfaces are two dimensionally periodic.
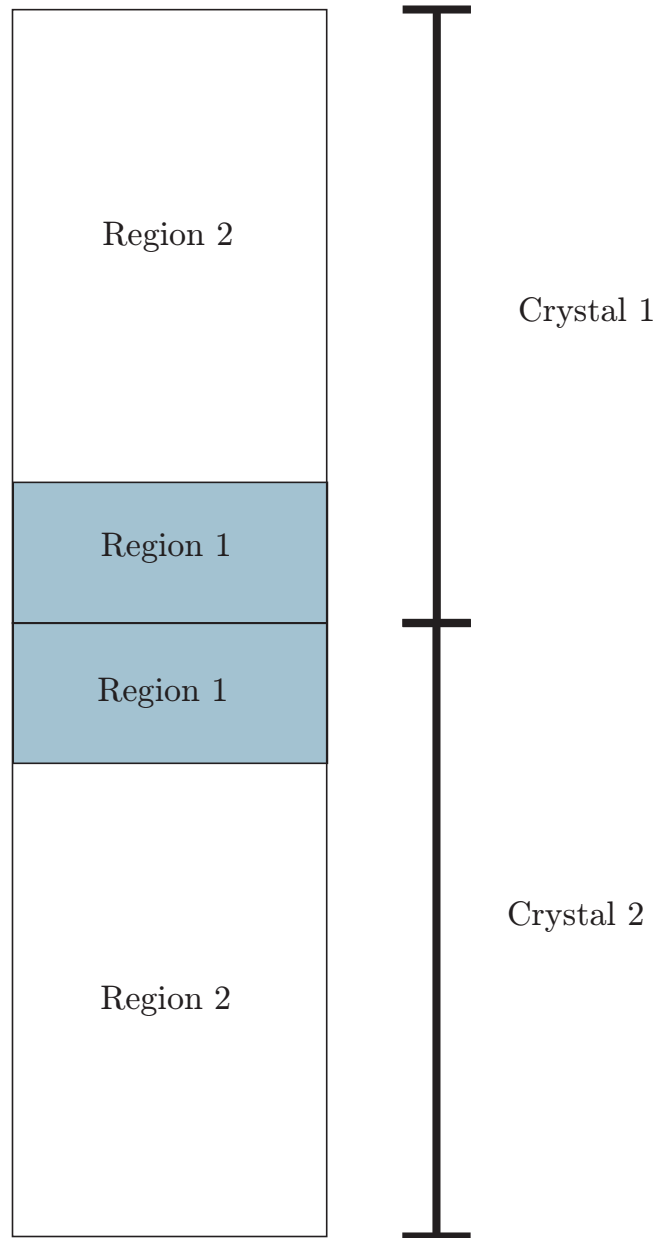
Figure 2.7: Schematic showing how the METADISE (bicrystal) approach splits up an interface for optimisation.

2.1.3 Grain boundary properties

The formation energy is a useful quantity which characterises the relative stability of a defect. The formation energy can be expressed in the following way,

$$E_f = E_{\text{tot}} - \sum_i N_i \mu_i, \tag{2.1}$$

where E_{tot} is the total energy of the supercell, μ_i is the chemical potential for atom i and N_i is the number of atoms in the supercell. For a bulk crystal the chemical potential μ_i reduces to the cohesive energy E_{coh}. In the case of a GB the formation energy is calculated by comparing a supercell with a GB in it to a supercell with exactly the same number of atoms but with no GB. The area of the interface normal is different for each GB orientation thus the numerator is divided by the area to allow for comparison between different GBs. The formation energy per unit area for GBs is calculated in the following way,

$$\gamma = \frac{E_{\text{tot}} - \sum_i N_i \mu_i}{2A}, \tag{2.2}$$

where A is the area of the GB normal direction the factor of two arises since in the supercell approach bicrystals contain two GBs.

While the formation energy is a key property in understanding the stability of GBs it is extremely difficult to probe experimentally. However another property called the excess volume can more easily be compared to experiment. The excess volume was first discussed by Bishop through a private communication to Aaron and Bolling in 1972 [75]. GBs are almost always associated with an excess volume relative to the corresponding bulk crystal. The excess volume is the degree of expansion of a material due to the presence of a GB. Contrary to the name the excess volume is a change in length as is it defined per unit area. The excess volume can be defined as,

$$\delta V = \left(\frac{\partial V}{\partial A} \right)_{T,p,n_i}, \tag{2.3}$$

where the partial derivate is evaluated at constant temperature T, pressure p and number of atoms n_i. It is calculated computationally in the following way,

$$\delta V = \frac{V_{\text{tot}} - N\Omega_{\text{bulk}}}{2A}, \tag{2.4}$$

where V_{tot} is the volume of the supercell, Ω_{bulk} is the atomic volume per atom in the bulk crystal, N is the number of atoms in the supercell and A is the surface area of the interface plane.

2.1.4 Stereographic projections

It is difficult to visualise the variation of properties with respect to variation of the Miller indices which define GB orientations. A useful approach is to project the Miller indices onto a unit sphere representing a conversion between Cartesian and spherical coordinates. There are many ways to perform the Cartesian spherical mapping including a conformal mapping known as stereographic projection or an equal-area map called the Lambert-equal area projection (LP). These differ as the conformal map conserves the angles between different vectors while the equal area map conserves all areas swept out by the vectors. In this thesis the LP and the stereographic projection are used and are equally informative. Transformations between Miller indices and conformal stereographic coordinates can be computed using the following formulae,

$$X = \frac{k}{\sqrt{h^2 + k^2 + l^2}}, \tag{2.5}$$

$$Y = \frac{l}{\sqrt{h^2 + k^2 + l^2}}, \tag{2.6}$$

where X and Y are the two conformal stereographic coordinates, h, k and l are the usual Miller indices, the reader is directed to ref. [76] p. 39-45 and [77] for further information. Once in conformal spherical coordinates a transformation can be performed to get the coordinates in the Lambert azimuthal equal area projection X' and Y'. This is achieved by first transforming into Cartesian coordinates (x, y, z) then into equal area coordinates in the following way,

$$x = \frac{2X}{\sqrt{1 + X^2 + Y^2}}, \tag{2.7}$$

$$y = \frac{2Y}{\sqrt{1 + X^2 + Y^2}}, \tag{2.8}$$

$$z = \frac{-1 + X^2 + Y^2}{\sqrt{1 + X^2 + Y^2}}, \tag{2.9}$$

$$X' = \sqrt{\frac{2}{1 - z}} x, \tag{2.10}$$

$$Y' = \sqrt{\frac{2}{1 - z}} y. \tag{2.11}$$

This can be done in one step but is shown in full for the reader. Fig. 2.8 shows a schematic drawing which explains how the conversation process between 3D Miller indices and 2D stereographic coordinates is performed.
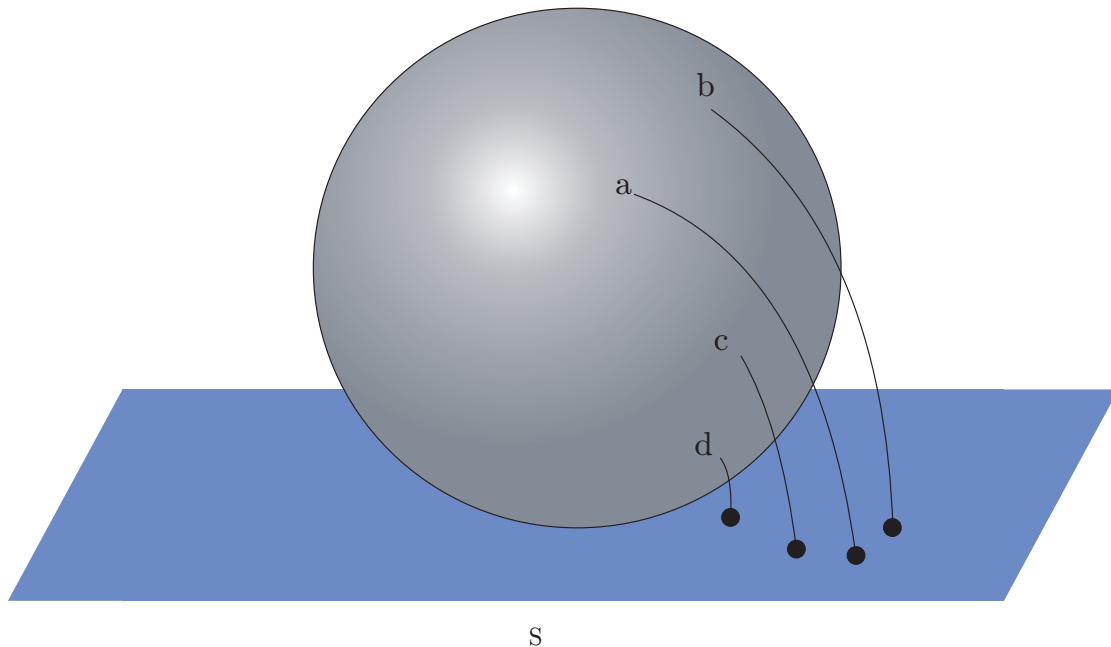
Figure 2.8: Schematic showing how the Miller indices can be mapped on a 2D surface S using the Lambert azimuthal equal area projection. The letters a-d refer to Miller indices on to the unit sphere.

With the LP or stereographic mapping it is possible to show how GB properties such as the excess volume or GB formation energy change with orientation in a 2D figure. The z-axis is usually coloured to denote excess volume or GB formation energy (see Sec. 4.2.3).

2.2 Previous work on grain boundaries in metals

2.2.1 Theoretical

One of the first theoretical models of GBs in the literature is the model of Read and Shockley in 1950 [78]. One of the insights given by Read and Shockley was to relate the theory and understanding of dislocations to GBs. It is a continuum model where the variation of the GB formation energy (γ) is approximately linear in the low angle limit

(i.e. GBs which have a small inclination between the grains). The Read-Shockley model is applicable to both metals and metal-oxides. The Read-Shockley equation is given as,

$$\gamma = \frac{Gb}{4\pi(1-\nu)}\theta\left(1 + \ln\left(\frac{b}{2\pi r_0}\right) - \ln\theta\right),$$ (2.12)

where G is the shear modulus, b is the Burgers vector, ν is Poisson's ratio and r_0 is the radius of the dislocation core. Read and Shockley's paper has had enormous impact and has been cited over 1600 times.

Another landmark paper is DG Brandon's paper in 1966 [79]. Read and Shockley's model did not work well for high angle GBs because the chains of dislocations begin to interact with each other to lower their energy. In Brandon's work he developed a discrete model of GBs based on the dislocation model of Read and Shockley and the CSLs of Kronig and Wilson[3] [78]. The model applies both to metals and metal-oxides and was a step forward in the understanding of high angle GBs. The model moves away from the traditional ideas that GBs are rigid objects and allows for some deviation of the CSLs allowing for strain in the crystal structure. Brandon also explored the locations of some of the common CSLs in the stereographic projection including twin GBs in the fcc and bcc structures. Brandon's paper has also had very significant impact in the definition and characterisation of GBs being cited over 1600 times.

Computational modelling of the atomic structure of GBs was catalysed by the confluence of two things: the development of approximate methods which enabled atomistic modelling to be feasible and the dramatic increase in computational power in the late 1990s which enabled large enough simulation cells to be simulated. One particular method which was developed by Daw and Baskes in Sandia National Laboratories and similarly Finnis and Sinclair in the University of Oxford is called the EAM [29,30]. The EAM method is a classical method used to describe the interactions in metals. The EAM is described in more detail in the methods section (Sec. 3.1.1.2).

Using classical simulations a range of properties can be determined including: the formation energy of surfaces, bond strain, elastic constants and moduli, and cohesive energies. In interatomic (classical) based methods it is possible to find stable structures using a range of optimisation methods such as simulated annealing, minimisation and genetic algorithms. Simulated annealing and genetic algorithms have been used widely

---

[3]Kronig and Wilson developed the idea of CSLs explained in Sec. 2.1.1.

to predict the structures of many metallic systems including Cu-Au nanoalloy clusters, Al nanoparticles, Ni, Ag and Au nanoclusters, Li, K, Al and P [80–83].

One of the first researchers to look at the properties of Gbs in metals computationally using the EAM was D. Wolf in 1989 and 1990 [44, 84]. In his many papers he confirmed the Read and Shockley relationship at low inclination angles. Wolf also found that there are quite interesting trends in the GB formation energy at high angles. He found the existence of cusps where the GB formation was lower than GBs which have angles which are nearby (see Figs. 4.8 & 4.7). Wolf's work laid the foundation for characterising GBs computationally. Many other researchers have used the EAM to compute the formation energy of GBs including within nickel [85] and copper [86] which validated much of Wolf's work.

In DFT many more properties can be predicted such as the density of states, band structure and magnetisation. It was not until 1997 when the first DFT calculations of GBs in aluminium were performed by Ogata *et. al.* [87]. They showed that there was a good agreement of the GB formation energies with other methods and experiment but showed that the EAM did not perform well. This is quite interesting because there have been studies subsequent to this which show that there is a good agreement in terms of the energetic ordering [88].

A range of modelling techniques based on both classical potentials and first principles calculations have been developed to predict the structure of GBs on the basis of their formation energy [84–86, 89–93]. In many cases very good agreement between computational predictions and experiment is obtained for both structure and associated properties (e.g. mechanical, electronic or chemical) [84, 85, 92, 94–96]. A rather general finding is that GBs are often favourable locations for the segregation of point defects and impurities which in part has been associated with the additional free space which can more easily accommodate lattice defects [38, 75, 95, 97–100]. For example, the segregation of He to GBs in metals and the resulting embrittlement has received significant attention owing to its relevance to the design of materials for fusion reactors [26, 101–106].

2.2.2 Experimental

The structure and properties of GBs in metals have been the focus of many previous experimental investigations [41, 63, 79, 107–109]. Transmission electron microscopy (TEM) is an invaluable technique to probe the atomic structure. TEM uses a beam of electrons

which pass through a whole sample of material (transmission). The electrons are detected after they have been scattered by atoms in the sample. To improve the resolution of TEM the electron beam can be focused then scanned over the sample known as STEM. In STEM electron lenses are used to focus the electron beam into a cross section much smaller than then the size of the sample. Transmission of the highly focussed electrons gives a much higher resolution of the sample [15, 110]. For example, studies of materials after mechanical work and annealing processes have revealed their polycrystalline texture [111, 112]. Detailed images of the structure of individual tilt GBs have also been acquired for copper and nickel [113, 114]. The TEM experiments on copper and nickel confirm that there is a relationship between the GB orientation and the structures of associated dislocation cores. It is possible to probe the density of states of a sample using EELS [115]. Using a scanning electron microscope (SEM) it is possible to perform a technique known as electron back scatter diffraction (EBSD). EBSD uses backscattered electrons in an SEM to detect the distribution of grain sizes and orientations within a sample. Many studies have used EBSD to determine the granular distribution of copper, nickel and steel [116–118]. Magnetic structure can also be detected experimentally using TEM and energy loss magnetic chiral dichroism [119–121]. Segregation of elements to GBs and their modified diffusion is also an issue that has received considerable attention [24, 25, 122]. For example, segregation of H and Bi to GBs in palladium and copper has been probed [38, 123] using TEM and activity measurements. The diffusion of impurities along GBs in metals have also been studied using the tracer diffusion method [124, 125].

The additional 'free space' created by the excess volume is thought to be one of the main factors responsible for the preferential segregation of point defects and impurities towards GBs, which affects key materials properties, such as mechanical strength and electrical resistivity [38–41]. It also helps explain the phenomena of enhanced impurity diffusion along GBs that has been observed in a diverse range of materials [124, 126, 127]. While excess volume is recognised as a key materials parameter probing it in real materials remains extremely challenging. A small number of studies have characterised excess volume for specific GBs using high-resolution electron microscopy [128, 129]. More recently ensemble average excess volumes have been determined for bulk polycrystalline samples of copper and nickel using high-precision difference dilatometry [42, 43]. The experimental studies found that the average excess volume associated with GBs in Cu

(0.46 Å) is significantly larger than that in Ni (0.32 Å) – a difference of over 40%. Given that Cu and Ni posses the same fcc crystal structure and fairly similar lattice constants (3.62 Å and 3.52 Å respectively, a difference of less than 3%). The large difference between the excess volumes of Cu and Ni is currently lacking an atomistic explanation.

The drive to miniaturise optical lenses is creating significant interest with the advent of metalenses. Optical microscopy has been used to image plasmon surface modes of metals, which can manipulate light waves on the nanoscale [130, 131].

2.3 Previous work on grain boundaries in metal-oxides

2.3.1 Theoretical

In metal-oxides the presence of the ions in the crystal structure means that the long range Columb interaction must be considered. Some of the first theoretical studies on metal-oxides led to the development of interatomic potential such as the Buckingham potentials (see Sec. 3.1.1.1). Richard Catlow *et. al.* developed Buckingham potentials for a range of different materials such as oxides and fluorides [132–134]. The potential-based models have been extremely successful at predicting the structures and properties of a range of metal-oxides. Catlow and co-workers' work is extremely important as it opened up the field of modelling metal-oxides and has been cited over 1400 times. Subsequent to developing interatomic potentials others such as Julian Gale have written systematic reviews of the empirical potential fitting process and parameterised metal-oxides such as MgO [135]. Julian is also one of the developers for the GULP code which offers many interesting features when compared to other molecular dynamics code, such as the ability to automatically compute the elastic constants [136].

With a description of the atomic interactions for metal-oxides the properties of metal oxides can be investigated. Watson *et. al.* developed a code called METADISE which can systematically create defect structures such as surfaces and GBs. The METADISE code uses the bicrystal approach as shown in Fig. 2.7 to find optimised surfaces and interface geometries. The METADISE code is extremely popular being cited over 350 times and used widely to study surfaces, GBs and dislocations within MgO [74]. More recently a new code called *ab-initio* random structure searching (AIRSS) has been developed by Christopher Pickard and Richard Needs [137]. The AIRSS code works in a similar way to METADISE with the exception that optimised geometries can be found by pseudo

randomly[4] generating the geometries. The AIRSS code has been cited over 184 times and has been used to predict the structure of ZrO/Zr interfaces [138]. The AIRSS code has also been used to predict the structure of grain boundaries within graphene and SrTiO$_3$ [139].

D. Wolf performed some of the first calculations of GBs in metal oxides such as CaO, MnO and NiO [65]. Wolf's work used some of the interatomic potentials developed by Catlow *et. al.* to show that for certain twist orientations the GB formation energy lied significantly above the energy of the free surface. This is interesting because it suggests that GBs would like to de-adhere to form free surfaces. It was suggested by Wolf that additional techniques need to be employed to compute the geometry of twist GBs other than the CSL. Calculations on twist GBs have also been performed by Dorothy Duffy and co-workers using lattice relaxation models in NiO [140–142]. Duffy's work showed the existence of GB cusps in the (111) orientation with very ordered structures at the GBs. The GBs in Duffy's work were also extremely high in formation energy suggesting that the GBs would rather form free surfaces. Twist GBs in MgO have been the subject of intense investigation including the Σ25 GB by Dean Sayle [67]. In Dean Sayle's work, Dean and co-workers showed that MgO twist GBs are largely unstable but can become stable if the density of MgO units is reduced at the interface. This insight allowed researchers to find more stable geometrical configurations in general twist GBs. Further studies of the energetic stability of MgO twist GBs have been calculated using an empirical potential and DFT by Harding *et. al.* [143]. Harding showed the differences between the density of states of the relaxed and unrelaxed GBs using DFT (see Sec. 3.1.2.2). Harding found that there are additional states which occur near the valence band in the relaxed boundary slightly reducing the band gap. Further work has been undertaken by Harding *et. al.* on the rock salt structured oxides of MgO and NiO. His work reveals the stark contrast between the discontinuous nature of the energy of GBs and continuous nature of surface energies in a tilt series [144]. The effect of temperature on MgO GBs has also been investigated by Harris *et. al.* [145]. Harris' showed that MgO GBs dilate when they are heated and can structurally transform to accommodate for the additional strain at the interface. The application of pressure to GBs reduces the average bond length at interfaces. DFT calculations have been performed on MgO at high pressures to compare the structure and electronic properties

---

[4]With constraints such as ensuring atoms do not get too close etc.

with experiment [146, 147]. The influence of heat and pressure on GBs in MgO has also been performed to gain an insight into MgO at the centre of planets [148]. The properties of vacancies near GBs in MgO has also been studied [149]. In the study classical Buckingham interatomic potentials have been used to study the presence of point defects near GBs in MgO. The results show that the segregation of oxygen is preferred at the centre of the GBs [150].

In contrast to static calculations Dean Sayle and co-workers developed a technique called amorphisation and recrystallisation. The amorphisation and recrystallisation technique forces a film on a substrate to become amorphous, then after a period of dynamical simulation the cluster recrystallises. The recrystalised structure contains GBs, dislocations, steps, vacancies and other defects. This technique can predict growth, nucleation and structural properties of metal-oxides and has been applied to a range of metal-oxide/metal-oxide systems in various combinations including MgO, CaO, $SrTiO_3$ and BaO [151–154]. Genetic algorithms have been used to predict the structures of a range of metal oxides and of interfaces in $SrTiO_3$ [155, 156]. It is a general observation that interatomic potentials sometimes do not perform well in situations which they have not been parameterised. To combat the under fitting issue interatomic potential models have been extended by parameterising interatomic potentials based on first principles calculations [157]. The idea of fitting interatomic potentials using first principles calculations has had significant impact on scientific discovery being cited over 1200 times. Mike Finnis and co-workers have used the *ab-initio* parametrised interatomic potential for Al_2O_3 which has been found to be comparable in predictive properties to DFT but with less computational cost [158]. Interfaces of Ag/MgO have been investigated by comparing results between interatomic potentials and first principles calculations [159]. First principles calculations have been performed to compare how the use of different exchange correlation functionals affects the predicted material properties between NiO, MgO and CoO [160]. Properties of the $\Sigma 7$ GB in Al_2O_3 have been calculated using DFT by Mike Finnis and co-workers, in their work they show the effect of different GBs on the density of states and compare GB formation energies between different levels of theory [161]. It is a general observation that the presence of GBs in insulators reduces the band gap. Further calculations have been performed on surfaces and GBs in a range of materials including TiO_2, MgO and HfO_2 [16, 162–164].

2.3.2 Experimental

There have been a multitude of methods used to characterise metal-oxide films including STM, TEM, electron energy loss spectroscopy, x-ray diffraction and atomic force microscopy. An STM uses a conducting tip which is brought very near to the surface of a sample of material. A bias voltage is then applied to the tip such that electrons can tunnel through the vacuum gap between the sample and tip. The resulting tunnelling current can be measured against the applied voltage (bias) to create an image of the sample. STM has been widely used to image dislocations in MgO grown on Mo [62,165,166]. STM studies have also been performed on other oxides such as TiO_2 and WO_3 [167–169]. While STM can be used to investigate surfaces it does not give an atomically resolved level of detail. By contrast TEM studies have been performed to atomically resolve the structure of MgO twist GBs [170–172]. The studies find examples of preferred CSL orientations. Experimental evidence of certain CSL orientations is important as a starting point for first principles calculations. STEM studies have also been performed on MTJs (in cross-section) to visualise the Fe/MgO stack structure [53–55, 173, 174]. The TEM images do show some evidence of dislocations and the possibility of GBs. It has also been possible to observe the roughness of Fe/MgO/Fe interfaces using TEM [175]. High resolution STEM has managed to atomically resolve different dislocations in MgO which have been compared to theoretical predictions [16]. Electron energy loss spectroscopy (EELS) is a technique which can determine the types of atoms which are present in a sample. EELS experiments can be performed by passing electrons with energies between 100 - 300 keV through a sample and measuring the amount of energy which is lost after the electrons have passed through[5] [176]. Due to the electromagnetic lenses which are used this beam can be focussed on to small diameter between 1 nm and 0.1 nm. This gives atomically resolved information on the chemical composition of a sample. Alternatively EELS experiments can be performed with low energy electrons which reflect from the surface of a sample. Using low energy electrons is a higher precision technique and known as high resolution EELS. The use of EELS, TEM and computational models is an extremely powerful trinity for studying thin film materials. In 1998 Steve Pennycook *et. al.* demonstrated this trinity by showing that calcium was segregating to GBs in MgO which caused a structural transformation of the structural units of the GBs [177].

---

[5]TEM samples are usually of no more than 1 μm thick.

The presence of Ca was confirmed by EELS and its stability was investigated using first principles calculations. More recent studies involving the MgO (310)[001] GB have shown that other materials such as titanium are present near the GBs [16]. Additional studies have shown the behaviour of boron before and after annealing of a magnetic tunnel junction. The results show that boron is likely to be in the charge state of 3+ if it were to enter the MgO after annealing [17]. X-ray diffraction and photo spectroscopy techniques have been used to study the growth of MgO on Fe. A couple of studies have showed that a layer of FeO can form in-between the Fe and MgO structure [178, 179]. Using x-ray diffraction it is possible to show how strain equilibrates in interfaces of NiO on MgO [180].

Chapter 3

Methods

Predicting the macroscopic properties of matter has been made possible using atomistic simulations. Atomistic simulations model a system of interest by characterising it using numerous variables. The variables in the system are adjusted alone or in combination and the effect of the changes on the system is calculated. Computational modelling has accelerated the rate of progress in science and industry as scientists and engineers can conduct hundreds of simulated experiments using computers to reduce the search space of possibilities for experimentalists or to model systems which cannot easily be experimentally measured. The best use of computational modelling is in conjunction with other methods to maximise the utility. It is impossible to simulate the exact behaviour of nature since both the unified fundamental equations governing nature and enough computing power to process all possible combinations and permutations are required. In any case such a calculation would violate the computational density of this Universe [181]. As computational models can only recreate a small section of a system a deliberate choice of the degrees of freedom should be selected. Careful approximations and symmetry should be employed to simplify problems. Computational modelling is one of the fastest growing areas of science with many universities and international companies housing modelling departments. Computational modelling has successfully been applied to many other areas of science such as weather forecasting, economics, sociology and is growing [182–184].

In this thesis computational techniques have been employed to model simplified polycrystalline systems. As traditional pen and paper theoretical techniques cannot easily explore the vast phase space of possibilities required to understand polycrystalline materials and designing suitable experiments to probe phenomena of interest can be extremely

challenging. Understanding polycrystalline materials is one of current challenges in material science.

In this chapter the methods and techniques used to model polycrystalline materials throughout this thesis are explained in detail.

The chapter is arranged into two sections. The first of which explains the principles behind total energy calculations including the EAM and DFT which are used throughout this thesis (Sec. 3.1). The final section details all of the code which are used for simulation and analysis (Sec. 3.2).

3.1 Total energy calculations

The concept of total (internal) energy is paramount in computational modelling. The total energy depends explicitly on all of the electrons and nuclei in a given system. The total energy of most systems cannot be determined exactly thus approximations must be used to simplify the physics [136]. The approximations which are used in this thesis are the EAM and DFT which allow the total energy of a system to be computed. With an approximate description of a system's energy the forces can be calculated which in turn can be used to move the atoms and relax the structure (as $F = -\nabla E$). Simplistically the collection of atoms are moved such that the total energy of the system reduces. The lowest energy state of a given system is known as a global minima but as the complexity of a system increases the number of degrees of freedom increases which reduces the likelihood that global minima can be found. In most cases local minima are found from optimisation methods. It is a requirement that many initial configurations are specified to increase the probability that the most stable configuration is found. There are many different types of optimisation algorithm including descent algorithms, quasi-Newtonian, genetic algorithms and simulated annealing. In this thesis only quasi-Newtonian methods and descent algorithms are used. The conjugate gradients (CG) algorithm is a descent algorithm which is heavily used in classical and electronic structure code used in this thesis. It is defined below,

$$\mathbf{s}_{n+1} = \mathbf{g}_{n+1} + \gamma_n \mathbf{s}_n, \tag{3.1}$$

where $\mathbf{s}_n$ is the search direction at a step n, $\mathbf{g}_n$ is the gradient at each step and the parameter γ_n is defined as,

$$\gamma_n = \frac{\mathbf{g}_{n+1} \cdot \mathbf{g}_{n+1}}{\mathbf{g}_n \cdot \mathbf{g}_n}. \tag{3.2}$$

If a line minimisation is applied to each search direction the definition of the CGs algorithm generates a series of search directions which are orthogonal to the gradient $\mathbf{s}_n \cdot \mathbf{g}_n = 0$ for different steps. The search direction is also conjugate to previous search directions such that previous search directions are not repeated. The CG algorithm moves a system's energy downhill to find a stable configuration. Although the Hessian matrix[1] ($\mathbf{H}$) is not explicitly calculated it is how the conjugacy condition is determined $\mathbf{s}_n \cdot \mathbf{H} \cdot \mathbf{s}_n = 0$.

In quasi-Newtonian (or Hessian) methods an approximation to the Hessian or its inverse is computed. With the correct Hessian it is possible to get the minima of the system as the Hessian represents the types of turning points in a system. It can be demonstrated that if a function is expanded into a quadratic form shown below,

$$E(\mathbf{R} + \delta\mathbf{R}) = E(\mathbf{R}) + \delta\mathbf{R} \cdot \nabla E(\mathbf{R}) + \frac{1}{2}\delta\mathbf{R} \cdot H \cdot \delta\mathbf{R}, \tag{3.3}$$

where E is a quadratic function of the energy landscape and $\delta\mathbf{R}$ is a small change in position. Then the derivative of Eqn. 3.3 is taken,

$$\nabla E(\mathbf{R} + \delta\mathbf{R}) = 0 = \nabla E(\mathbf{R}) + H \cdot \delta\mathbf{R}, \tag{3.4}$$

the $\delta\mathbf{R}$ can be determined as $\delta\mathbf{R} = -H^{-1} \cdot \nabla E(\mathbf{R})$. Both the CGs and the quasi-Newtonian methods are very robust efficient and reliable [185]. The Hessian can become quite large so schemes such as the low memory BFGS algorithm have been developed to reduce its size [186].

3.1.1 Interatomic potentials

Classical modelling assumes that the electrons are integrated out and atoms and ions are treated as point particles. The total energy then becomes a series of interactions between different orders of the total number of atoms [136]. The many-body energy can be written down as an infinite series shown below,

$$U = \sum_{i=1}^{N} U_i + \frac{1}{2}\sum_{i=1}^{N}\sum_{j=1}^{N} U_{ij} + \frac{1}{6}\sum_{i=1}^{N}\sum_{j=1}^{N}\sum_{k=1}^{N} U_{ijk} + \dots, \tag{3.5}$$

---

[1]The Hessian is a matrix of second order derivatives. In this thesis it is of energy is w.r.t. position.

where the first term in the series is the self-energy of an atom, the second is a pairwise interaction and the third term is a three body term etc. As the number of bodies involved increases the contribution to the total energy diminishes such that it becomes possible to truncate the series without loosing significant accuracy. The trick is to truncate the series in order to still describe a system of interest well whilest decreasing computational complexity. Usually functional forms which are parameterised to experiment are used to represent the N-body terms. There are many of these functional forms to choose from and often it is the case that different functional forms describe different classes of materials. One of the first interatomic potentials created is known as the Lennard-Jones potential which approximates the interaction between atoms as a series of 2-body (pairwise) interactions. The Lennard-Jones model has been shown to work well for gases such as Argon [187–189]. The functional form for the Lennard-Jones model is shown below,

$$V_{LJ}\left(\mathbf{r}_{ij}\right) = 4\epsilon\left[\left(\frac{\sigma}{\mathbf{r}_{ij}}\right)^{12} - \left(\frac{\sigma}{\mathbf{r}_{ij}}\right)^{6}\right],$$
(3.6)

where ϵ and σ are parameters which describe the strength and range of the bonding. The general form of this potential is of an attractive r^{-6} part and a repulsive r^{-12} part. The repulsive part is based on the Pauli exclusion principle which states that it is impossible for the wavefunctions of two fermions in the same spin state to overlap. The attractive part is more fundamentally based on the Van de Waals force based on the electrostatic dipole-dipole interaction. Although this potential has serious shortcomings when modelling anything other than inert gases [190] this simple method was the starting point for the whole field of materials modelling. Some parameters for the following materials (Ar, Kr, CH_4, O_2, H_2, C_2H_4) have been determined by Matyushov [191]. Further parameters can be found in Ashcroft-Mermin [64].

3.1.1.1 Buckingham potentials

In this thesis many simulations of ionic materials are performed so an appropriate interatomic potential which describes this bonding type is required. In ionic materials electrons are transferred between atoms, this occurs because this is the most favourable way in which electron shells can be filled. For example in NaCl (or regular salt) sodium is electropositive meaning that it wants to loose electrons, becoming smaller and ionised.

While chlorine is electronegative meaning that it is more favourable to gain electrons and fill its partially filled electron shell becoming larger and an ion. In these materials the bonding is predominately electrostatic in nature. Electrostatic bonding means that short range and long range descriptions of the bonding need to be considered. It has been shown that an adjusted Buckingham-Coulomb functional form can be used to model the interactions in metal-oxides [134, 192]. The Buckingham functional form is shown below,

$$V_{ij}(\mathbf{r}_{ij}) = A_{ij} \exp\left(\frac{-\mathbf{r}_{ij}}{\rho_{ij}}\right) - \frac{C_{ij}}{\mathbf{r}_{ij}^6} + \frac{q_i q_j}{4\pi\epsilon\mathbf{r}_{ij}}, \tag{3.7}$$

where A, ρ and C are parameters of the model, q_i and q_j are the charges of the ions involved, and ϵ is the permittivity. The variables A, ρ and C are parameterised from experimental values such as the cohesive energy and the lattice constant. The increased number of parameters of the Buckingham potential allows for a larger degree of control on how the potential behaves. There is however a drawback by increasing the number of parameters as it becomes possible to over fit the problem, fitting idiosyncrasies. Buckingham potentials have been shown to be effective in bulk, surfaces and GBs. However they are limited in the sense that the charge on each atom is fixed and so is impossible for atoms in these simulation to become polarised or change their charge state. It is possible to extend this model using the shell model potential which allows the ionic charges to polarise during a simulation [193]. These potentials have been very successful in modelling a range of metal oxides including MgO which is studied in this thesis [194–196].

3.1.1.2 The embedded atom method

The EAM is a classical method used to model the interaction between atoms. It expands on the pairwise type potentials such as the Lennard-Jones and Buckingham potentials described previously by adding many-body terms. The many-body terms consider the sum over many atoms in a locality rather than between pairs. It is beneficial over the use of simple pair potentials for many reasons including describing more accurately the relationship between the coordination and the bond energy of metals which is not linear. The EAM also allows the Cauchy condition[2] to be violated which for most metals is positive. At worst the EAM is only twice as computationally expensive as simple pair

---

[2]The Cauchy condition relates two elastic moduli $c_{12} = c_{44}$, where c_{44} is the shear modulus and c_{12} is the transverse expansion.

potentials [29,63]. The total energy of a system of atoms within the EAM is described in the following way,

$$E_{\text{tot}} = \frac{1}{2} \sum_{i,j} V\left(\mathbf{r}_{ij}\right) + \sum_i F_i\left(\rho_i\right), \tag{3.8}$$

$$\rho_i = \sum_j \Phi(\mathbf{r}_{ij}), \tag{3.9}$$

where $V(\mathbf{r}_{ij})$ is a pair potential term which depends on the separation between atoms i and j and F_i is the embedding energy function for atom i. The latter term accounts for the many-body aspects of the atomic binding and is expressed in terms of a sum over atom centred functions $\Phi(\mathbf{r}_{ij})$ which phenomenologically represents the shape of the electron density around a particular atom. Although the EAM was originally designed for use on sp-bonded metals it has been applied to many materials including transition metals. The EAM potentials are usually parameterised by fitting either to experimental data and/or first principles calculations. The EAM offers a good balance between physical accuracy and computational feasibility allowing supercells containing millions of atoms to be simulated in a reasonable time. Extensive research undertaken on transition metals has demonstrated that EAM potentials give an accurate description of many bulk, surface, GB and defect properties [31–34]. It is often the case that many of the potentials do not perform well for situations which are far from the bulk. It is essential that a rigorous testing regime is undertaken to ensure that the correct interatomic behaviour is expected. Such tests include reproducing the cohesive energy, the bulk modulus and the lattice constant. Once these have been found more complex tests must be performed, these are tests such as forcing a different geometric structure upon a material. This should have the effect of giving a higher cohesive energy and hence a less stable structure. Although in theory the EAM potential does not contain the details to know which structural phases should be the most energetically favourable *a priori* [63] EAM potentials are parameterised with the most stable experimental structural phases.

3.1.2 Quantum mechanical modelling

The time independent Schrödinger equation (TISE) for the nuclei and the electrons is one of the most precise and accurate descriptions of the microscopic Universe. The TISE

is shown below,

$$\hat{\mathcal{H}}\Psi = E\Psi,\tag{3.10}$$

$$\hat{\mathcal{H}} = -\frac{1}{2}\sum_n \nabla_{\mathbf{r}_n}^2 - \frac{1}{2}\sum_n \frac{\nabla_{\mathbf{R}_{I_n}}^2}{M_{I_n}} - \sum_{n,m} \frac{Z_{I_n}}{|\mathbf{r}_n - \mathbf{R}_{I_m}|} + \frac{1}{2}\sum_{n\neq m} \frac{1}{|\mathbf{r}_n - \mathbf{r}_m|} + \frac{1}{2}\sum_{n\neq m} \frac{Z_{I_n}Z_{I_m}}{|\mathbf{R}_{I_n} - \mathbf{R}_{I_m}|}$$
$$\tag{3.11}$$

where $\hat{\mathcal{H}}$ is the Hamiltonian (the total energy operator) of the system, Ψ is the many-body wavefunction and E is the total energy. In the terms of the Hamiltonian M_{I_n} is the nuclear mass for nucleon I_n and Z_{I_n} is the atomic number for atom I_n. Ψ depends on the positions of all electrons and nuclei. Quantum mechanical many-body systems are extremely complex and cannot be solved exactly so approximation schemes are required to solve them. As the nuclei are large and slow moving they can be treated classically meaning the quantum mechanical coupling between the nuclei and electrons can be neglected. This approximation is known as the Born-Oppenheimer approximation. In other words the Born-Oppenheimer approximation assumes that the motion of atomic nuclei and electrons in a molecule can be separated ($\Psi = \Psi_{\text{nuclear}} \times \Psi_{\text{electronic}}$). The independent electron approximation can also be employed which treats the dynamics of an individual electron separately to the motion of the other electrons. The independent electron approximation is a truly profound approximation as it means that the many-body Schrödinger equation can be reduced to a system of single electron Schrödinger equations.

3.1.2.1 Hartree and Hartree-Fock theories

In order to solve the single electron Schrödinger equation it is a requirement that the relationship between the single electron wavefunctions or atomic orbitals and the total wavefunction needs to be defined. Hartree theory assumes that it is possible to write the many-body wavefunction for N electrons as a product of single electron wavefunctions shown below,

$$\Psi = \psi_1\psi_2\psi_3\ldots\psi_n,\tag{3.12}$$

where Ψ is the many-body wavefunction and ψ_i are the single electron wavefunctions. The many-body Schrödinger equation reduces to a system of single electron Schrödinger equations shown below,

$$\epsilon_i \psi_i = \left(-\frac{1}{2}\nabla^2 + V_i\right)\psi_i, \tag{3.13}$$

where ϵ_i is the single electron eigenenergy and V_i is the electrostatic potential felt by electron i due to all of the other electrons. In Hartree theory each electron feels a mean field or effective potential from all the other electrons. The effective potential $V_i(r)$ felt by each electron shown below,

$$V_i(\mathbf{r}) = \sum_j \int \frac{n_j(\mathbf{r}')}{|\mathbf{r} - \mathbf{r}'|} d\mathbf{r}', \tag{3.14}$$

where $n_j = \psi_j^* \psi_j$ (the electron density for electron j). The single electron Schrödinger equation can be solved using a self-consistent method to find ψ. Solving equations in a self consistent way involves first guessing the initial electron density then calculating the initial potential. From the potential the single electron wavefunction Schrödinger equations can be solved. The potential is then recalculated using the new density from the previous wavefunction. The process is continued until the input and output wavefunctions are equal to within a small tolerance. One of the drawbacks of Hartree theory is that the potential contains an unphysical self-interaction which occurs from the calculation of the Hartree potential (V_i). The self-interaction error occurs because it is possible for an electron to interact with itself. The self-interaction arises from the electron density n within the potential for when $i = j$ an electron is interacting with itself.

Hartree theory falls down because the wavefunction is not anti-symmetric with respect to exchange[3] [197]. If the wavefunctions are not symmetric with respect to exchange properties such as magnetism cannot be explored and Hunds rules are not recovered. The Fock condition making Hartree-Fock (HF) ensures that the wavefunctions are antisymmetric with respect to exchange. The self-interaction error is also fixed through the addition of the Fock part of the theory. The anti-symmetric principle means the wavefunction changes sign under interchanging of any two electrons (see equation below),

$$\Psi(\mathbf{x}_1, \mathbf{x}_2, \mathbf{x}_3, \ldots, \mathbf{x}_n) = -\Psi(\mathbf{x}_2, \mathbf{x}_1, \mathbf{x}_3, \ldots, \mathbf{x}_n). \tag{3.15}$$

---

[3]From the Pauli exclusion principle for fermions.

It is possible to enforce the anti-symmetry explicitly by building Slater determinants shown below,

$$\Psi(\mathbf{x}_1, \mathbf{x}_2, \mathbf{x}_3, \ldots, \mathbf{x}_n) = \frac{1}{\sqrt{N!}} \begin{vmatrix} \chi_1(\mathbf{x}_1) & \chi_2(\mathbf{x}_1) & \chi_3(\mathbf{x}_1) & \cdots & \chi_n(\mathbf{x}_1) \\ \chi_1(\mathbf{x}_2) & \chi_2(\mathbf{x}_2) & \chi_3(\mathbf{x}_2) & \cdots & \chi_n(\mathbf{x}_2) \\ \chi_1(\mathbf{x}_3) & \chi_2(\mathbf{x}_3) & \chi_3(\mathbf{x}_3) & \cdots & \chi_n(\mathbf{x}_3) \\ \vdots & \vdots & \vdots & \ddots & \vdots \\ \chi_1(\mathbf{x}_n) & \chi_2(\mathbf{x}_n) & \chi_3(\mathbf{x}_n) & \cdots & \chi_n(\mathbf{x}_n) \end{vmatrix},$$

where N is the total number of electrons, $\chi_i(\mathbf{x}_i)$ is a spin orbital defined as the spatial orbital ψ multiplied by the spin wavefunction $\chi = \psi\alpha$ or $\chi = \psi\beta$ where α is an up spin and β is a down spin. Spin can be made intrinsic[4] to Hartree-Fock theory which can be used to compute magnetic properties. From the new definition of the wavefunction by application of the variation principle the new single electron Schrödinger equation can be defined given below,

$$\epsilon_i \psi_i(\mathbf{r}) = \left(-\frac{1}{2}\nabla^2 + V_{ext}(\mathbf{r}) \right) \psi_i(\mathbf{r}) + \sum_j \int d\mathbf{r} \frac{|\psi_j(\mathbf{r}')|^2}{|\mathbf{r} - \mathbf{r}'|} \psi_i(\mathbf{r}) -$$
$$\sum_j \delta_{\sigma_i \sigma_j} \int d\mathbf{r}' \frac{\psi_j^*(\mathbf{r}')\psi_i(\mathbf{r}')}{|\mathbf{r} - \mathbf{r}'|} \psi_j(\mathbf{r}). \quad (3.16)$$

Eqn. 3.16 resolves the problem of self-interaction as now there is an exchange part in the equation which cancels out the self-interaction error. Hartree-Fock theory is much more accurate than Hartree theory but is computationally time consuming to both determine the Slater determinants for increasingly large systems and compute the complicated integrals in the exchange operator (final term in Eqn. 3.16).

3.1.2.2 Density functional theory

In the 1960's Hohenberg and Kohn showed that the ground state electronic energy is determined exactly by the electron density. In other words there is a one to one correspondence between the electron density of a system and its energy. Rather than studying complex many-body wavefunctions which depend on $4N$ variables (3 spatial and 1 spin) which increases exponentially in complexity with the number of electrons it

---

[4]Or removed for nonmagnetic materials to increase the speed of calculations.

is possible to study electron densities which require only 4 variables (3 spatial and spin). It is possible to write down a Schrödinger-like equation where the energy is a functional (a function of a function) of the electron density [198] given below,

$$E[n(\mathbf{r})] = \langle \Psi_0 | \hat{F} + \hat{V}_{\text{ext}} | \Psi_0 \rangle = \langle \Psi_0 | \hat{\mathcal{H}} | \Psi_0 \rangle \geq E_0, \tag{3.17}$$

where Ψ_0 is the groundstate wavefunction, E_0 is the groundstate energy, $\hat{V_{\text{ext}}}$ is the external potential due to the nuclear cores, $n(\mathbf{r})$ is the electron density, $\hat{F} = \hat{U} + \hat{V}_{\text{ee}}$ where U is the kinetic energy operator and $\hat{V}_{\text{ee}}$ is the coulomb interaction between the electrons.

The Hohenberg-Kohn theories are truly remarkable results in modern material science however although very interesting they are not particularly useful as the universal functional $\hat{F}$ is difficult to determine. There was not a significant wait until Kohn and Sham in 1965 determined a method to estimate F [199]. Rather than considering a system of interacting electrons where $\hat{T}$ and $\hat{V}_{\text{ee}}$ are non-linear entities. A system of non-interacting electrons with an adjusted fictitious potential which fixes our electron density such that it is the same as the system with the interacting electrons is considered. The single electron Schrödinger equations can then be solved to find the electron density. In the Kohn-Sham formulation both the kinetic energy operator and the electron-electron interaction become very simple. In a similar vein to Hartree-Fock theory the single electron Schrödinger equation with a modified potential V_{KS} can be written down, shown below,

$$\epsilon_i \psi_i = \left(-\frac{1}{2}\nabla^2 + V_{\text{KS}} \right) \psi_i, \tag{3.18}$$

$$V_{\text{KS}}(\mathbf{r}) = \int \mathrm{d}r' \frac{n(\mathbf{r}')}{|\mathbf{r} - \mathbf{r}'|} + V_{xc}(\mathbf{r}) + V_{\text{ext}}(\mathbf{r}), \tag{3.19}$$

where the first term in V_{KS} is the columbic interaction from all the other electrons, V_{xc} is the exchange correlation potential and V_{ext} is the external potential from the nuclear cores. From this the single electron wavefunction can be estimated using by generating an ansatz of the electronic density defined below,

$$n(\mathbf{r}) = \sum_i^N |\psi_i(\mathbf{r})|^2. \tag{3.20}$$

Usually the ansatz is based on the atomic orbitals of the atom is question. The solution can then be converged using the self-consistent approach by computing the Kohn-Sham potential. Then the modified functional Schrödinger equation can be used to calculate the groundstate energy for the electrons shown below,

$$E[n(\mathbf{r})] = E_{\text{KE}} + \int n(\mathbf{r})V_{\text{ext}}(\mathbf{r})dr + E_{\text{Hartree}}[n(\mathbf{r})] + E_{xc}[n(\mathbf{r})]. \qquad (3.21)$$

Is is faitly straightforward to arrive at Eqn. 3.21 by multiplying Eqn. 3.18 by ψ^*. It is also required to calculate the contributions from the nuclei-nuclei interactions. Note that the difficulties of this theory come from the exchange-correlation energy (XC). This is because the exact form of the XC functional is not known. There are a few good approximations which can be used such as the local density approximation (LDA) shown below,

$$E_{xc}^{\text{LDA}}[n] = -\frac{3}{4}\left(\frac{3}{\pi}\right)^{1/3}\int n(\mathbf{r})^{4/3}dr. \qquad (3.22)$$

The LDA is an integral over all space, with each point contributing to the exchange-correlation energy as if it was a homogenous electron gas of that density. The LDA has been analytically derived in the high and low density limits. Quantum Monte Carlo methods have been used for intermediate densities. For molecular systems the LDA underestimates the exchange energy by around $\sim 10\%$ which can result in smaller theoretically predicted lattice constants than experimental values. It is possible to add spin to the LDA by considering the densities of the spin up (α) and spin down (β) electrons individually. The local spin density approximation (LSD) is given as,

$$E_{xc}^{\text{LSD}}[n] = -2^{1/3}\frac{3}{4}\left(\frac{3}{\pi}\right)^{1/3}\int \left(n(\mathbf{r})_\alpha^{4/3} + n(\mathbf{r})_\beta^{4/3}\right) dr. \qquad (3.23)$$

There is also the generalised gradient approximation (GGA). The GGA adds the first order derivative of the density to the approximation of the exchange correlation functional. There are many different GGA functionals which can be parameterised using experimental data from rare gases, the helium atom or can derived from theoretical results. In this thesis the parameterization of Perdew, Burke and Ernzerhof (PBE) has been used to describe the exchange correlation energy [200]. GGA exchange correlation functionals can reduce the error in the exchange energy relative to the LDA by up to two orders of magnitude [197].

DFT suffers from self-interaction error because the Hartree potential used to compute part of a system's energy contains an integral over the product of a charge density and a wavefunction where electron density is indexed over all electrons in the system. In theory the self-interaction error should cancel with the exchange correlation functional if it were exact. But as the XC functional is an approximation a small contribution to the self-interaction error remains. In the 1990s it was proposed that because in Hartree-Fock theory there is no self-interaction error due to the Fock exchange operator a fraction of Hartree-Fock exchange could be added into DFT to improve the XC functionals. These new functionals are known colloquially as hybrids. The hybrid exchange-correlation functional for the LSD is shown below,

$$E_{xc}^{\text{hyb}} = E_{xc}^{\text{LSD}} + a_0(E_x^{\text{exact}} - E_x^{\text{LSD}}), \qquad (3.24)$$

where the subscript xc refers to the exchange correlation and the subscript x refers to the exchange only. The amount of exchange a_0 added is usually determined by fitting to experiments but in many cases is between 20-30%. Because of these changes hybrids estimate many physical properties much better than the LDA(GGA) such as lattice constants and band gaps. However there are a few drawbacks to hybrids as many have argued that HF and DFT are two very different theories which are being combined to get the right answer experimentally making the method less *ab-initio*. Furthermore since the Fock exchange operator needs to be computed the calculations are very expensive. The Heyd Scuseria Ernzerhof (HSE) exchange-correlation functional is a computationally cheaper alternative to other hybrid exchange correlational functions. It uses an error function screened Coulomb potential to calculate the exchange portion of the energy to improve computational efficiency, especially for metallic systems. It is defined in the following way,

$$E_{xc}^{\text{HSE}} = a_0 E_x^{\text{HF,SR}}(\omega) + (1 - a_0)E_x^{\text{PBE,SR}}(\omega) + E_x^{\text{PBE,LR}}(\omega) + E_c^{\text{PBE}}, \qquad (3.25)$$

where a is the mixing parameter and ω is an adjustable parameter controlling the range of the interaction. Standard values of $a_0 = \frac{1}{4}$ and $\omega = 0.2$ (usually referred to as HSE06) have been shown to give good results for most systems. $E_x^{\text{HF,SR}}(\omega)$ is the short range Hartree-Fock exact exchange functional, $E_x^{\text{PBE,SR}}(\omega)$ and $E_x^{\text{PBE,LR}}(\omega)$ are the short and long range components of the PBE exchange functional, and $E_c^{\text{PBE}}(\omega)$ is the PBE correlation functional [201, 202].

Plane wave basis

To perform calculations in both DFT and HF a representation of the wavefunction must be selected. A representation can be chosen by picking a basis set. In atomistic modelling no basis set is complete (i.e. does not represent the wavefunction perfectly). In this thesis plane waves are used as they have a good systematic convergences, good computational scaling, simple operations, easy calculations of forces and are bias free. Bloch's theorem states that the wavefunction of an electron within a perfectly periodic potential may be written as,

$$\psi_{j,k}(\mathbf{r}) = u_j(\mathbf{r})e^{i\mathbf{k}\cdot\mathbf{r}}, \tag{3.26}$$

where $u(\mathbf{r})$ is a function that possesses the periodicity of the potential, i.e. $u(\mathbf{r}+\mathbf{l}) = u(\mathbf{r})$, where $\mathbf{l}$ is a lattice vector of the unit cell. In Eqn. 3.26 $i = \sqrt{-1}$ and $\mathbf{k}$ is a wavevector. Since $u(\mathbf{r})$ is a periodic function, we may expand it in terms of a Fourier series,

$$u_j(\mathbf{r}) = \sum_G \mathbf{c}_{j,G}e^{i\mathbf{G}\cdot\mathbf{r}} \tag{3.27}$$

where the $\mathbf{G}$ are reciprocal lattice vectors defined through $\mathbf{G}\cdot\mathbf{R} = 2\pi m$, where m is an integer, $\mathbf{R}$ is a real space lattice vector and the $\mathbf{c}_{i,G}$ are plane wave expansion coefficients. The electron wavefunctions may therefore be written as a linear combination of plane waves:

$$\psi_{j,k}(\mathbf{r}) = \sum_G \mathbf{c}_{j,G}e^{i(\mathbf{k}+\mathbf{G})\cdot\mathbf{r}}. \tag{3.28}$$

It is possible to define a cut-off energy for the $\mathbf{G}$ vectors to truncate the number of plane waves required shown below,

$$\frac{1}{2}\mathbf{G}^2 \geq E_{\text{cut}}, \tag{3.29}$$

where E_{cut} is the cut-off energy. In all calculations a convergence process should be undertaken whereby the cut-off energy is increased and the total energy is calculated for a given system. Appropriate cut-off energies are chosen when the total energy becomes approximately constant w.r.t. cut-off [203].

k-points

Given that each electron occupies a state of definite k, the infinite number of electrons within the solid gives rise to an infinite number of k-points. However, one does not need to consider all of these k-points as the electron wavefunctions will be almost identical for

values of k that are sufficiently close. It is therefore sufficient to consider the electronic states at a finite number of k-points to determine the electron density of the solid. It is possible to define a mesh of k-points equidistant in each reciprocal direction. Such a method is called Monkhorst-Pack (MP) mesh and requires only the number of k-points in each direction. It is important to centre the MP grid at the gamma point for certain calculations in for example in MgO (as this is a direct gap insulator so the smallest band gap is found at the gamma point.). Convergence of the total energy with respect to the number of k-points must be performed to ensure that the wavefunctions describe the physics of a given system correctly [203].

Psuedopotentials

The majority of the physical properties of solids depend on the valence electrons. It is possible to partition the electrons between core and valence states because the core electrons are almost environment independent. The pseudopotential approximation in DFT can be introduced by replacing the core electrons and ionic potential with a pseudopotential that acts on a set of pseudo wavefunctions. The pseudopotential is constructed such that that the pseudo wavefunction has no radial nodes within the core region and that the pseudo wavefunctions and potential agree with the true wave function and potential outside some cut-off radius r_{cut}. Further, the pseudopotential must preserve the atomic properties of the element, including phase shifts on scattering across the core; as these phase shifts will in general be dependent upon the angular momentum state. In general a pseudopotential must be non-local, i.e. it must have projectors for the different angular momentum states. The most general form for a pseudopotential is,

$$\Psi = \Psi_{\mathrm{pseudo}} \times \Psi_{\mathrm{valence}}, \tag{3.30}$$

where Ψ_{pseudo} is the pseudopotential part of the wavefunction and Ψ_{valence} are the valance electrons. The use of a pseudopotential greatly simplifies the computational complexity of many systems and has been shown to be very accurate when compared to all electron calculations[5] [204].

---

[5]Without a pseudopotential.

Density of states

The density of states (DOS) describes the total number of occupied and unoccupied states at each energy level. In DFT it is possible to count the number of states which exist in a particular system in a particular energy range. It is useful as it allows us to classify a material into metal, semi-metal, semi-conductor or insulator by inspecting the band gap. In a DFT calculation the density of states can be extracted by inspecting the eigenvalues of the wavefunction,

$$n(\epsilon_i) = (N(\epsilon_i) - N(\epsilon_{i-1}))/\Delta\epsilon, \tag{3.31}$$

$$N(\epsilon_i) = \int_{-\infty}^{\epsilon_i} n(\epsilon)d\epsilon, \tag{3.32}$$

where ϵ is a given energy level, $n(\epsilon)$ is the local density of states, $N(\epsilon)$ is the integrated density of states and $\Delta\epsilon$ is the distance between two discrete grid points.

Bader analysis

As the electron density in a DFT calculation represents an amalgamation of individual electronic orbitals the atomic charges are not observables. Knowledge of the electronic charges in a system is extremely important to understand phenomena such as charge transfer. It is not obvious how electronic density should be partitioned to calculate the electronic charges on the atoms. Many different schemes have been proposed such as: Mulliken population analysis, density matrix based normal population analysis, Bader analysis and Hirshfeld analysis. In this thesis Bader analysis has been used to partition the electron density to predict the atomic charges. Bader analysis works by separating systems into atom centred charge distributions by a zero-flux surface defined as,

$$\nabla\rho(\mathbf{r}_s) \cdot n(\mathbf{r}_s) = 0, \tag{3.33}$$

where ρ is the charge density, $\mathbf{r}_s$ is a point on the surface S and $n(\mathbf{r}_s)$ is the unit vector normal to the surface at $\mathbf{r}_s$ [205].

3.2 Code used in this thesis

CASTEP

CASTEP (CAmbridge Serial Total Energy Package) is a first principles code used to calculate the properties of materials. It implements DFT and can model a wide range of material properties including total energies, structure, electronic and magnetic properties. CASTEP uses a plane wave basis set to expand the Kohn-Sham wavefunction [206].

VASP

The Vienna Ab initio Simulation Package, also known as VASP, is a package for performing first principles calculations using the projector augmented wave method with a plane wave basis set [207]. It implements DFT, but also contains many post-DFT corrections such as hybrid functionals and many-body perturbation theory (GW).

LAMMPS

The Large-scale Atomic/Molecular Massively Parallel Simulator (LAMMPS) code [208] is a classical molecular dynamics code that can model a range of systems using classical interatomic potential methods and different boundary conditions. In this thesis the code was mainly used to model metals using the EAM formalism. LAMMPS requires that interatomic potentials are supplied in a tabulated format so a simple code written in C++ which tabulates each potential from its parameters was developed. Many pre-existing tabulated potentials can be found on the National Institute for Standards and Technology (NIST) website [209].

VESTA

Visualisation for Electronic STructure Analysis (VESTA) is a powerful tool used to visualise crystals and molecules [210]. VESTA has the ability to visualise most file formats including both CASTEP (.cell) and VASP (POSCAR). However for LAMMPS a new code was written to convert from the .lammpstrj file to a VESTA appropriate input. VESTA has the ability to show iso-surfaces, draw bonds and offers a significant amount of customisation.

VMD

Visual Molecular Dynamics (VMD) is a useful tool to visualise and analyse crystallographic systems. It may be used to view more general molecules, such as LAMMPS trajectory formats and display the structure. VMD provides a wide variety of methods for rendering and colouring a molecule: simple points and lines, CPK spheres and cylinders, liquorice bonds, backbone tubes and ribbons, cartoon drawings, and others. VMD can be used to animate and analyse the trajectory of a molecular dynamics (MD) simulation. In particular, VMD can act as a graphical front end for an external MD program by displaying and animating a molecule undergoing simulation on a remote computer [211].

GULP

General Utility Lattice Program (GULP) is a useful code which allows classical simulations of atoms. It has many useful features such as the ability to automatically calculate the elastic constants [136]. A variety of force fields can be used within GULP spanning the shell model for ionic materials, molecular mechanics for organic systems and the embedded atom model for metals.

Bader analysis

It is possible using techniques developed by Richard Bader to divide the electronic density from clusters of atoms such as those in GBs into individual atom centred charge densities. Bader's method defines an atom based on the total electronic charge density and uses a zero flux surface to divide the atoms. A zero flux surface is a 2-D surface on which the charge density is a minimum perpendicular to the surface. Dr Henkelman's group in Texas have developed a program to perform Bader analysis from the output files of VASP calculations. This offers a convenient way to analyse the results from VASP to show the charges present on atoms in ionic structures [212].

Chapter 4

Excess volume due to grain boundaries in metals

4.1 Introduction

GBs in metals play an extremely important role in determining their properties and functionality. As discussed in Sec. 2.1.3 the excess volume at GBs influences phenomena such as segregation, diffusion and embrittlement in metals. However until recent experiments by Steyskal and Oberdorfer it has been challenging to probe the excess volume in real materials directly [42, 43]. In these investigations a difference of 0.14 Å between the average excess volumes of Cu and Ni has been detected. The difference in the lattice constants is insufficient to explain the differences in the excess volume and an atomistic explanation of this observation is currently missing [88]. Understanding the factors which influence the excess volume could have many important benefits not least for materials design relevant to many technological applications such as fusion reactors.

In this chapter a detailed theoretical investigation into GB excess volume in the polycrystalline metals Fe, Cu and Ni is presented. These materials are chosen to allow comparison with previous theoretical and experimental studies, and due to their numerous applications in areas such as spintronics, fusion, fission, power generation and catalysis [213–216]. The focus is on symmetrical tilt GBs over a wide range GB orientations to draw out trends across the three materials. By employing an automated computational approach based on an EAM description of interatomic interactions [85, 217] the stable structures of over 400 distinct symmetrical tilt GBs for Fe, Cu and Ni are determined. The validity of the approach is demonstrated by comparison to first principles calcula-

tions of GB properties using DFT. The results recover a systematic difference in excess volume of between 0.1 and 0.2 Å between Cu and Ni which is in very good agreement with experimental data. By analysing the strain at the atomic level it is demonstrated that the excess volume difference is localised in a region of 5 - 10 Å around the GB plane. A semi-quantitative explanation for the origin of the difference in terms of the differing bulk moduli of Cu and Ni (138 GPa and 186 GPa respectively) is provided. While Cu and Ni are fcc, Fe is bcc and therefore GBs have different geometric structures. The localisation of GB cusps[1] in Fe is also different to Cu and Ni. The range of excess volumes in Fe is comparable to Ni.

The rest of this chapter is structured in the following way. In Secs. 4.2.1 & 4.2.2 the approach is validated by looking at several examples of GBs in Fe, Cu and Ni. From Sec. 4.2.3 the results are presented. In Sec. 4.3 the results are discussed and in Sec. 4.4 the chapter is concluded.

4.2 Results

4.2.1 Interatomic potential validation

Numerous EAM potentials have been developed for Fe, Cu and Ni. A systematic investigation of corresponding predicted properties to determine the most appropriate to employ in this study has been performed. The ability of different potentials to describe bulk properties such as the lattice constant, the cohesive energy, the bulk moduli as well formation energies of low-index surfaces has been assessed. All calculations have a convergence tolerance of 1×10^{-6} eV for total energies and < 0.001 Å for cell volumes (see Sec. 3.1.1.2). The precision of the cell volumes is important for calculations which involve adjusting the size of the cell.

The cohesive energy of a monoatomic solid in a classical simulation is calculated by computing the total energy of a bulk periodic supercell which has been optimised with respect to the cell volume and the atomic positions of all of the atoms then divided by the total number of atoms,

$$E_{\text{coh}}^{\text{Classical}} = \frac{E_{\text{total}}}{N_{\text{atoms}}}. \tag{4.1}$$

---

[1]Crystallographic orientations which are particularly high or low in formation energy relative to nearby orientational configurations.

The bulk modulus is calculated by fitting the volume dependence of total energy to the Birch-Murnaghan equation of state [218] shown below,

$$E\left(V\right) = E_0 + \frac{9V_0 B_0}{16} \left\{ \left[\left(\frac{V_0}{V}\right)^{\frac{2}{3}} - 1 \right]^3 B' + \left[\left(\frac{V_0}{V}\right)^{\frac{2}{3}} - 1 \right]^2 \left[6 - 4\left(\frac{V_0}{V}\right)^{\frac{2}{3}} \right] \right\}, \quad (4.2)$$

where E_0 is the cohesive energy, B_0 is the bulk modulus, V_0 is the equilibrium volume of the primitive cell and B' is the first pressure derivative of the bulk modulus. The first pressure derivative of the bulk modulus is a quantity which describes the anharmonicity of the energy volume curve, important for phenomena such as shockwaves. Higher orders of the bulk moduli become more important in areas where the pressure is changing rapidly such as the centre of planets and stars but also in GBs as it can alter the interfacial geometry.

First principles calculations within the formalism of DFT are also employed to calculate the properties of Fe, Cu and Ni (discussed in detail in Sec. 3.1.2.2) [198,199]. Calculations have been performed using CASTEP [219]. Ultrasoft pseudopotentials model the inner electrons and $3d$ and $4s$ valence electrons are treated explicitly. The GGA with the parameterisation of PBE has been used to describe the exchange correlation energy [200]. To determine the bulk properties of the metals the wavefunctions are expanded in a plane-wave basis with energies up to 500 eV and a Monkhorst-Pack k-point grid of $12 \times 12 \times 12$ for primitive cells and structures are optimised using the limited-memory Broyden Fletcher Goldfarb Shanno (LBFGS) algorithm [220].

In a DFT calculation the energy of the infinitely separated system is not zero like in the classical simulation. To compute the cohesive energy in DFT the difference in energy between a bulk system and one of isolated atoms which are effectively infinitely separated should be taken. In practice this means that supercells containing only a single atom surrounded by at least 10 Å of vacuum in each direction are constructed. The cohesive energy ($E_{\text{coh}}^{\text{DFT}}$) is calculated as,

$$E_{\text{coh}}^{\text{DFT}} = \frac{E^{\text{Bulk}}}{N_{\text{atoms,Bulk}}} E^{\text{Isolated}}, \quad (4.3)$$

where N_{atoms} is the total number of atoms in either the bulk or isolated systems, E^{Bulk} is the total energy of the bulk and E^{Isolated} is the total energy of the isolated system. The bulk energy as a function of interatomic separation are compared between the EAM and DFT in Fig. 4.1.

Surfaces are modelled using a similar approach to the one described for GBs in Sec. 2.1 however only one grain (more commonly referred to as a slab in surface calculations) is included and PBC are employed in all directions. The surface energy is defined in the same way as the GB formation energy using Eq. 2.2. Surface energies have been fully converged with respect to slab thickness. Surface energies are calculated with a k-point grid of 1×9×9, 1×8×8 and 1×6×4 for (100), (110) and (111) surfaces respectively with a cut-off energy of 500 eV. To compute surface energies in a DFT plane wave code a slab with a large vacuum gap should be constructed and compared with a system with no gap. The DFT predicted bulk and surface properties are included in Table. 4.1 and comparison with the EAM potential and experimental values demonstrates good agreement across the board.

For GB structures the plane-wave basis cut-off is set to 350 eV and MP k-point grids of 1×3×3 are employed (with only one k-point along the non-periodic GB normal direction). The EAM optimised supercells have in-plane dimensions corresponding to the EAM optimised bulk lattice constants. These supercells must be scaled to reflect the optimised DFT lattice constant which in general may differ slightly. GB formation energies have been calculated by comparing the total energy difference between a supercell containing a GB and a bulk supercell of the same size. This minimises the error associated with differing k-point sampling and basis sets.

Table 4.1: Summary of properties calculated using various embedded atom method potentials (S-C Sutton and Chen, Ack Ackland, C-R Cleri Rosato, F-S Finnis Sinclair, Mend Mendelev) for Fe, Cu and Ni. E_{coh} (eV) is the cohesive energy, a (Å) is the lattice constant, B_0 (GPa) is the bulk modulus, γ_{hkl} (Jm^{-2}) is the surface energy relating to surface (hkl), $\Delta a_{\text{fcc/bcc}}$ is the ratio of the lattice constants of the bcc and fcc phases and, $\Delta E_{\text{fcc-bcc}}$ is the difference between the cohesive energies of the bcc and fcc phases.

Cu	Expt. [1] [2] [3] [4]	DFT	S-C	Ack.	C-R
E_{coh}	-3.54	-3.70	-3.49	-3.52	-3.54
$\Delta E_{\text{fcc-bcc}}$		0.05	0.03	0.04	0.03
a_{fcc}	3.62	3.63	3.62	3.62	3.61
$\Delta a_{\text{fcc/bcc}}$		1.26	1.25	1.26	1.25
B_0	138	139	135	144	142
γ_{001}		1.33	1.22	1.14	1.36
γ_{011}		1.48	1.29	1.23	1.47
γ_{111}		1.25	1.14	0.95	1.27
Fe	Expt.	DFT	F-S	Ack.	Mend.
E_{coh}	-4.28	-5.30	-4.28	-4.31	-4.12
$\Delta E_{\text{fcc-bcc}}$		-0.15	-0.11	-0.05	-0.12
a_{bcc}	2.87	2.85	2.87	2.87	2.85
$\Delta a_{\text{fcc/bcc}}$		1.22	1.27	1.30	1.28
B_0	168	177	106[5]	179	169
γ_{001}		2.62	1.69	1.80	1.78
γ_{011}		2.59	1.51	1.58	1.64
γ_{111}		2.91	1.92	1.99	1.99
Ni	Expt.	DFT	S-C	Mend.	C-R
E_{coh}	-4.44	-4.92	-4.43	-4.39	-4.43
$\Delta E_{\text{fcc-bcc}}$		0.05	0.02	0.09	0.12
a_{fcc}	3.52	3.52	3.52	3.52	3.52
$\Delta a_{\text{fcc/bcc}}$		1.25	1.25	1.27	1.25
B_0	186	200	192	174	186
γ_{001}		2.30	1.64	1.41	2.62
γ_{011}		2.35	1.73	1.59	2.78
γ_{111}		1.97	1.53	1.28	2.60

[1] Standard reference for experimental physical quantities; lattice constants, cohesive energies and bulk moduli [221].

[2] Listing of experimental lattice constants [222].

[3] Listing of experimental cohesive energies [223].

[4] Experimental measurements of elastic properties of Fe, Cu and Ni [224–226].

[5] It is noted here that a correction made to the FS potential for iron in 1986 [227] which improves the agreement of the bulk modulus with experiment.

Table 4.1 summarises properties calculated using a range of potentials for Fe, Cu and Ni. These include the Finnis and Sinclair (FS) [30], Ackland [34] and Mendelev [228] potentials for iron; and the Johnson [229], Sutton and Chen [33], Cleri and Rosato [32], Ackland [31] and Mendelev [228] for copper and nickel. It is found that the Ackland potential describes the properties of iron and copper more accurately than the others. This potential is fitted to the lattice parameter a, three important elastic constants C_{11}, C_{12}, C_{44}, the cohesive energy E_{coh} and the unrelaxed vacancy formation energy. The Ackland potential has a cut-off value $r_{\mathrm{c}} = 4.43$ Å for copper and $r_{\mathrm{c}} = 3.73$ Å for iron. Results for this potential can be found in Table 4.1. For nickel it is found that the Mendelev potential describes the properties more accurately. This is initially parameterised in the same way as the Ackland potential, however the weighting of the solid properties is reduced in order to allow the system to describe the liquid phase. The Mendelev potential has a cut-off value $r_{\mathrm{c}} = 6.0$ Å for nickel.

To further demonstrate how DFT and the EAM differ the EAM and DFT energy-volume curves near equilibrium for each metal in the bcc and fcc structures are shown in Fig 4.1. This is undertaken by performing single point calculations on scaled values of the lattice constant of each material in both bulk structures. A range of $\pm 20\%$ strain of the lattice constant is shown. This range of strain is of the order found in GBs. It is observed that for Cu there is an extremely good agreement between DFT and EAM in the absolute position and the gradient of the potential, for Fe there is a systematic shift of around 0.8 eV suggesting that DFT over predicts the cohesive energy and for Ni there is a small shift of 0.4 eV suggesting a very good agreement between DFT and EAM. In Ni there is a large divergence as the material becomes compressed by 15% however it has been shown that bonds in GBs are unlikely to be compressed to this degree. Since it is the gradient which determines how easily a material can be compressed and expanded it is expected that materials with larger gradients to be more resistive to strain. The distribution of bond lengths present in GBs should be wider in Cu when compared to Fe and Ni. It is expected that the distribution of bond lengths should be similar in Fe and Ni.

4.2.2 Determination of grain boundary structure and properties

In this section the approach for determining the stable structures of arbitrary symmetrical tilt GBs is illustrated by describing a number of examples in detail. First a
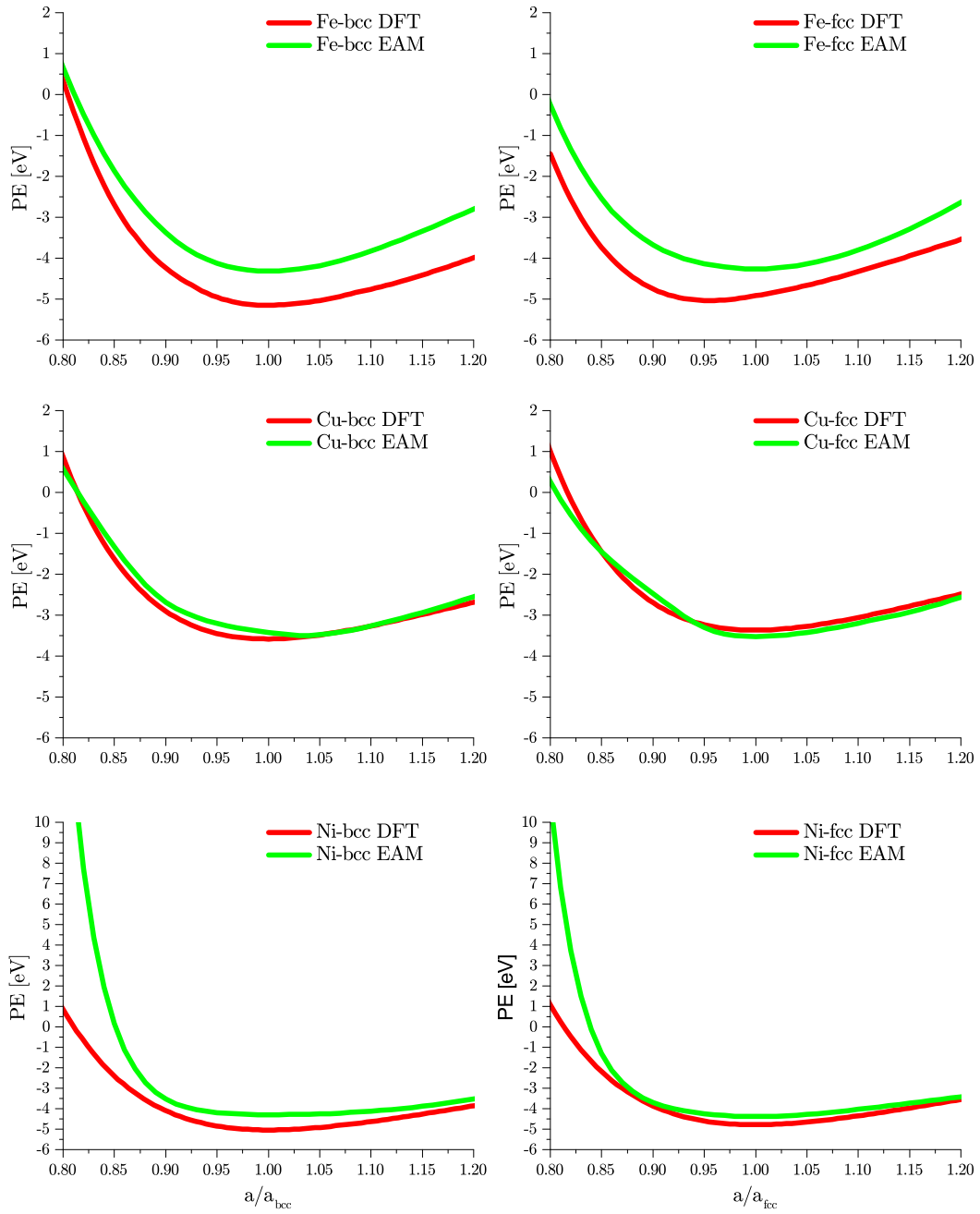
Figure 4.1: Energy-volume curves near equilibrium for the bcc and fcc structures Fe, Cu and Ni using the embedded atom method and density functional theory. For Fe and Cu the Ackland potentials is used and for Ni the Mendelev potential is used.

Ni(210)[001] GB is considered. A systematic screening approach (explained in detail in Sec. 2.1.2) identifies three inequivalent low formation energy structures as shown in Fig. 4.2. The structures are labelled a-c ordered according to their formation energy. The most stable GB structure Ni(210)[001]-a (γ =1.38 Jm^{-2}) has no rigid body translation between the two crystals and is fully symmetric about the interfacial plane. The GB can be viewed as a periodic arrangement of triangular structural units as indicated in the figure. The next most stable structure Ni(210)[001]-b (γ =1.43 Jm^{-2}) is formed from diamond shaped structural units. Finally GB structure Ni(210)[001]-c (γ =1.70 Jm^{-2}) has one grain which has a rigid body translation of $a/2[\bar{1}20]$ with respect to the other and is not mirror symmetric. The GB can be viewed as a periodic arrangement of two irregular quadrilaterals.
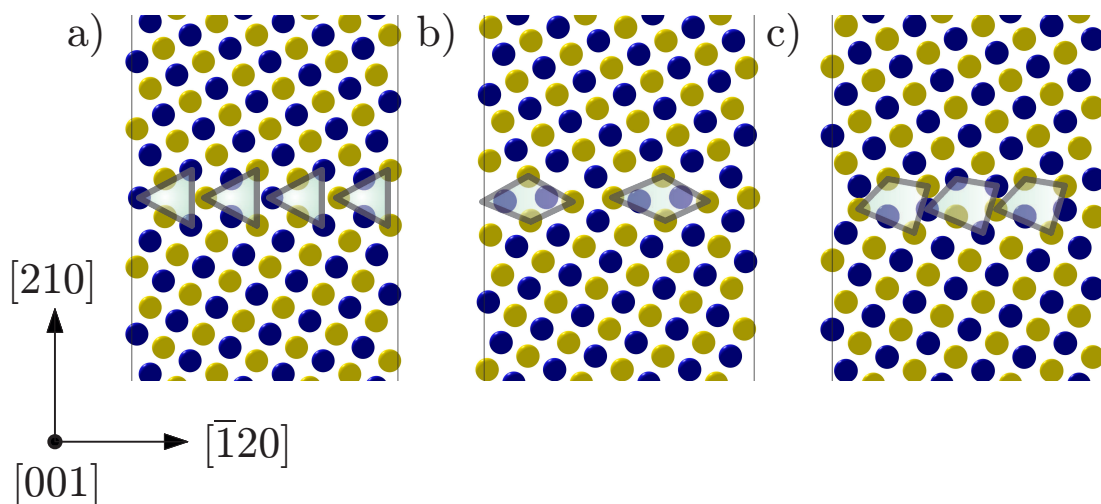
Figure 4.2: Embedded atom method optimised structures of the nickel (210)[001] grain boundary. The yellow and blue atoms indicate atoms in different planes perpendicular to the tilt direction [001], with the structural units highlighted. The three most stable grain boundary structures are shown (a-c).

DFT calculations on these structures predict the same ordering in energy as using the EAM approach. The GB formation energies calculated at the EAM and DFT levels are very consistent (differing by less than 0.2 Jm^{-2}). The corresponding excess volumes calculated at the DFT and EAM levels are in good agreement (differing by less than 0.12 Å). The predicted stable structure is also consistent with previous EAM based studies [230]. To further verify the approach stable structures for the (111)[101], (121)[101] and (210)[001] symmetrical tilt GBs in Fe, Cu and Ni have been determined in a similar

way. It is noted that the (111)[101] GB in the fcc materials copper and nickel should correspond to twin boundaries with a very low formation energy, this is confirmed by the systematic screening approach. The twin GB is a structural feature of many materials and actually corresponds to a stacking fault[2]. Table. 4.2 summarises the calculated formation energies and excess volumes for three GBs at both the EAM and DFT levels of theory. The DFT and EAM determined GB formation energies are very similar and predict the same relative stability of the three GB types for each material. The calculated excess volumes again differ more significantly (with the DFT values being in general lower however again the relative ordering is consistent). The only exception is the Cu(210)[001] GB for which the DFT and EAM approaches predict different structures as the most stable. Fig. 4.3 shows the two alternative structures of the Cu(210)[001] GB. Structure Cu(210)[001]-a ($\gamma = 0.96$ Jm^{-2}) is mirror symmetric and consists of a periodic arrangement of diamond structural units. Structure Cu(210)[001]-b ($\gamma = 1.07$ Jm^{-2}) is also mirror symmetric and consists of a periodic arrangement of triangular structural units. The latter structure is the only one to have been reported previously on the basis of EAM calculations [231–233]. The energetic ordering of these two possible interfaces is swapped at the DFT level (Table 4.2) however the difference in energy remains very small (0.06 Jm^{-2}) at the DFT level and 0.11 Jm^{-2} at the EAM level. This suggests that thermodynamically both structures may coexist.

The results presented in this section demonstrate that the systematic screening approach of creating GBs (see Sec. 2.1.2) can determine the stable structures of arbitrary tilt GBs and the calculated formation energies and excess volumes at the EAM level are broadly consistent with first principles based calculations. The results in Table II are also consistent with other studies on GBs in the literature [26, 84, 85, 92, 233–236]. This demonstrates the reliability of the EAM approach.

4.2.3 Excess volume in Fe, Cu and Ni

The process of determining stable GB structures is scaled up to consider a series of GBs of the general type $(hkl)[mno]$ in Fe, Cu and Ni. Supercells defined by the integers h, k, l, m, n and o ranging from 1 to 20 are considered. The search space is also reduced to supercells with less than 15,000 atoms (400 distinct orientations for each material).

---

[2]The pattern of atomic layers is ABCBA rather than ABCABC at the GB.
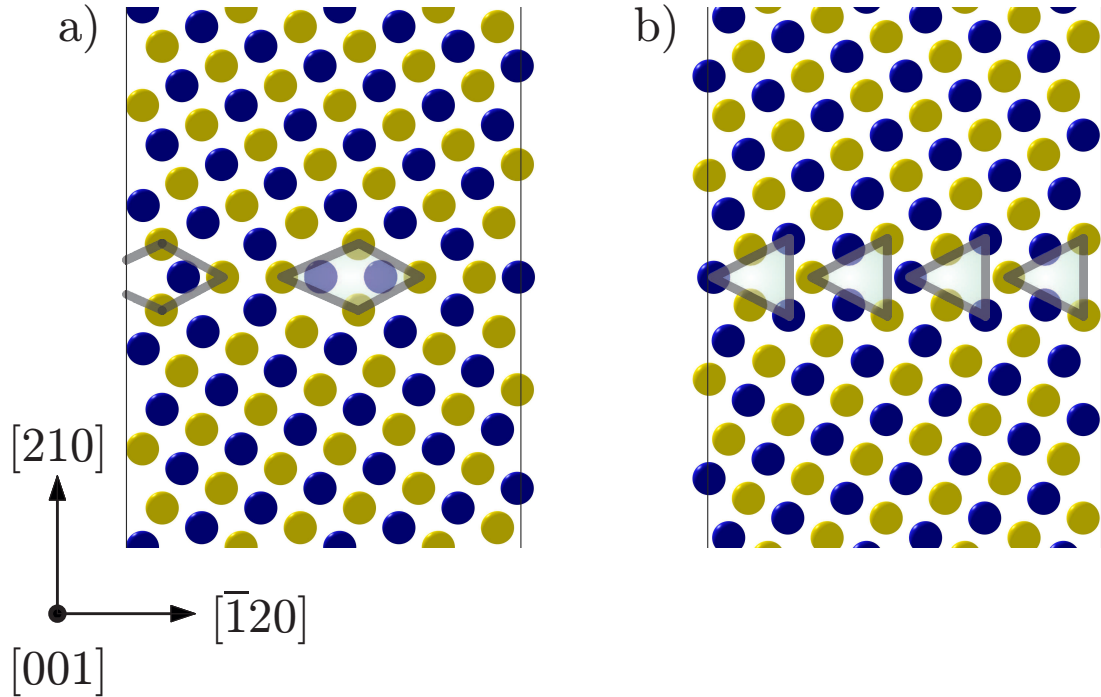
Figure 4.3: Embedded atom method optimised structures of the copper (210)[001] grain boundary. The yellow and blue atoms indicate atoms in different planes perpendicular to the tilt direction [001], with the structural units highlighted. The two most stable GB structures are shown (a-b).

Only orthogonal GBs are considered so it must ensured that the dot product of (hkl) and $[mno]$ is zero. Due to symmetry of cubic crystals there are no integer reflections e.g. $(210) = (120)$ as these are structurally identical GBs. The grains also need to be large enough that the GBs do not interfere with each other. It is found that a granular thickness of 30 Å is sufficient to ensure GBs do not interfere with each other. A task farming algorithm is implemented within LAMMPS to compute the excess volume and GB formation energy for each system [208].

In Fig. 4.4 the GB formation energy and the excess volume across all of these orientations for Fe, Cu and Ni is shown. Broadly speaking there is a linear correlation between GB formation energy and excess volume which becomes pronounced in the low formation energy limit, in agreement with previous theoretical calculations [237]. However it is observed that there is a stark difference between the range of excess volumes in Cu and Ni, with Cu being on average 40% larger. By contrast Fe occupies a similar

Table 4.2: Comparison of embedded atom method and density functional theory predictions of excess volume δV (Å) and GB formation energy γ (Jm^{-2}) for a number of tilt GBs in Fe, Cu and Ni.

Cu	γ_{DFT}	γ_{EAM}	δV_{DFT}	δV_{EAM}
(111)[101]	0.02	0.02	0.01	0.04
(121)[101]	0.57	0.77	0.17	0.29
(210)[001]-a	0.92	0.96	0.24	0.36
(210)[001]-b	0.86	1.07	0.34	0.36
Fe	γ_{DFT}	γ_{EAM}	δV_{DFT}	δV_{EAM}
(111)[101]	1.38	1.50	0.23	0.29
(121)[101]	0.31	0.29	0.09	0.06
(210)[001]	1.31	1.22	0.42	0.40
Ni	γ_{DFT}	γ_{EAM}	δV_{DFT}	δV_{EAM}
(111)[101]	0.04	0.10	0.01	0.02
(121)[101]	0.84	1.02	0.10	0.07
(210)[001]	1.23	1.38	0.35	0.36

distribution of points to Ni.
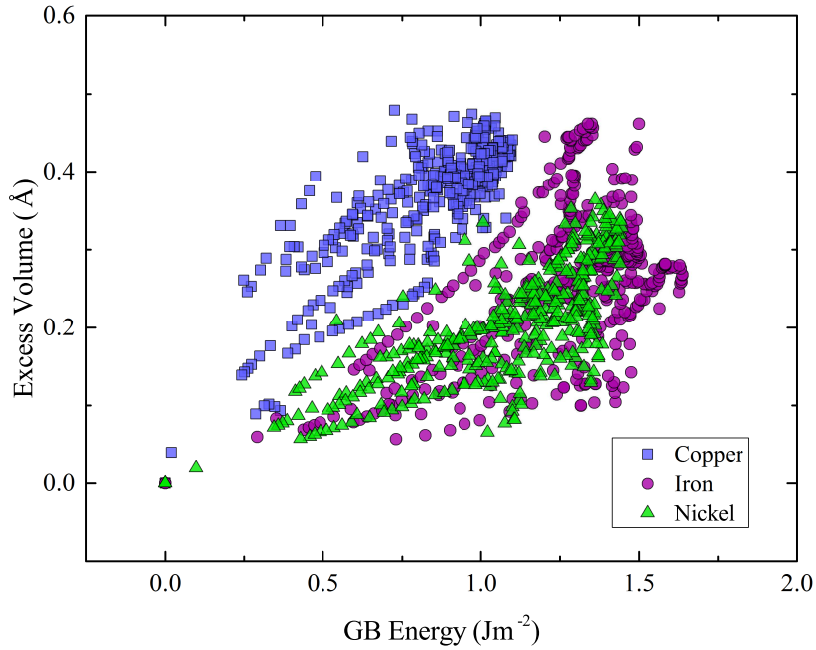
Figure 4.4: Correlation between grain boundary formation energy (Jm^{-2}) and excess volume (Å) for 400 unique stable grain boundaries in Fe, Cu and Ni. Cu has systematically higher excess volumes than Ni, Fe is comparable to Ni.

The variation of excess volume with respect to GB orientation can be illustrated by mapping each GB orientation onto a unit sphere [76, 84]. Once in spherical coordinates a projection on to a circle using a Lambert azimuthal equal area projection (LP) can be performed [77]. The methodology for the construction of this projection is given in the Sec. 2.1.4. Fig. 4.5 shows the result for Cu and Ni, recognising that due to symmetry it is only necessary to show an irreducible sector of the circle. It is noted that the set of 400 GB orientations considered span the perimeter and most of the area inside this irreducible sector. Fig. 4.5 also helps further highlight that the excess volume is systematically larger in Cu than Ni.
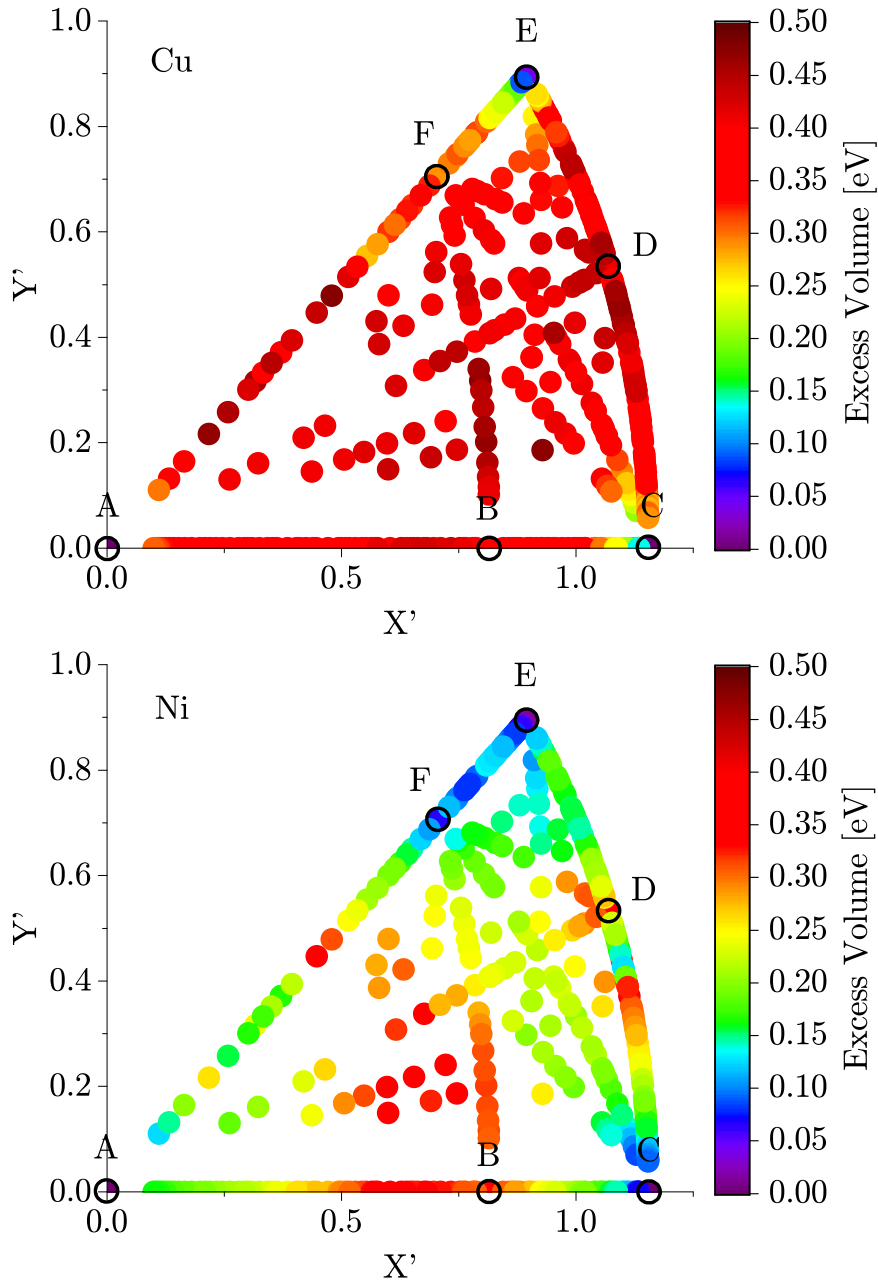
Figure 4.5: Lambert azimuthal projection showing the variation of excess volume with grain boundary orientation for Cu and Ni. X′ and Y′ are coordinates in this projection which represent a mapping from the Miller index definition $(hkl)[mno]$ (see Sec. 2.1.4). High symmetry orientations are labelled on the figure as follows: A($(100)[001]$), B($(210)[001]$), C($(101)[010]$), D($(212)[101]$), E($(111)[101]$) and F($(131)[101]$).

In Fig. 4.6 the stereographic projection for Fe is shown. When compared to the projections in Cu and Ni (Fig. 4.5) there is a clear difference between Fe and, Cu and Ni in where low excess volumes are located. For Fe (Fig. 4.6) there is a minima of excess volume located between the points C and F but for Cu and Ni the minima lies between points E and F (Fig. 4.5). The difference in the excess volume projections in Cu and Ni, and Fe is a purely structural effect and is exactly the difference between the bcc and fcc lattices.
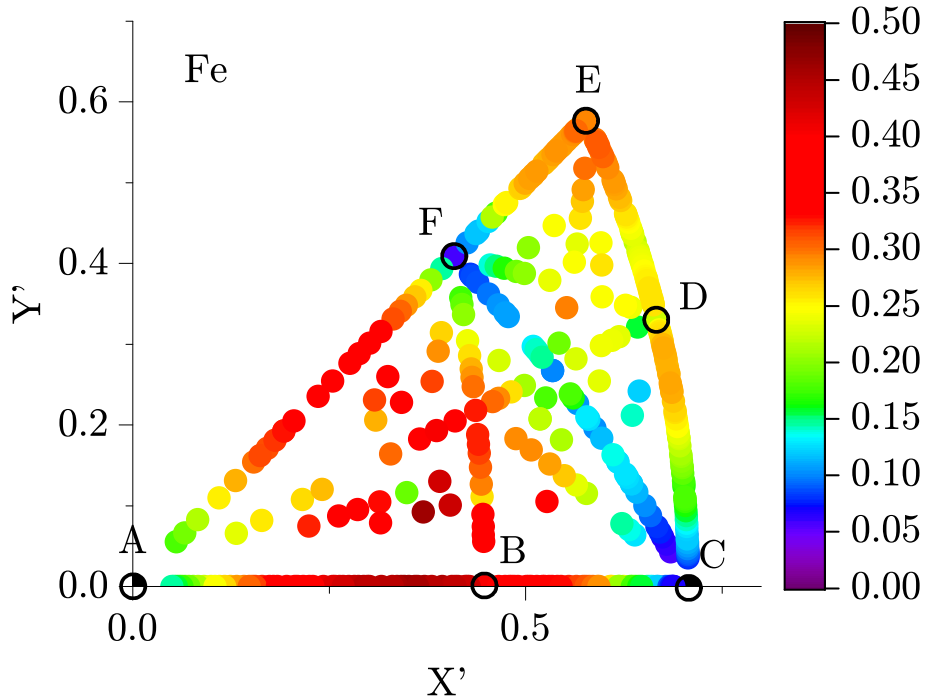
Figure 4.6: Stereographic projection showing the variation of excess volume with grain boundary orientation for Fe. X′ and Y′ are coordinates in this projection which represent a mapping from the Miller index definition $(hkl)[mno]$ (see Sec. 2.1.4). High symmetry orientations are labelled on the figure as follows: A($(100)[001]$), B($(210)[001]$), C($(101)[010]$), D($(121)[101]$), E($(323)[101]$) and F($(132)[101]$).

Paths between particular high symmetry orientations (labelled A to F in Fig. 4.5 & Fig. 4.6) define a series of GBs with fixed tilt axis $[mno]$ (known as a tilt series). For example, the [100] tilt series is defined by the path AC. The degree of rotation of the

two grains can be expressed by the tilt angle,

$$\alpha = \cos^{-1}\left(\frac{|oh - mk|}{\sqrt{(m^2 + o^2)(h^2 + k^2 + l^2)}}\right), \tag{4.4}$$

where h, k, l, m, o are the indices characterising the GB orientation $(hkl)[mno]$. The variation of excess volume with tilt angle for four high-symmetry tilt series: [100] (path AC), [101] (path CEA), [111] (path CF) and [201] (path ADFB) is shown in Fig. 4.7 & Fig. 4.8. Each tilt series exhibits a characteristic dependence on tilt angle with local minima appearing at particular GB orientations of high symmetry. For example, near 36° in the [001] tilt series ($\Sigma 5$ (310)[001]) or near 70° in the [101] tilt series ($\Sigma 3$ (111)[101]). This mirrors the cusp behaviour that is well known in the variation of GB formation energy with tilt angle [84, 85]. Importantly, while the trend in each series is similar for both Cu and Ni there is a systematic difference of up to 0.2 Å, consistent with experimental results for polycrystalline materials containing more general GBs [42, 43]. Only for a small number of low index GB orientations is the difference absent – for example $\Sigma 5$ (210)[001] in the [001] tilt series – which is attributed to its much higher symmetry which constrains atomic relaxation near the interface.
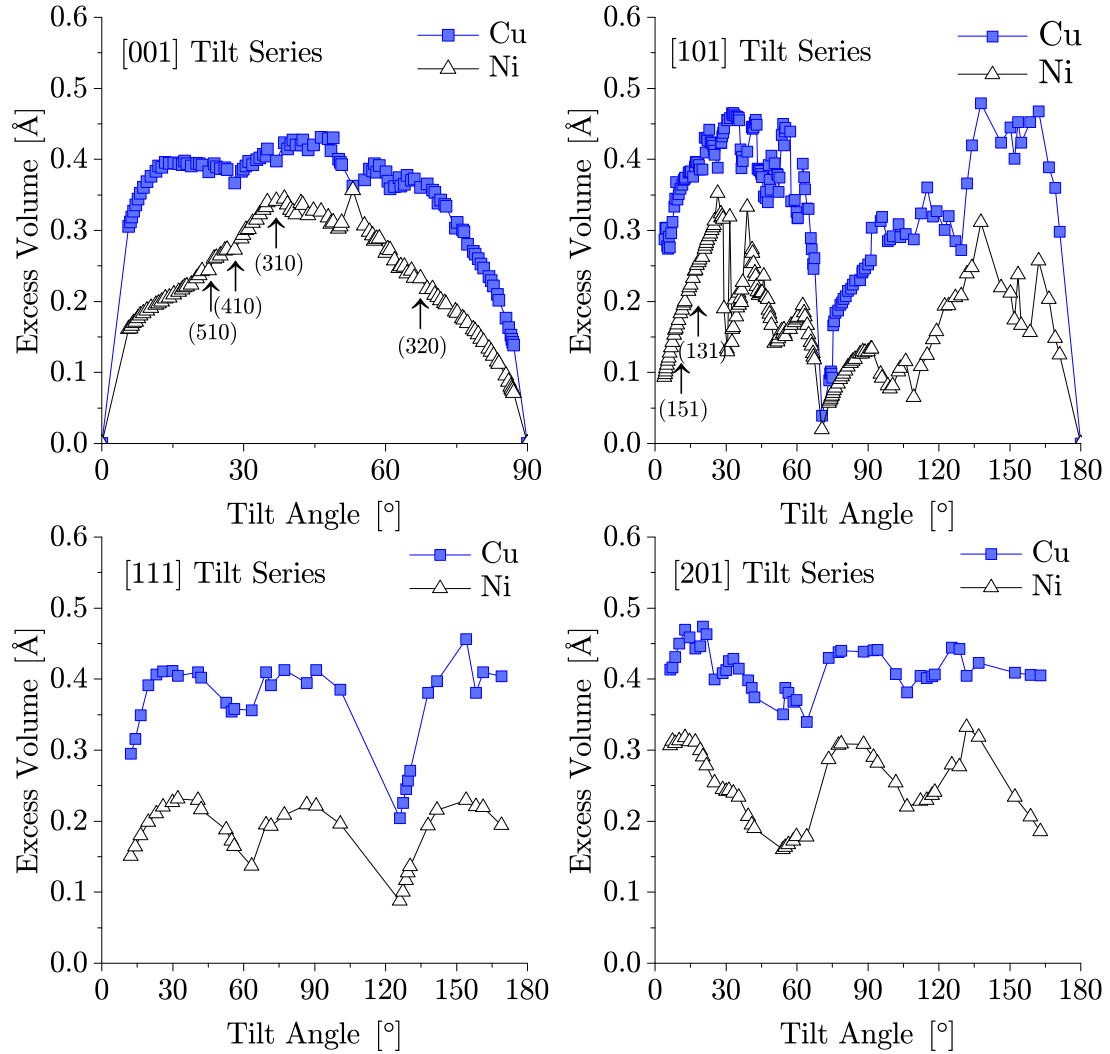
Figure 4.7: Variation of excess volume with tilt angle for the four high-symmetry tilt series: [100], [101], [111] and [201]. While the trend in each series is similar for both Cu and Ni there is a systematic difference of up to 0.2 Å.

It is found that the Fe [100] tilt series of the excess volumes are much higher when compared to Cu and Ni with the highest value being 0.45 Å (see Fig. 4.7 & Fig. 4.8). For the [101] and [201] tilt series Fe is more comparable to Ni. For the [111] tilt series Fe is much lower in excess volume than both Cu and Ni. The reason for differences between Fe and Ni is that the nearest neighbour distances are comparable ($Fe_{NN} = 2.482$ Å and $Ni_{NN} = 2.489$ Å). The similarity between the nearest neighbour distances in Fe and

Ni partly explains why the excess volumes of Fe and Ni are comparable. The major difference between the two metals is the location of the GB cusps. For example in Fe there is a low cusp in the [101] tilt series at (111)[101] 107° however in Ni this occurs at (121)[101] 70°.
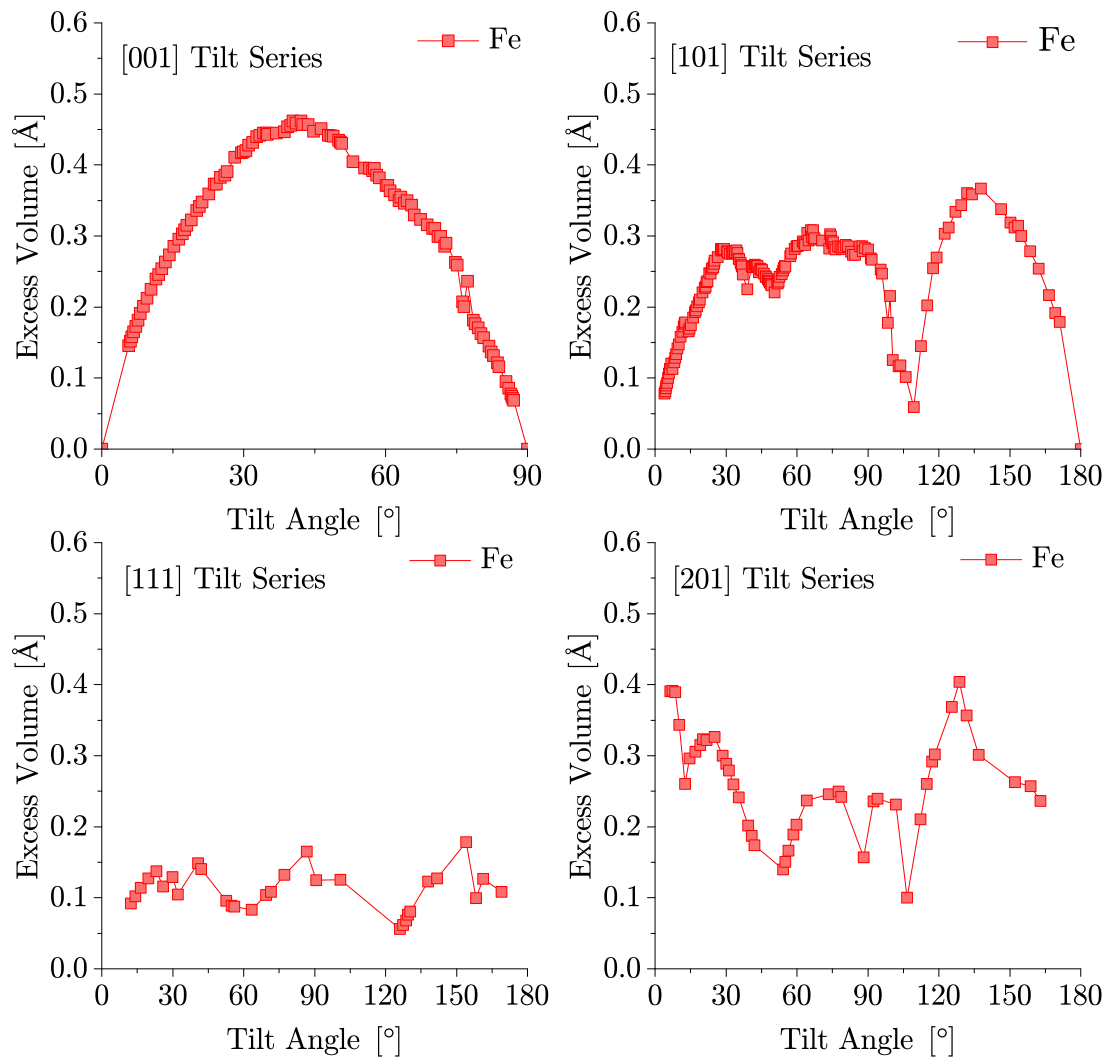
Figure 4.8: Variation of excess volume with tilt angle for the four high-symmetry tilt series: [100], [101], [111] and [201] for Fe.

4.2.4   Origin of excess volume differences in Cu and Ni

The results presented in Sec. 4.2.3 clearly demonstrates that there is a systematic differ-
ence between the excess volumes of Cu and Ni tilt GBs, larger than would be expected
based on their rather similar lattice constants (differing by less than 3%). However, the
above analysis above does not allow us to assess whether this difference is associated
with the local atomic structure at the interface or with the longer range strain field
associated with GBs. Providing insight into this question requires a detailed analysis
of the atomic structure of GBs in both materials. For this purpose a number of GBs
from the [001] and [101] tilt series are selected for more detailed analysis. In particular,
the $\Sigma 5$ (310)[001], $\Sigma 17$ (410)[001], $\Sigma 13$ (510)[001], $\Sigma 13$ (320)[001], $\Sigma 11$ (131)[101] and
$\Sigma 27$ (151)[101] GBs as indicated by the arrows in Fig. 4.7. Fig. 4.9 shows the local
atomic structures of each of these GBs for both Cu and Ni. In each case the structural
units which define the interface structure extend to the second atomic layer from the
plane of mirror symmetry. The perpendicular distance from the mirror plane to the
second atomic layer, $d^2_{Cu/Ni}$, is calculated to quantify the half-width of the structural
unit (shown for each GB in Fig. 4.9).
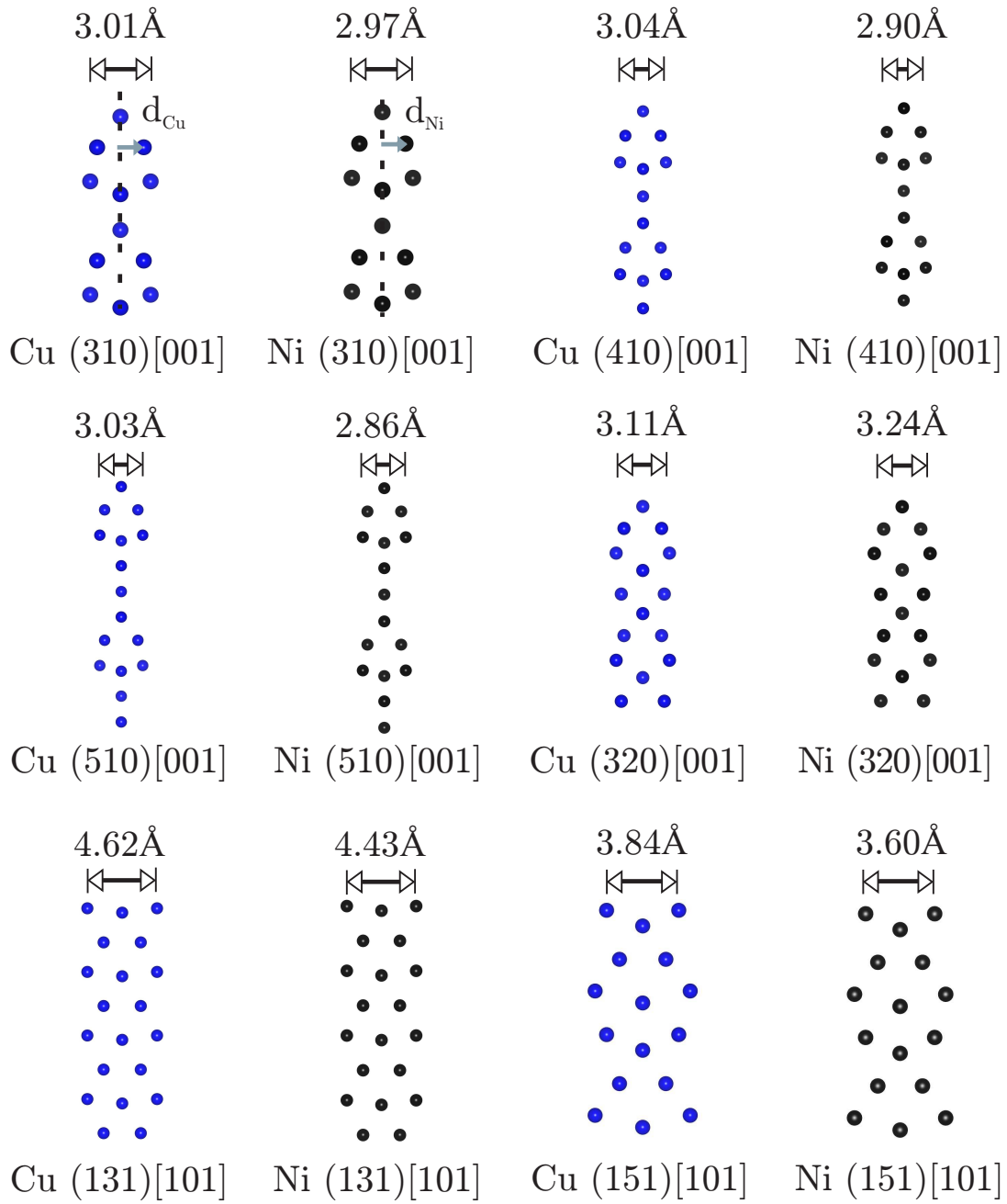
Figure 4.9: Atomic structure of selected grain boundaries in the [100] and [101] tilt series. The half-width of each structural unit (defined as the perpendicular distance from the mirror plane to the second atomic layer) is shown for each grain boundary in Cu and Ni.

The half-widths of the structural units in (310)[001], (410)[001], (510)[001], (131)[101]

and (151)[101] GBs are all larger in Cu than Ni (0.020 Å, 0.070 Å, 0.072 Å, 0.095 Å and 0.12 Å respectively) which is consistent with the observed excess volume differences. These differences are sufficient to account for a significant proportion of the total difference in excess volume observed. However, it is found that in (320)[001] the difference is -0.065 Å, meaning that the long range strain field plays a larger role in the determination of the total excess volume. The differences in structural units for an additional six GBs have been analysed. The half-widths of the structural units in the (610)[001], (710)[001], (810)[001], (910)[001] and (341)[111] GBs show that the dislocation structures accounts for a significant proportion of the difference in excess volume (in Fig. 4.10). It is found that in (430)[001] the half width of the structural unit is larger in Ni than Cu. However, as found for the GB analysis presented in this chapter in all cases differences in longer range strain associated with GBs are needed to explain the differences in excess volume.
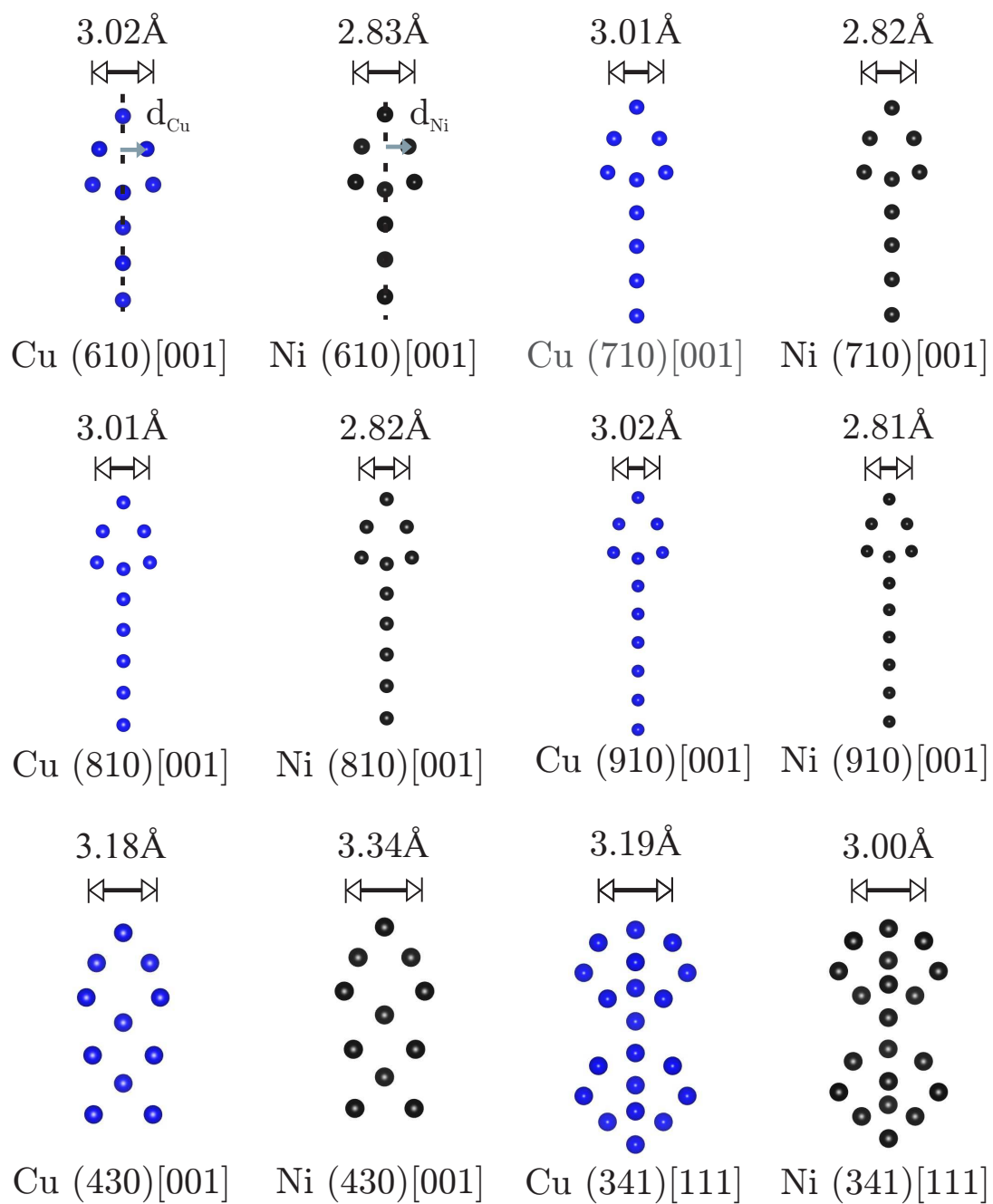
Figure 4.10: Atomic structure of selected grain boundaries in the [100], [101] and [111] tilt series. The half-width of each structural unit (defined as the perpendicular distance from the mirror plane to the second atomic layer) is shown for each grain boundary in Cu and Ni.

A direct comparison of the widths of structural units in Cu and Ni GBs is only possible in cases where the most stable GB structure in each material is equivalent. Of the twelve GBs analysed the half-width of the structural unit is larger in Cu than Ni for ten GBs. However, in all cases longer range strain (i.e. beyond the second atomic layer away from the GB plane) is needed to explain differences in excess volume between Cu and Ni.

To analyse the longer range differences in atomic structure between Cu and Ni GBs of the same orientation the following dimensionless quantity can be defined,

$$\Delta^i = \left(\frac{d^i_{\mathrm{Cu}}}{a_{\mathrm{Cu}}} - \frac{d^i_{\mathrm{Ni}}}{a_{\mathrm{Ni}}} \right), \tag{4.5}$$

where $d^i_{\mathrm{Cu/Ni}}$ is the perpendicular distance from the mirror plane to a particular atomic layer i in the supercell (similar to the definition above but for a general atomic layer), and a_{Cu} and a_{Ni} are the lattice constants of Cu and Ni. Far from the GB atomic planes are equally spaced and do not contribute to the excess volume, i.e. $d_{\mathrm{Cu}} \to \delta V_{\mathrm{Cu}} + k a_{\mathrm{Cu}}$ and $d_{\mathrm{Ni}} \to \delta V_{\mathrm{Ni}} + k a_{\mathrm{Ni}}$, where $\delta V_{\mathrm{Cu/Ni}}$ is the excess volume and k is a constant[3]. Far from the GB Δ converges to a constant ($\Delta = \delta V_{\mathrm{Cu}}/a_{\mathrm{Cu}} - \delta V_{\mathrm{Ni}}/a_{\mathrm{Ni}}$). Therefore the variation of Δ provides a convenient way to quantify the spatial extent of the region around the GB that contributes to the excess volume difference.

In Fig. 4.11 the dependence of Δ is shown for each of the GBs identified above. It is noted that in each case the second point corresponds to the distance to the second plane shown in Fig. 4.9. Considering the (310)[001] GB one finds that for the second layer Δ is negative, consistent with the small difference in the structural unit half-width noted above. However, Δ exhibits oscillations from layer to layer converging to a positive value by the eleventh atomic plane (corresponding to a distance of about 6 Å). Similar oscillations are seen in the other GBs considered with convergence to a positive Δ typically being achieved within around 5 to 15 Å of the GB plane. However, in cases with a longer range of convergence the variation of Δ exhibits small amplitude oscillations characteristic of a strain field and the majority of the excess volume is already established within a smaller range of about 5 Å.

---

[3]This constant is the same in both Ni and Cu and represents the number of bulk-like atomic planes.
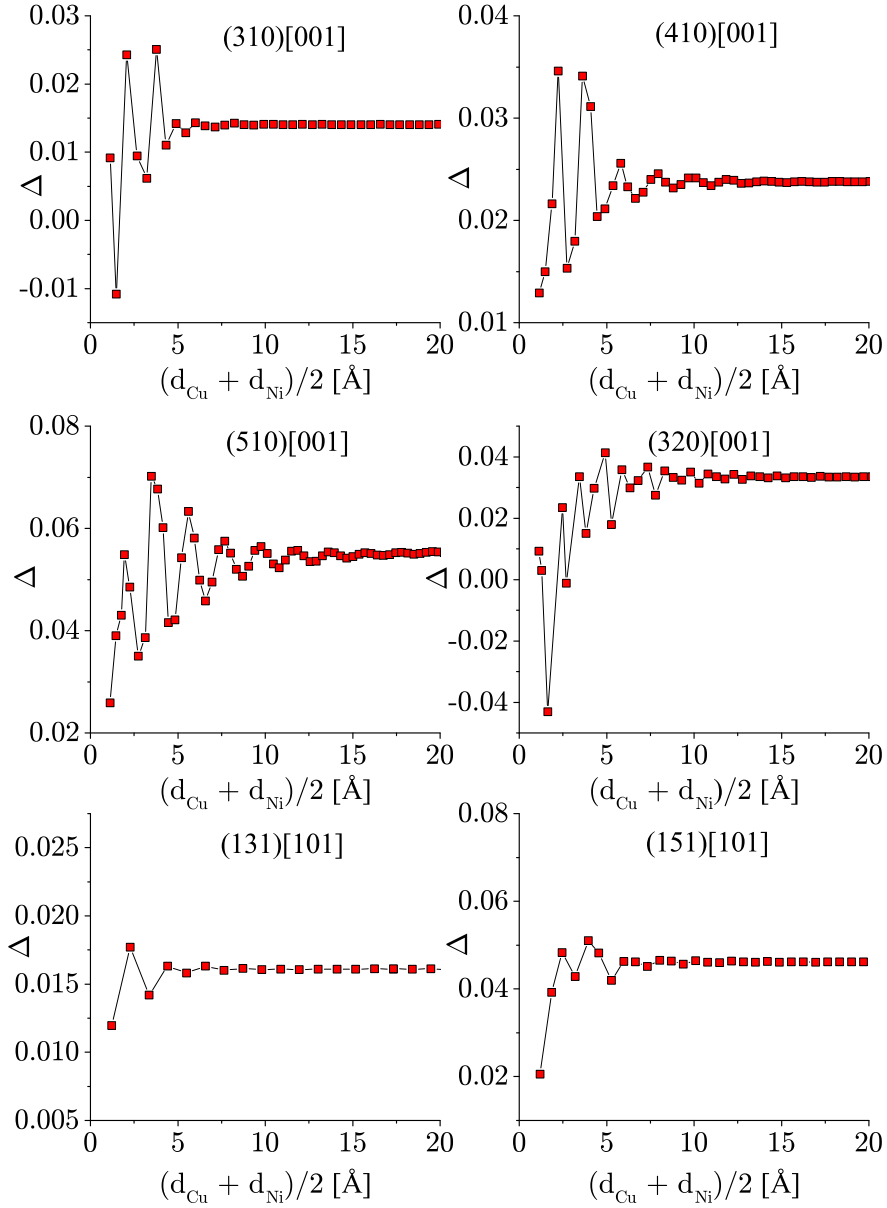
Figure 4.11: Variation of the dimensionless parameter Δ (Eq. 4.5) with distance from the GB mirror plane for grain boundaries from the [100] and [101] tilt series. The convergence of Δ to a positive value within 5 to 15 Å of the mirror plane defines the region associated with the excess volume.

The above analysis indicates that the differences in GB excess volume between Cu and Ni are associated with differences in the local atomic structure near the GB, mainly

within a range of ± 5 Å of the GB plane but with smaller strain contributions extending up to 15 Å in some cases. This difference cannot be explained by the difference in the lattice constants of Cu and Ni and ultimately must be due to differences in the interatomic interactions.

4.2.5 Analysis of bond strain

Further analysis of the atomic structures obtained in this study indicates that in the regions near GBs bonds can be strained significantly compared to the bulk. In extreme cases bonds can be compressed by up to 10% and extended by up to 15%. However, the majority of bonds lie in a range of $\pm 2\%$ strain. To understand how bond strains differ in Cu and Ni GBs all of the first nearest neighbour distances within 10 Å of the interface have been calculated for the (310)[001], (410)[001], (510)[001], (320)[001], (131)[101] and (151)[101] GBs. Due to symmetry only one side of the grain is considered. The strain σ for each bond is calculated using the following formulae,

$$\sigma_{Cu} = \frac{l_{Cu} - \frac{\sqrt{2}}{2} a_{Cu}}{\frac{\sqrt{2}}{2} a_{Cu}}, \tag{4.6}$$

$$\sigma_{Ni} = \frac{l_{Ni} - \frac{\sqrt{2}}{2} a_{Ni}}{\frac{\sqrt{2}}{2} a_{Ni}}, \tag{4.7}$$

where l_{Cu} and l_{Ni} are the lengths of each bond in Cu and Ni respectively, σ_{Cu} and σ_{Ni} are the strains in Cu and Ni respectively and the factor of $\frac{\sqrt{2}}{2} a_{Cu,Ni}$ arises from calculating the nearest neighbour distance in an fcc metal from the lattice constant. The difference of the strains η is defined below,

$$\eta = \sigma_{Cu} - \sigma_{Ni}. \tag{4.8}$$

This difference is calculated for each bond and plotted in a histogram with a bin width of 0.25% for the whole population of bonds within 10 Å of the interface and a reduced sample in which only strains greater than 1% are allowed $|\sigma| > 1\%$. For values greater than zero η characterises a bond which is strained more in Cu than in Ni, for values less than zero η describes a bond which is strained more in Ni than Cu. The reduced range is taken to reduce the skew of the distribution towards zero since for bulk like bonds there is no preferential straining. The histograms show that there are far more bonds with

$\eta > 0$, which suggests that on average Cu is strained more than Ni. The histograms are shown in Fig. 4.12 & Fig. 4.13. This is consistent with the fact that the bulk modulus of Cu is considerably smaller than that of Ni (138 GPa compared to 186 GPa respectively) a property well represented by the EAM potentials used. Therefore the difference in bulk moduli provides a semi-quantitative interpretation for the observed difference in excess volume between Cu and Ni.
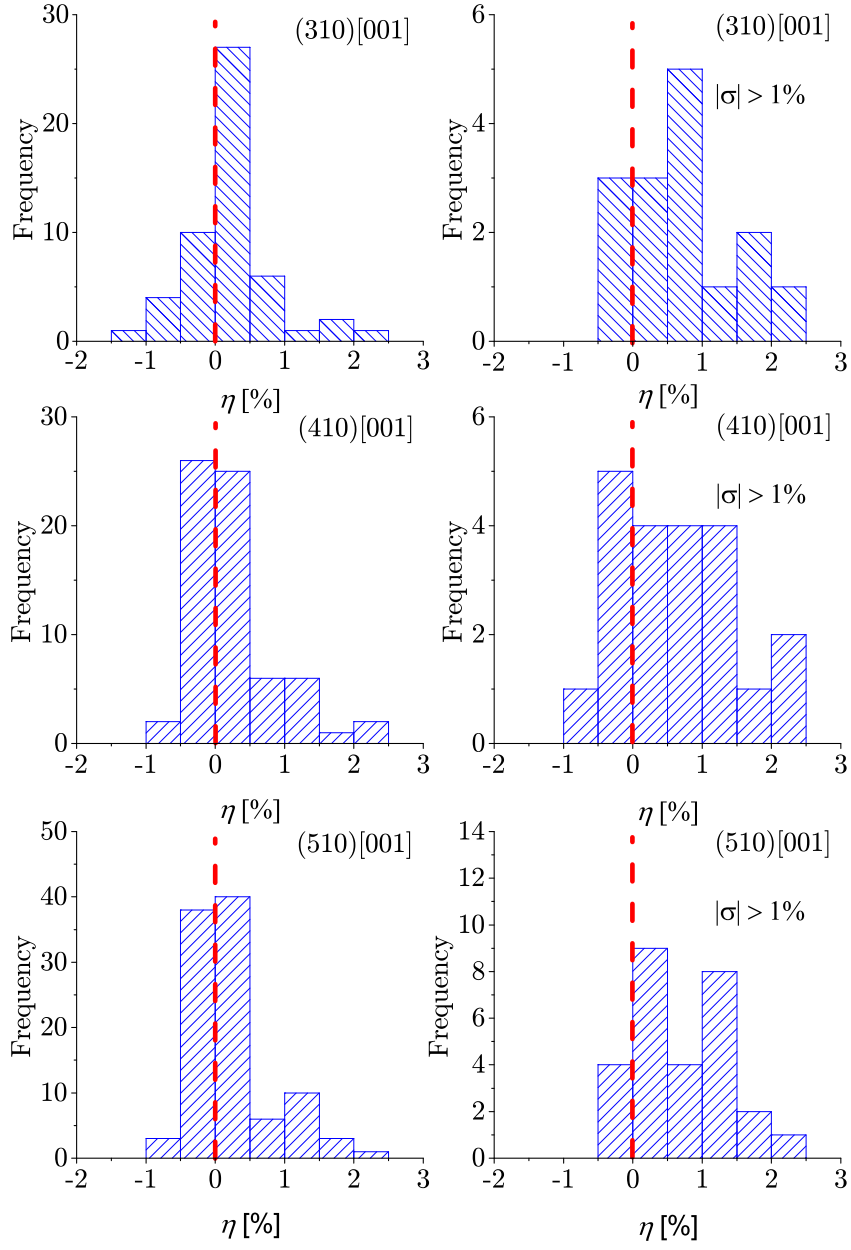
Figure 4.12: Histograms of the strain difference η (Eqn. 9) plotted with a bin width of 0.25%. The red dashed line indicates the parity value of the two strains ($\eta = 0$). There is a preference towards additional strain in Cu over Ni in all grain boundaries.
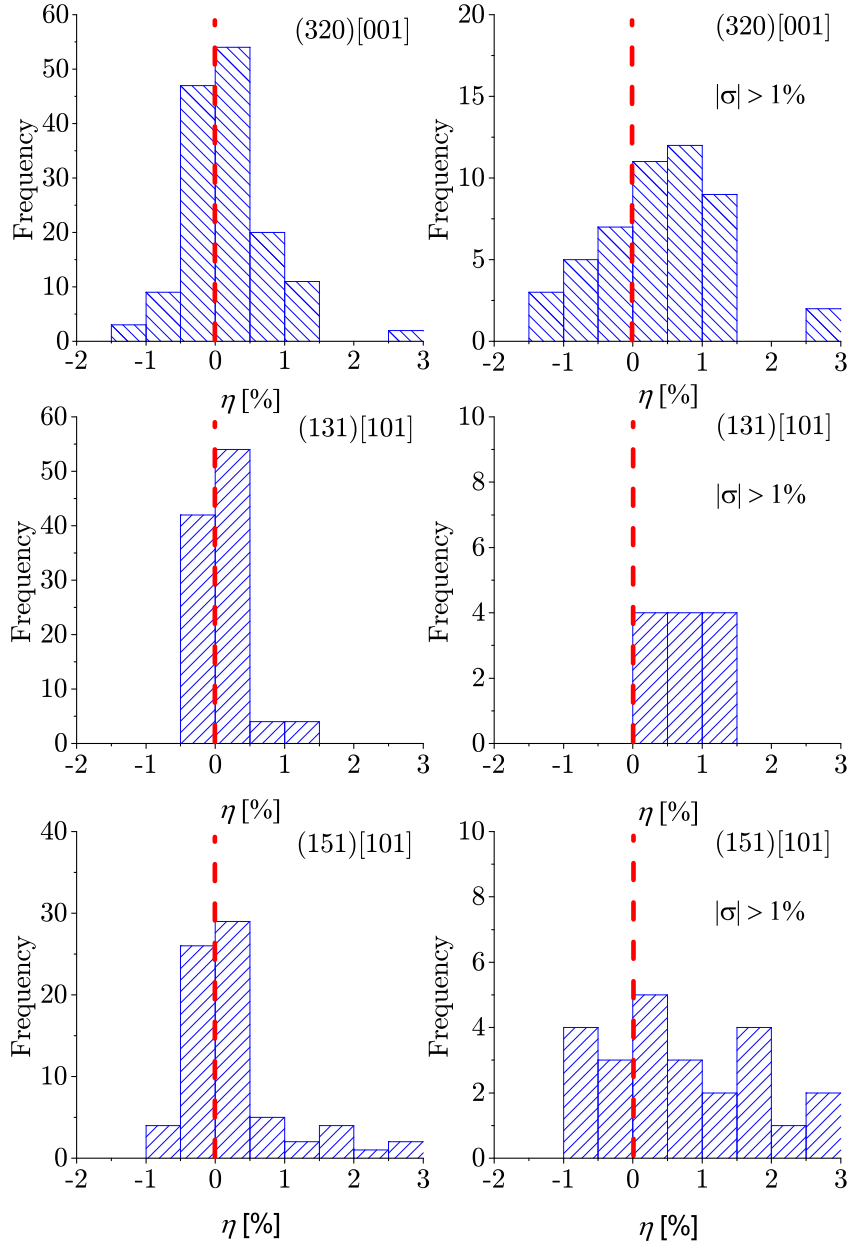
Figure 4.13: Histograms of the strain difference η (Eqn. 9) plotted with a bin width of 0.25%. The red dashed line indicates the parity value of the two strains ($\eta = 0$). There is a preference towards additional strain in Cu over Ni in all grain boundaries.

4.2.6 Statistical distribution of excess volume

Our set of 400 distinct GB structures samples a wide range of possible orientations as shown in Fig. 4.4. To generate statistical distributions of excess volume relevant to real polycrystalline materials all inequivalent orientations should be sampled, however this is computationally infeasible as other supercells contain too many atoms. Since the variation in GB formation energy and excess volume is relatively smooth between calculated points a linear interpolation approach is proposed to generate a uniform sampling of GB formation energy and excess volume across the orientations.

Physically the interpolation is a reasonable approximation because most of the GB cusps which are present have been modelled. Discontinuities are usually where an interpolation scheme is likely to fail. Regions slightly away from the cusps can be described by a Read and Shockley formula [78] which is approximately linear.

It can be shown that the variation of GB formation energy and excess volume with orientation are converged by considering a random sample of only 350 GBs in the total data set. The idea here is to pseudo-randomly choose a sample of the excess volumes to compute a fractional distribution with. Then the total number of random points is increased as described above. If the data was random the resulting distributions should be drastically different. For many different runs it should be expected that there should be a significant amount of variance between the distributions for a differing number of points chosen in the dataset. But after running the process 100s of times there is little difference between a distribution with 350 points and one with the whole dataset[4] (see Fig. 4.14).

---

[4]Note here only one random sample is chosen for the purposes of conciseness.
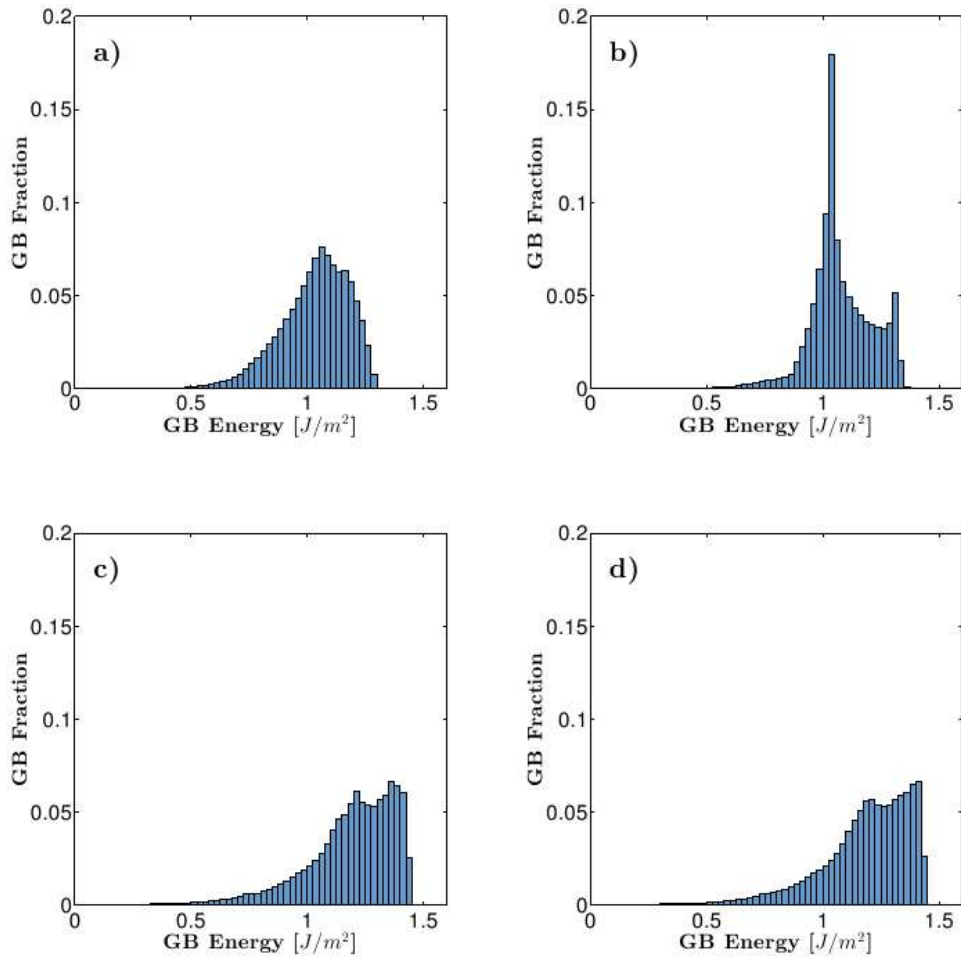
Figure 4.14: Fractional distributions of grain boundary energy in nickel based on a sample of the symmetric tilt grain boundaries. (a) with 10 points, (b) with 20 points, (c) with 350 points, (d) with 400 points.

Further to generating distributions it is possible to show how the percentiles in the distribution change with the addition of points (see Fig. 4.15). It is observed that with a mere 40 points the 1st percentile and 0.1^{th} percentile are largely converged. The trend of convergence is similar if the process were to be re-run with a different sample of points. This gives confidence that the interpolation scheme is valid.
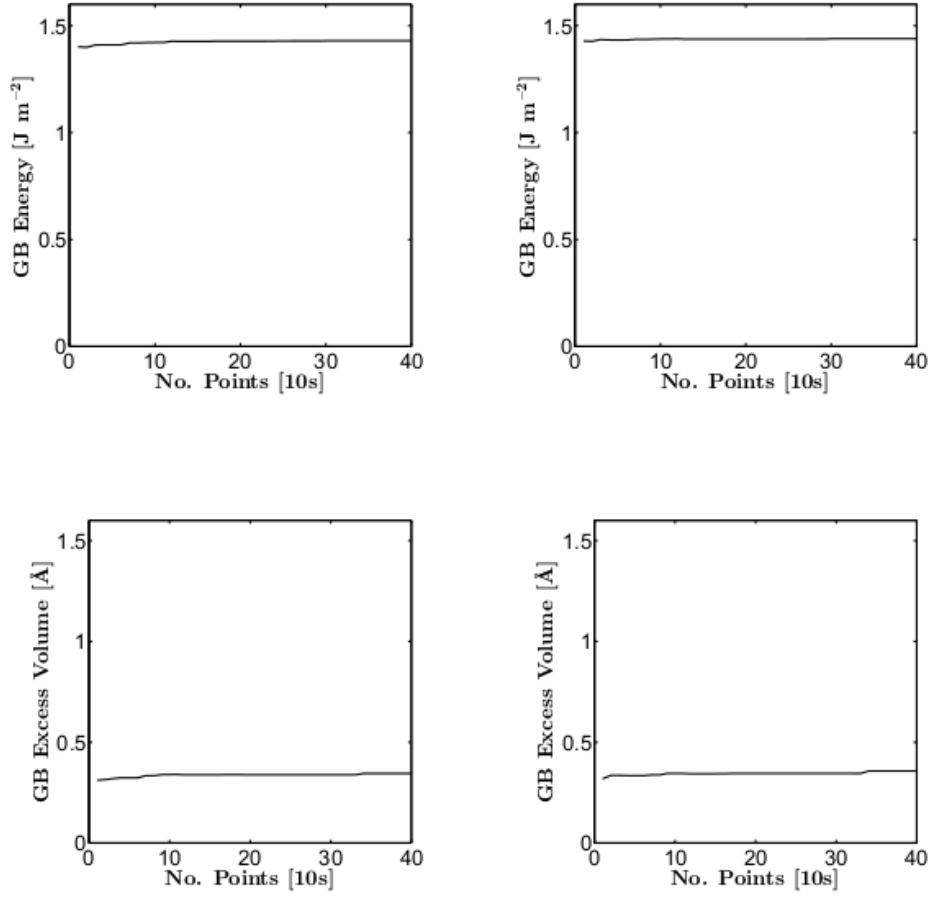
Figure 4.15: Convergence of percentiles in Ni, (a) grain boundary energy 1 Percentile, (b) grain boundary energy 0.1 Percentile, (c) Excess volume 1 Percentile, (d) Excess volume 0.1 Percentile.

Fig. 4.16 shows the interpolated LP for GB formation energy and excess volume for Fe, Cu and Ni. For both fcc metals the GB formation energy LP is characterised by zero energies at the bottom corners of the plot which correspond to (100)[001] and (101)[010] STGBs. These occur because STGBs with these surfaces make a bulk crystal. Low energy structures at the points [111] and [131] are observed, which correspond to the coherent twin GBs. For the excess volume copper and nickel exhibit similar features at the cusps but there is a low excess volume pathway from [131] to [101] in nickel which does not exist in copper. In the case of bcc iron the GB formation energy minima are located at [100] and [101] as in copper and nickel, but only one more deep minima at

82
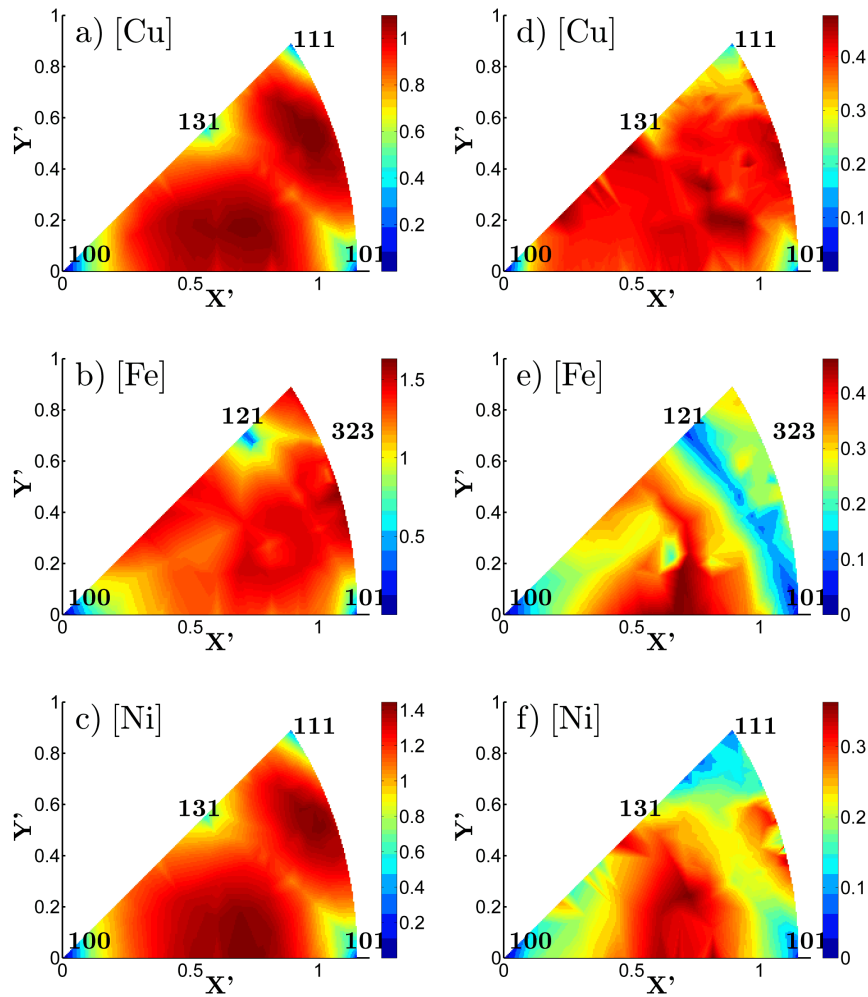
Figure 4.16: Lambert azimuthal equal area projections showing the variation of grain boundary formation energy and excess volume with grain boundary orientation obtained using the interpolation scheme. Important orientations are noted in each figure. Grain boundary formation energy and excess volume for Fe, Cu and Ni are shown in (a-c) and (d-f) respectively.

[121] is found with a shallow minima at [323]. With the excess volume it is noticed that there is region of low excess volume from [121] moving down towards [101], there are also some spots towards the centre of the projection representing discontinuities of the excess volume. These discontinues originate from the non-continuous nature of stable GB structures as the orientation of the crystals changes.

The normalised histograms for the full dataset of 400 points are shown in Fig. 4.17.
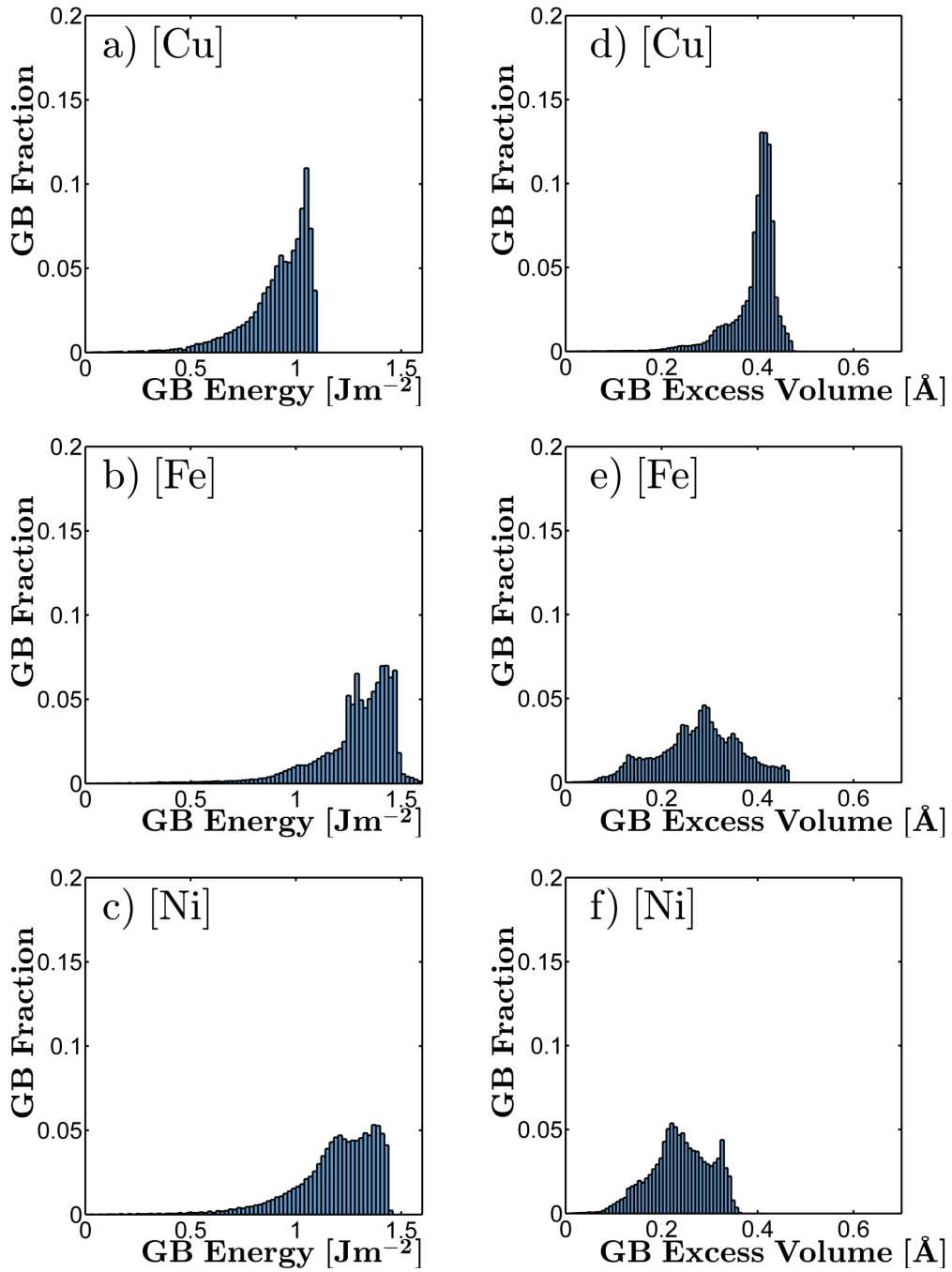
Figure 4.17: Distributions of grain boundary formation energy for all 400 points in the dataset assuming all orientations are equally likely. Grain boundary formation energy and excess volume for Fe, Cu and Ni are shown in (a-c) and (d-f) respectively.

For Fe, Cu and Ni a similar distribution for the population of GB formation energy is observed, this is characterised by low populations at low energies and large populations at high energies. This shows that given a random orientation it is more likely to get a higher energy GB. There is also a distinct difference between the maximum formation energy of copper in comparison to the other metals. In contrast each material has an excess volume distribution which varies significantly. For copper the distribution is asymmetric with a large peak which dominates, for iron the distribution resembles a normal distribution with minor perturbations and for nickel the distribution is similar to iron but is narrower and shifted towards lower excess volume. The distinct differences between the distributions of excess volume and that of formation energy suggests, that the differing material properties of Fe, Cu and Ni play a key role in the stable geometrical configurations.

The distributions shown in Fig. 4.17 represent a system in which all GB orientations are equally likely, however in general lower energy GBs are thermodynamically more stable hence more boundaries will be clustered in the low energy regions of the LP. The history of the sample will also play an important role in determining types of GBs present. There have been many examples of previous works which have experimentally measured and modelled the population of certain GBs with the GB formation energy [117, 118, 238–241]. The choice of modelling the relationship between population and formation energy follows from previous experimental work which has found a negative correlation between the relative GB formation energy and σ_i (the population) [118, 239–241]. In the model a weighting factor σ is introduced to bias the distributions towards GBs with lower formation energies. The f' are modified in the following way,

$$f_i' = \frac{\sigma_i f_i}{\sum_i^n \sigma_i f_i}, \tag{4.9}$$

$$\sigma_i = e^{(\beta \gamma_i)}. \tag{4.10}$$

where the form of σ_i has been postulated to model a situation where low energy GBs and their excess volumes are more probable than those with a higher energy. A simple exponential function has been used for model where γ_i is the formation energy and $\beta = -2$. The choice of β is arbitrary but describes the rate at which GBs become less likely. In the fullness of time β may be predicable experimentally.
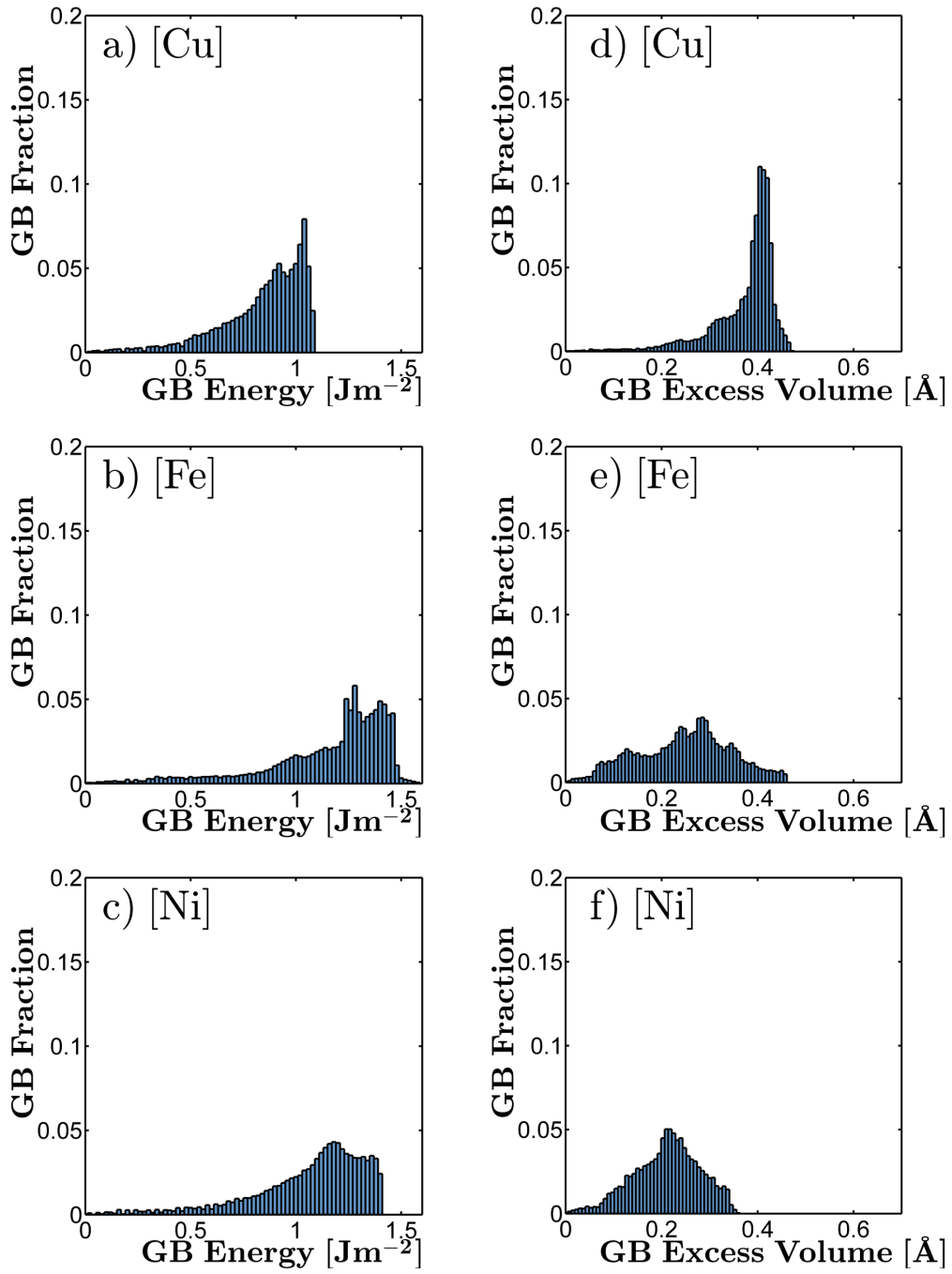
Figure 4.18: Distributions of grain boundary formation energy reweighted according to grain boundary formation energy. Grain boundary formation energy and excess volume for Fe, Cu and Ni are shown in (a-c) and (d-f) respectively.

Fig. 4.18 shows the re-weighted distributions for Fe, Cu and Ni. In comparison to the unweighted distributions there is a general shift to lower GB energies as expected. When this new adjustment factor is applied to copper the main peaks of formation energy and excess volume become diminished and the lower energy and excess volume regions of the histogram are increased. In iron the secondary peak surpasses the primary peak in the distribution for GB formation energy, for excess volume there is a significant increase in the fraction of GBs with lower excess volumes. In nickel the main peak in the GB formation energy distribution shifts to the left and high energy peaks are smeared out, while in the excess volume distribution the high volume plateau smears out. In Table. 4.3 summary statistics for the GB formation energy and excess volume for the unweighted and the weighted data in each material is shown.

For copper experimental excess volume have been measured as 0.46 ± 0.11 Å. The copper excess volume lies within the range of excess volumes which has been calculated theoretically $(0 - 0.48)$ Å and within one standard deviation of the average theoretical excess volume of 0.39 ± 0.07 Å [43]. The excess volume for two samples of nickel have been measured to be 0.32 ± 0.04 Å and 0.35 ± 0.04 Å. The experimentally calculated excess volumes for Ni both lie within the range of excess volumes found theoretically $(0 - 0.36)$ Å and is two standard deviations above the average excess volume of 0.21 ± 0.07 Å [42]. There is a good agreement between theoretically calculated excess volumes and experimental excess volumes.

Further comparisons may be made to experiments which have measured the fraction of GBs with particular orientations. In particular there are two studies which have calculated the fraction of occurrence of GBs in nickel. The first study by Lim and Raj (1984) [238] measured the ocurrence of CSL or Σ values in a polycrystalline sample of nickel. They found a significant peak at $\Sigma 3$ which could correspond to either $(111)[001]$ or $(121)[001]$ GBs. Computationally the $(111)[001]$ STGB corresponds to an extremely low formation GB but the $(121)[001]$ is high in comparison. In the second study by Li et. al. [117] they have calculated the fraction of occurrence over a continuous range of stereographic coordinates. It is found experimentally that there is a large number of GBs at (111) but no other significant GB types. There is good agreement between experimental and theoretical results in that the most common GB in Ni are those tilted about the (111) plane. Theoretically the lowest energy GBs are those also tilted about the (111) plane.

Table 4.3: Statistical properties of GB distributions in Fe, Cu and Ni. Subscript 1 represents the unweighted data and 2 represents the weighted data. γ (Jm^{-2}) and δV (Å) are the GB formation energy and excess volume respectively.

Cu	mean	most probable	max	standard deviation
γ_1	0.91	1.04	1.10	0.15
γ_2	0.85	1.04	1.10	0.20
δV_1	0.39	0.41	0.48	0.05
δV_2	0.37	0.41	0.48	0.07
Fe				
γ_1	1.27	1.42	1.63	0.19
γ_2	1.16	1.28	1.63	0.29
δV_1	0.27	0.29	0.46	0.09
δV_2	0.25	0.28	0.46	0.10
Ni				
γ_1	1.18	1.36	1.45	0.19
γ_2	1.07	1.18	1.45	0.26
δV_1	0.24	0.22	0.36	0.06
δV_2	0.21	0.21	0.36	0.07

4.3 Discussion

The primary factors which may affect the validity of the predictions are the accuracy and transferability of the EAM potentials and the suitability of the approach employed to determine the most stable structure for a given GB orientation. Comparisons between DFT and EAM predicted bulk and GB properties suggest EAM potentials provide a reasonable description although improvements could be made to the potentials to more accurately model highly strained bonds (-15% /$+10\%$) in GBs which may not be well described.

Furthermore to accurately predict stable structures GB supercells must also be large enough such that the two GBs in the supercell do not interact with each other. Here crystals of 30 Å thicknesses are employed, which is sufficient to minimise such effects[5]. It was ensured that the grid of points considered in the rigid body translations is sufficiently large to probe a large number of initial conditions to maximise the chances that the lowest energy structure is found (see Sec. 2.1). However, it should be noted that while it

---

[5]Note that for GB formation energies a thickness of only 20Å is required but to convergence excess volumes a larger grain size of 30Å is required.

has been demonstrated through several examples that the approach can identify stable GB structures the possibility that more stable structures may exist cannot be excluded. Here, a grid method has been used to find stable structures but other approaches, such as displacement shift complete method (DSC) as described by Sutton and Ballufi [63], are also possible.

While this study is focused on symmetric tilt GBs in principle the approach could be extended to more general types including asymmetric and mixed tilt/twist GBs. However, since the nature and origin of the effect (i.e. the presence of structural units at GBs and associated atomic relaxation and strain) is rather generic it is not expected that the qualitative conclusions should differ significantly.

When a polycrystalline sample is approximated by assuming only symmetrical tilt GBs are present all the detailed nuances of a polycrystalline material such as the other types of GBs which may exist are not considered. The effect of this may be to reduce the predictive nature of the approximation however the model can be extended to include other phenomena.

4.4   Conclusion

In this chapter a high throughput method for predicting stable GB structures from a large number of initial configurations containing many thousands of atoms has been employed. The increased computational power now available has allowed the modelling of over 400 unique tilt GB structures for Fe, Cu and Ni which span a wide range of orientations. Through analysis of these structures it has been shown that there is a systematic difference between the excess volumes of Cu and Ni GBs of up to 0.2 Å which is consistent with experiment but not fully explained by the relatively small lattice constant difference of 3%. It is found that the majority of the difference in excess volume occurs in the first 5 Å of the interface, with longer range strain effects contributing over a larger region. These differences can be understood as a result of the much smaller bulk modulus of Cu compared to Ni which means that bonds in Cu are easier to strain. Although the lattice constant for Fe is much smaller than both the fcc metals the nearest neighbour distance in Fe is very similar to that of Ni hence why the average excess volumes are similar.

These results bring much needed insight into the nature of excess volume in metals and the reasons for the different behaviour in the otherwise similar materials of Fe, Cu and Ni. These ideas may find important application in the computational design of materials, for example by identifying materials properties which may influence excess volume. In particular, it is thought that GBs with higher excess volumes are significantly more prone to defect segregation, diffusion and embrittlement which may prove catastrophic when used in extreme environments such as fusion reactors [38, 213]. If one wishes to minimise the excess volume in metals to limit impurity segregation the results presented in this chapter suggest that a material with a small nearest neighbour distance and a large bulk modulus should be selected.

Polycrystalline materials are ubiquitous both in nature and manmade devices and the presence of GBs is known to affect many material properties [39–41]. Although experimentally the average excess volume of polycrystalline samples have been measured by difference dilatometry, probing the excess volumes associated with individual GBs is more difficult [42, 43]. The results presented in this chapter provide atomic insight into the nature and origin of excess volume difference and provide an explanation for the different behaviour of Cu and Ni observed experimentally. Further study on the excess volumes of bcc, hcp and other structures and phases of metals needs to be undertaken to understand the nature of GBs in different environments.

Chapter 5

Grain boundaries in magnetic tunnel junctions

5.1 Introduction

GBs which have been investigated in Chapter 4 are extremely important in applications when a principal material is required in bulk for its unique properties and availability such as for railway lines, building frames, nuclear reactors, telephone and transmission wires, and many more. In many applications however a combination of many materials is required to produce a desirable phenomena or effect. Interfaces where one material is directly adhered (chemically or physically) to another to achieve a desired effect or property are intrinsic to many industries including the semi-conductor industry. A specific example is electrically insulating thin metal oxide films which form a key functional element in diverse technologies in spintronics, microelectronics, photovoltaics, optoelectronics, sensing and catalysis [242–247]. While in almost all practical devices metal oxide films are polycrystalline, very little is known about the effect of GBs on their electrical properties. The particular device of interest in this study is a MTJ which finds applications as a magnetic sensor in hard disk read heads and in emerging non-volatile MRAM technologies [46, 50, 248–250] (see Sec. 1.3 for more information). The active part of the device consists of an insulating MgO film sandwiched between two ferromagnetic FeCoB layers [17, 56, 251].

There have been many theoretical studies which have been performed in order to understand MTJs. In particular are two theoretical studies by Mathon and Bulter. The studies independently have shown that the TMR effect can be as large as 1000% in

epitaxial Fe/MgO/Fe interfaces [249, 252]. The dilemma here is that there is a large disparity between the theoretically predicted values of the TMR and the experimentally observed values. This discrepancy has fuelled much speculation including the possibility that defects such as GBs or oxygen vacancies could be diminishing the insulating properties of the MgO films. A scientific explanation of this discrepancy has been lacking.

In this chapter the properties of a MTJ are explored using theoretical techniques based on experimental measurements performed by collaborators in Japan. STEM has been used to resolve the atomic structure of GBs within an ultrathin MgO film buried inside a multilayer stack. The MgO film is polycrystalline, with a typical grain size between 10 - 15 nm with each grain oriented such that the [001] crystallographic direction is parallel to the film normal. Analysis of the STEM images reveals two commonly occurring structural unit types which correspond to an asymmetric tilt GB (which would not have been predicted in the absence of direct imaging due to its relatively high formation energy) and a more common symmetric tilt GB [253]. On the basis of these results first principles theoretical modelling of the structure and electronic properties of these systems is performed. It is found that GBs introduce additional states inside the MgO band gap. The spatial localisation of the interface states is found inside structural units at the GBs.

This chapter is structured in the following way. In Sec. 5.2.1 a description of how the MTJs were synthesised is given. In Sec. 5.2.2 the computational methods used to model the MTJs are validated. In the rest of Sec. 5.2 the results of the modelling of the MgO symmetric tilt and asymmetric tilt GBs are presented. In Sec. 5.3 the results are discussed and in Sec. 5.4 the main conclusions are presented.

5.2 Results

5.2.1 Synthesising magnetic tunnel junctions and imaging in plan-view

Experimental TEM imaging of the MgO layer within MTJs, sample growth and preparation were performed by Mitsuhiro Saito, Shunsuke Fukami, Hideo Sato, Shoji Ikeda, Hideo Ohno and Yuichi Ikuhara in Japan. They undertook a three stage process to acquire plan view images of MgO thin films. First the MTJ is grown, then all other materials are removed leaving only the MgO film[1] then TEM is employed to obtain the

---

[1]It could be that some FeCo remains on the MgO but this has not yet been experimentally verified.

plan-view images of the MgO film.

To grow the MTJ, layers are deposited onto a thermally oxidised Si substrate by radio frequency magnetron sputtering at room temperature. The stack structure from the substrate side is Ta(5)/ Ru(10)/ Ta(5)/ $Fe_{60}Co_{20}B_{20}$(5)/ MgO(20)/ $Fe_{60}Co_{20}B_{20}$(1), where numbers in parentheses are nominal thicknesses in nm. The bottom Ta/Ru/Ta/FeCoB serves as a seed to form the [001] textured structure of MgO, which is removed during the back-thinning process (see below). The top FeCoB layer deposited to protect the MgO layer is thin enough not to affect the observation of MgO structure. After the deposition, the film is annealed at 500°C for one hour.

To observe only the GBs of the MgO in the TMR device, a plan-view TEM sample which consists of only MgO needs to be prepared. TEM samples should be less than 10 nm in thickness in order to be transparent to the electron beam. Preparation of the plan-view sample can be achieved using a back-thinning method. First, the substrate of the specimen is ground with sand paper and dimpled mechanically from only the back side (substrate side) to reduce the thickness to around 20 μm. Then the specimen is thinned to around 10 nm using Ar-ion milling with an acceleration voltage of 1.5 - 3.5 kV and an incident beam angle of 4 - 6° from only the back side. Finally, the plan-view specimen which consists of only of MgO is obtained.

The GB microstructures are experimentally characterised in detail using annular bright-field (ABF) STEM. ABF imaging where an annular detector is positioned within the bright field region in an atomic resolution STEM has recently been shown to produce images with both light and heavy elements simultaneously [254, 255]. The ABF-STEM images are taken with the JEOL JEM-ARM200F (Cold FEG) electron microscope with Cs-corrector (CEOS GmbH), which is operated at 200 kV. ABF-STEM imaging was performed with a probe convergence angle of 22 mrad and a detector semiangle within 11 - 22 mrad. The obtained STEM images were low-pass filtered to reduce high frequency noise.

As shown in Fig. 5.1b the film is polycrystalline with irregularly shaped grains with typical diameters in the range 10 to 15 nm. Atomic columns in the [001] crystallographic direction are observed in every grain indicating that the film is almost perfectly [001] textured. There is a difference in contrast between the grains which suggests that small differences between the [001] growth orientation are present. Mitsuhiro Saito and Yuichi Ikuhara in Japan have also performed electron diffraction experiments (see Fig. 5.2). In

the electron diffraction pattern the experiments show rings meaning that the samples are polycrystalline (if dots were observed this would mean the samples was monocrystalline).
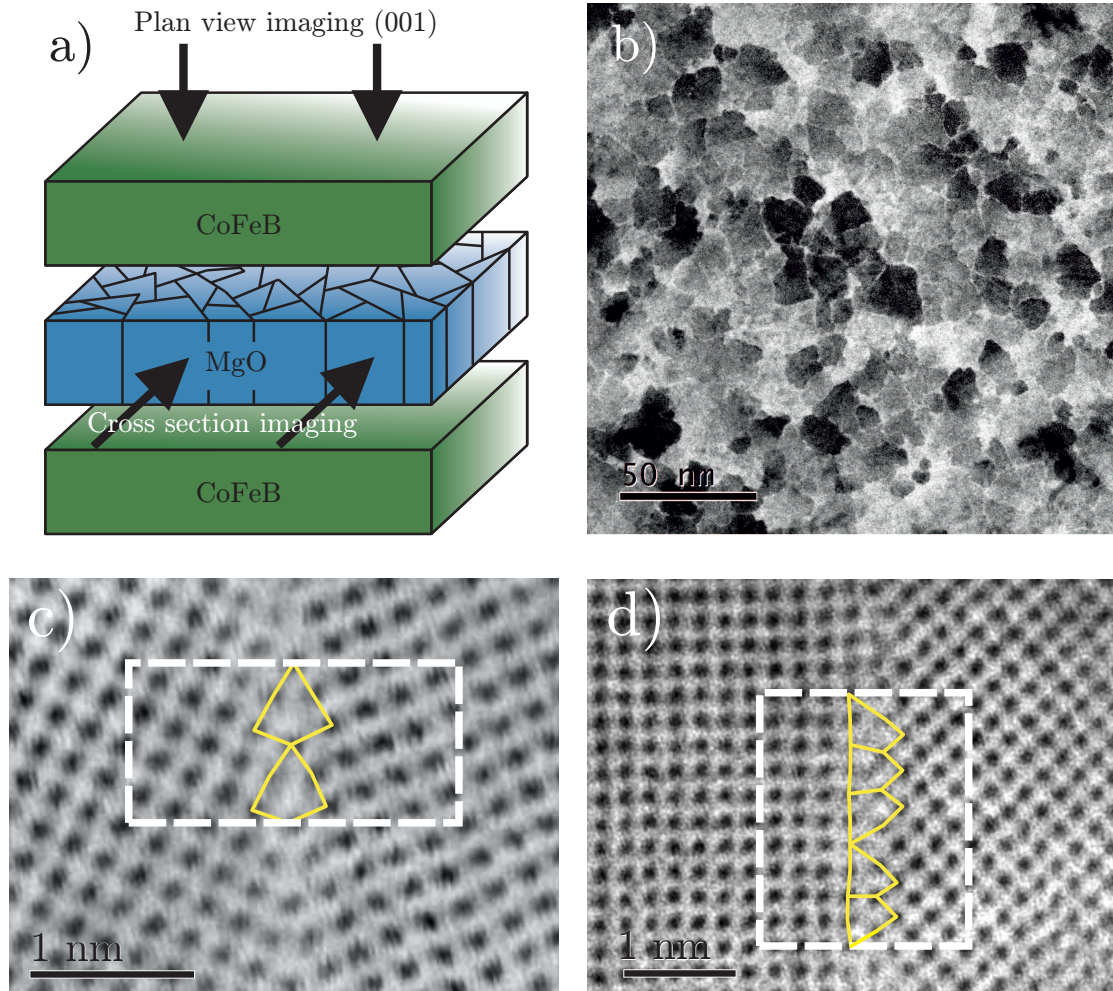
Figure 5.1: Annular bright field transmission election microscopy images of MgO polycrystalline samples a) Schematic showing the magnetic tunnel junction investigated in this study with cross-sectional and plan-view imaging directions indicated. b) Annular bright field-scanning transmission electron microscopy images showing the nanometre scale granular structure of the MgO films. c-d) Examples of commonly occurring structural units at grain boundaries corresponding to segments of a $\Sigma5(210)[001]$ symmetric tilt grain boundary (c) and a $(100)/(110)[001]$ asymmetric tilt grain boundary (d). The white dashed boxes indicate the periodic supercells which are used to model these grain boundary defects.
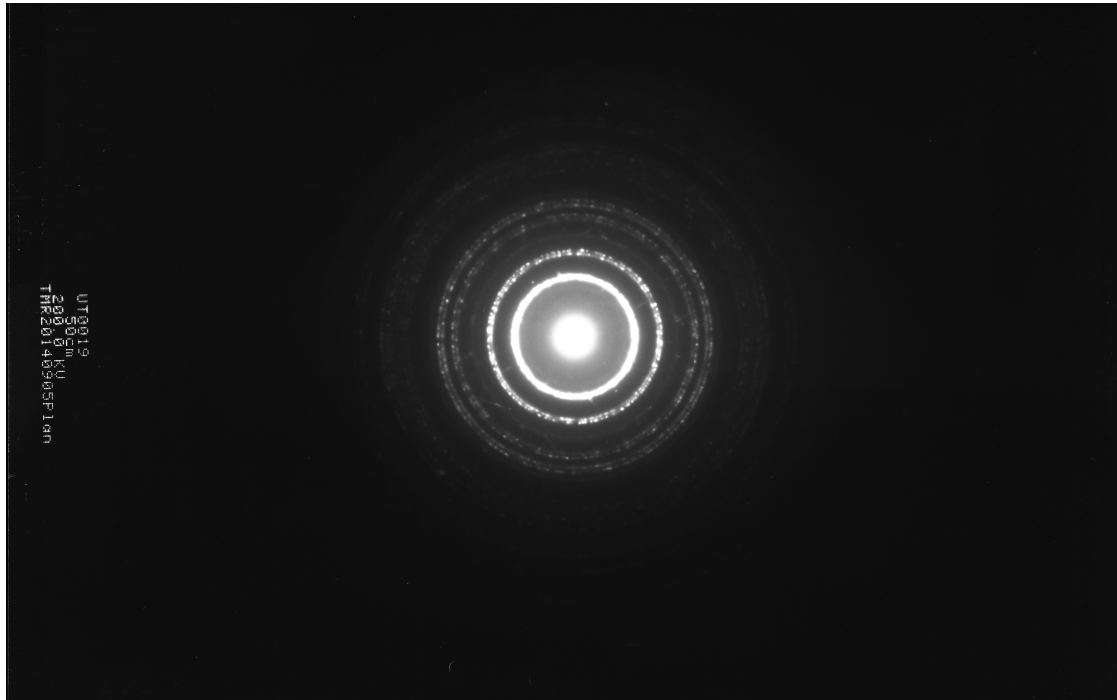
Figure 5.2: Diffraction pattern from polycrystalline films along the plan-view direction. Typical ring patterns indicate a polycrystalline sample with each ring split by several percent due to lattice mismatch between MgO and metal.

GBs in these cases consist of a connected chain of GB structural units (SUs). 35 images like that shown in Fig. 5.1b have been analysed to identify the most frequently occurring GB SUs in the MgO film. A number of commonly occurring SUs have been identified which are shown in Fig. 5.3. The most frequently occurring SU has a triangular shape with mirror symmetry along the plane of the GB. Chains of SUs of this type are analogous to segments of $\Sigma 5(210)[001]$ symmetric tilt GBs. There is also a considerable number of SUs which involve two back-to-back (or top-to-top) triangular shapes without mirror symmetry about the GB plane. Chains of SUs of this type are analogous to segments of $(100)/(110)[001]$ asymmetric tilt GBs (i.e. the grain on the left is rotated $45°$ with respect to the grain on the right). The observation of GBs of this type is quite unexpected due to the high energy associated with asymmetric tilt GBs. Some of the TEM images used in this analysis are shown in Figs. 5.4 - 5.6, with identified SUs indicated.
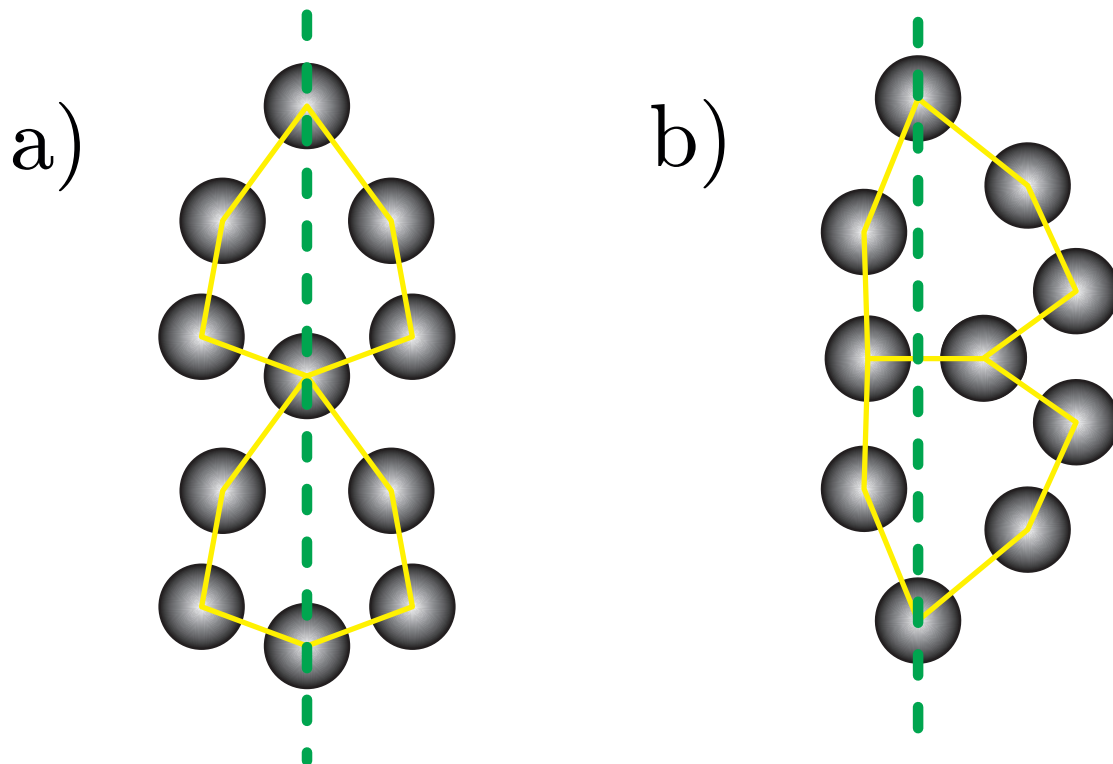
Figure 5.3: Two commonly occurring structural units in the MgO films. a) a-type structural unit which has a triangular shape with mirror symmetry along the plane of the grain boundary. b) b-type structural unit which involves two back-to-back (or top-to-top) triangular shapes without mirror symmetry about the grain boundary plane.
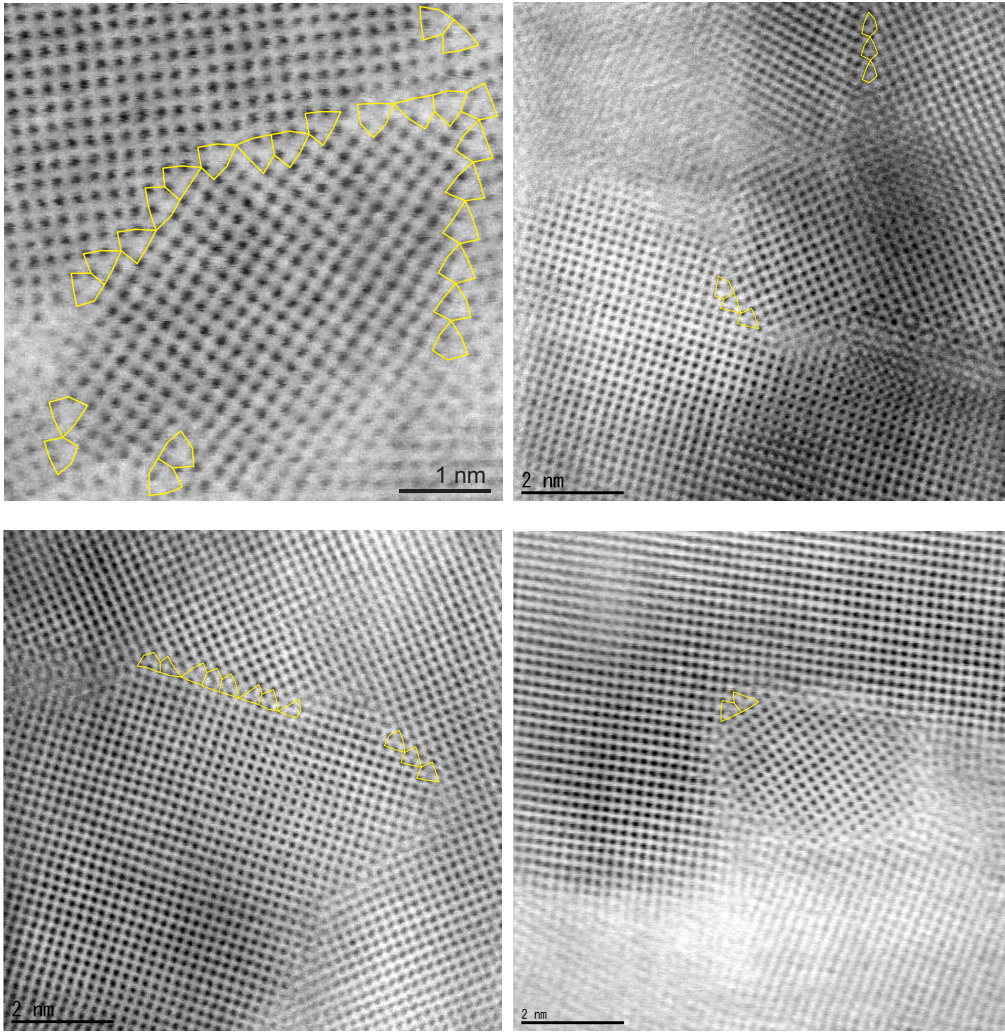
Figure 5.4: Scanning transmission electron microscopy images of the MgO film with identified structural units highlighted.
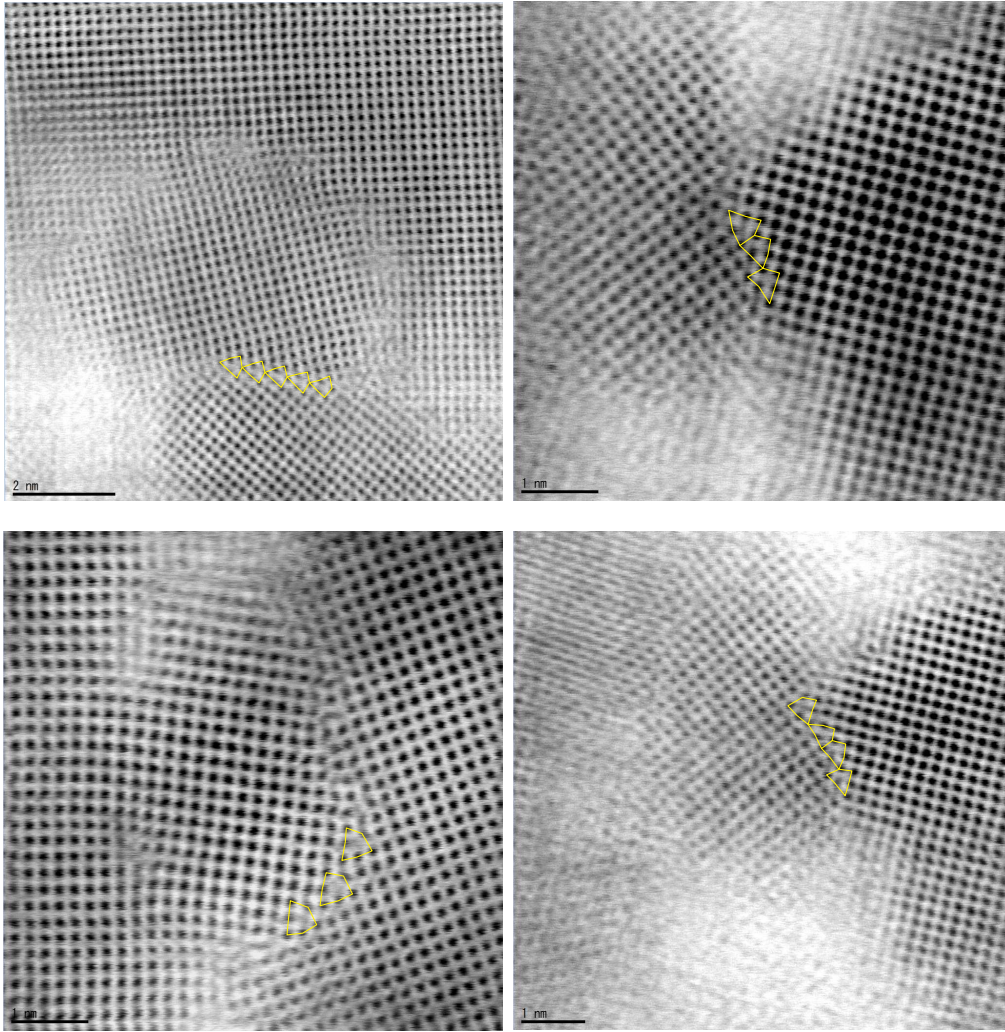
Figure 5.5: Scanning transmission electron microscopy images of the MgO film with identified structural units highlighted.
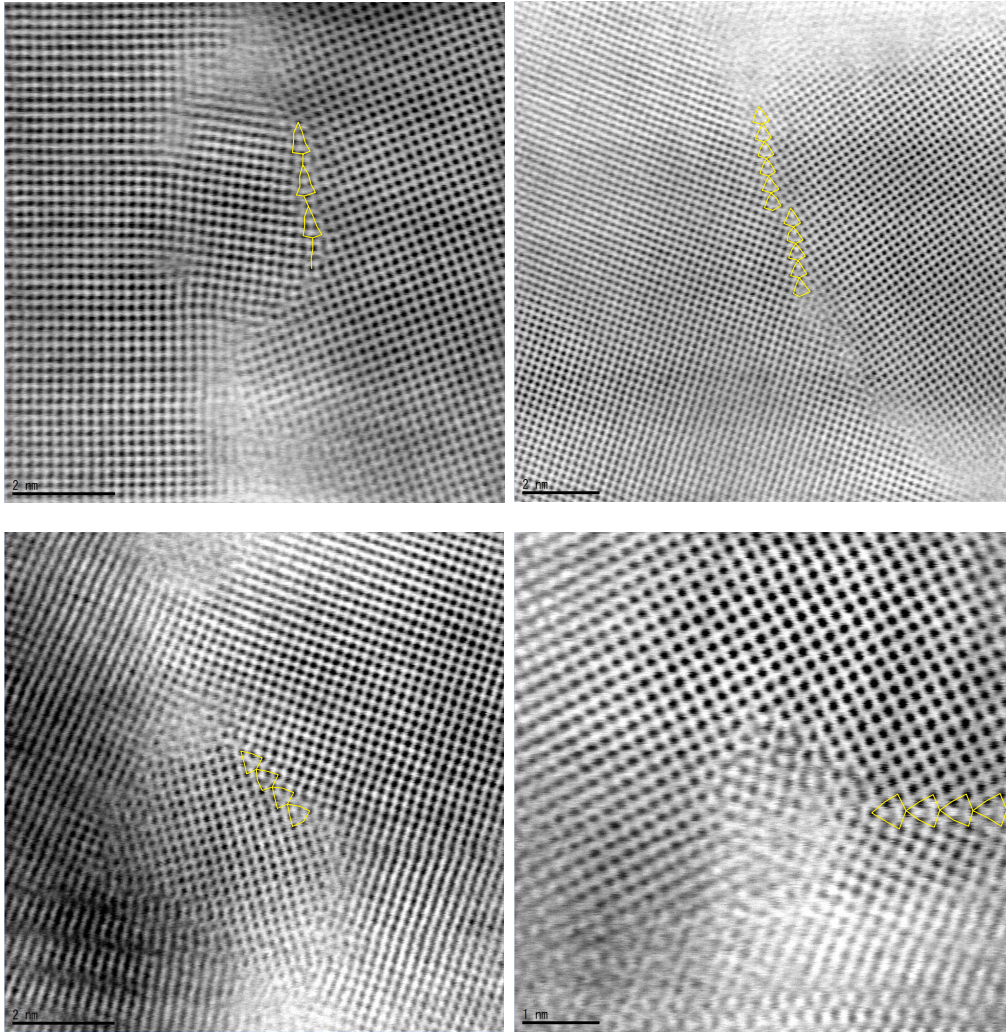
Figure 5.6: Scanning transmission electron microscopy images of the MgO film with identified structural units highlighted.

5.2.2 Computational modelling

To construct GB models based on the structural units found in TEM images knowledge gained in Chapter 4 on metal GBs can be used. In Chapter 4 it was found that in an fcc material the (210)[001] GB (Fig. 4.3) corresponds to repetitions of Christmas tree like structural units. These Christmas tree like structural units are similar geometrically to the structural units which are observed in the TEM images (see Fig. 5.3a). Thus it is the (210)[001] GB in MgO which needs to constructed to model this feature. With the

99

knowledge of the macroscopic degrees of freedom candidate structures can be generated using techniques described in the methods section (see Sec. 4.2.2). A classical Buckingham potential (see Sec. 3.1.1.1) along with a long range coulomb interaction is used to describe the interactions between the Mg and O ions and generate initial optimised candidate structures. The most stable candidate structure generated from the classical optimisation are then used as inputs for DFT calculations. The lattice cell lengths need to be rescaled between the Buckingham optimised and DFT structure to minimise forces and strain for DFT calculations.

Three-dimensionally periodic supercells are constructed to model the $\Sigma5(210)[001]$ symmetric tilt GB and the $(100)/(110)[001]$ asymmetric tilt GB. These models do not seek to replicate the complex structures shown in Fig. 5.1b but to describe the individual SUs in Figs. 5.1c & 5.1d. In the former case it is straightforward to construct such a supercell using methods previously described in the background section (Sec. 2.1.2). In the latter case the non-commensurate nature of the (100) and (110) orientations makes constructing a supercell more challenging. The $(100)/(110)[001]$ ATGB is modelled by constructing an interface between 7 unit cells of MgO(100) and 5 unit cells of MgO(110) resulting in only $\pm0.5\%$ strain in each grain.
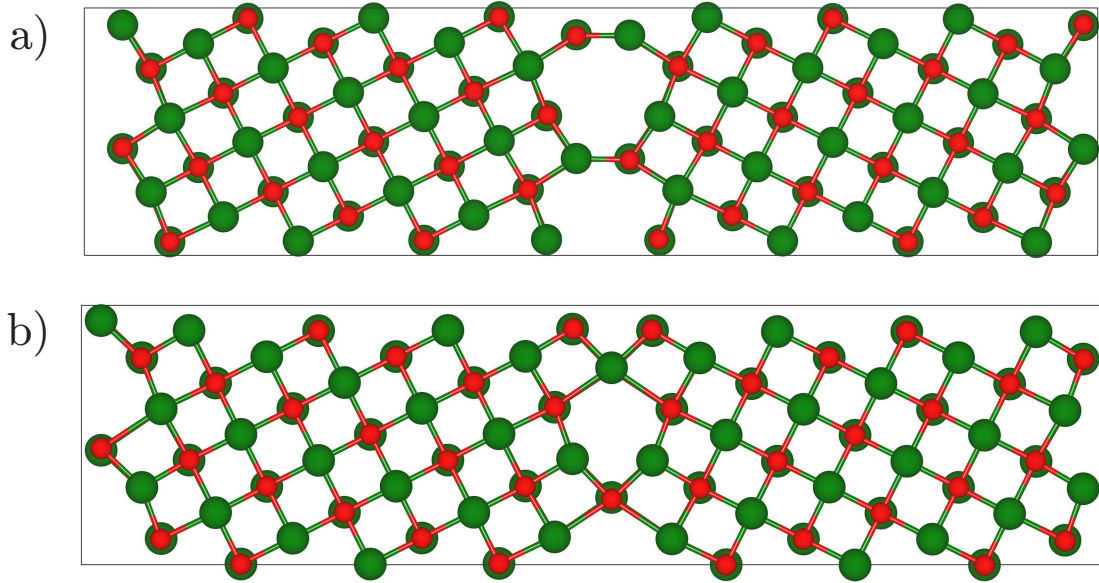
Figure 5.7: The two stable supercells found in the $\Sigma5(210)[001]$ symmetric tilt grain boundary. Red and green atoms represent O and Mg respectively.

For the $\Sigma5(210)[001]$ GB our computational search identifies two stable structures with similar energy which differ only by a rigid translation of one grain with respect to the other (shown in Fig. 5.7). Our attention is focussed on the model which matches the experimental images Figs. 5.1b - 5.1d. This is in fact a slightly less favourable structure according to DFT (by 0.4 Jm^{-2}) however the non-equilibrium nature of the growth or impurity segregation (as discussed in previous work on MgO [16,177]) could influence the GB structure which is formed in reality. The formation energy of the $\Sigma5(210)[001]$ GB is calculated to be 1.7 Jm^{-2}. The formation energy of the $(100)/(110)[001]$ asymmetric tilt GB is much higher as expected (2.2 Jm^{-2}).
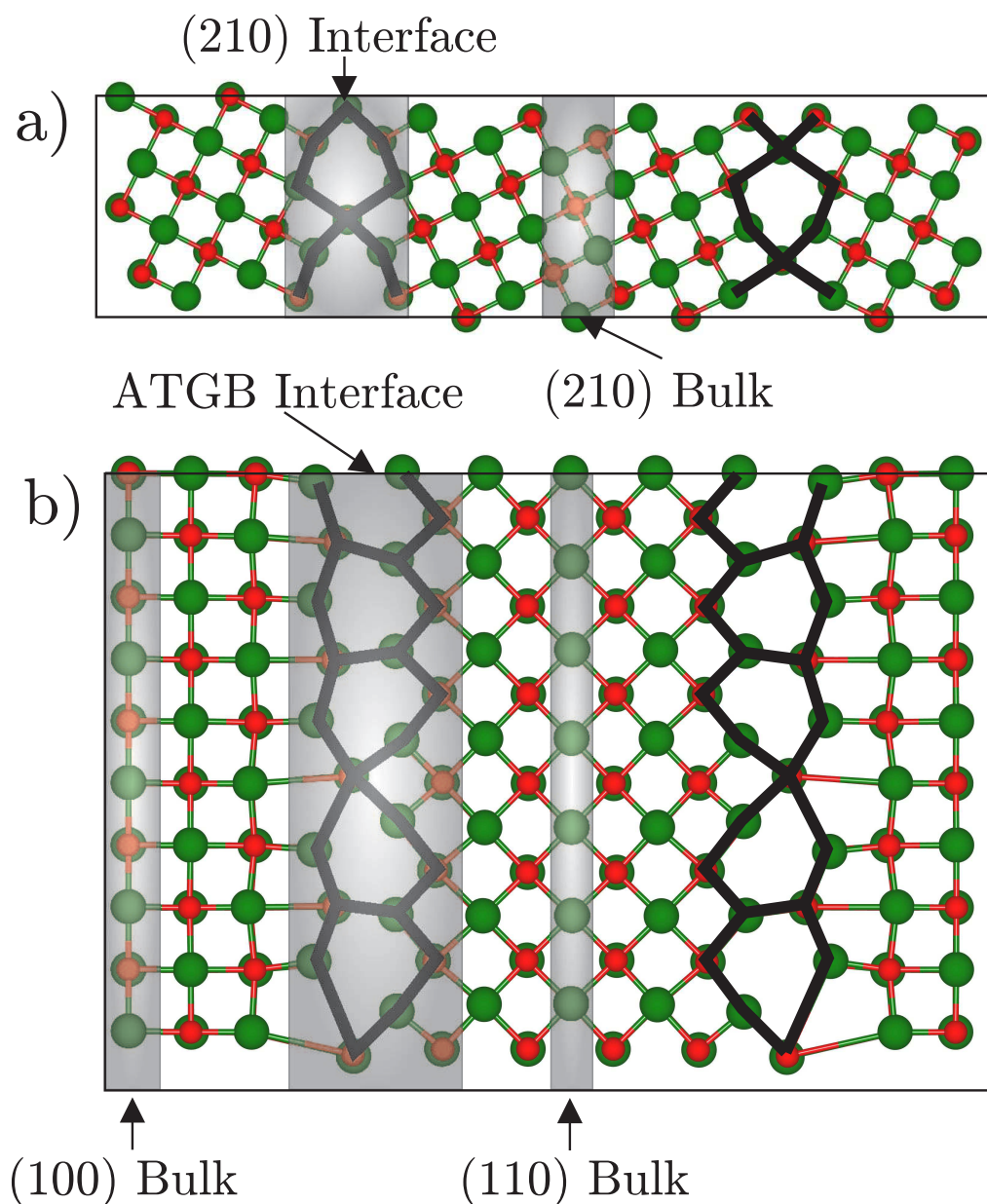
Figure 5.8: Supercells used to model commonly occurring grain boundary structures present in MgO films. a) $\Sigma 5(210)[001]$ symmetric tilt grain boundary and b) $(100)/(110)[001]$ asymmetric tilt grain boundary. Red and green atoms represent O and Mg respectively. Shaded areas highlight which atoms are used to produce the projected density of states shown in Fig. 5.10.

It is expected that the lowest energy configurations found using the systematic screening approach should correspond structurally to the GBs which are observed in the TEM

Table 5.1: Summary of theoretically predicted and experimentally properties of MgO. $E_{min|\text{fcc}}$ (eV) is the cohesive energy in the fcc phase, a_{fcc} (Å) is the lattice constant in the fcc phase, B_0 is the bulk modulus in GPa.

MgO	Lewis-Catlow	DFT (PBE)	DFT (HSE06)	Expt.
a_{fcc}	4.21	4.26	4.22	4.21 [256]
$E_{min|\text{fcc}}$	-10.27	-10.90		-9.89 [257]
B_0	225	150		164 [258]

images. Although many Buckingham potentials have been developed for MgO they do not significantly differ thus parameters of Lewis and Catlow are employed [196]. The usual tests are performed to ensure that this potential recovers the basic properties of MgO such as comparison between theoretical and experiment lattice constants and the bulk modulus. It is found that there is a good agreement between interatomic potentials, DFT and experiment (see Table. 5.1).

First principles calculations have been performed using the Vienna ab-initio simulation package (VASP) [259]. The projector augmented-wave method [260] at a cut-off energy of 350 eV using the GGA functional of Perdew, and a k-point mesh centred at the Γ point of 1×6×3 for the STGB and 1×6×1 for the ATGB. All atoms in the supercells were fully optimised with respect to interatomic force tolerance of 0.01 eV Å^{-1}. After this optimisation the electronic configuration of each system was then re-converged using the wavefunctions generated from the previous calculations with the hybrid functionals (HSE06). Hybrid functionals give a better agreement with experimental values for the electronic properties. As MgO is a paramagnetic material non-spin polarised calculations can be performed to increase throughput.

5.2.3 Electronic properties

With atomic models of the GB structures determined using density functional theory it is possible to predict the associated electronic properties. For each GB supercell the electronic density of states (DOS) using both the semi-local exchange correlation functional (PBE) and an exchange correlation functional including non-local exact exchange (HSE06) is computed. However, the latter gives a much more accurate prediction of the band gap of bulk MgO 7.2 eV (4 eV PBE) compared to the experimental value of 7.8

eV [261] and so is used for the results presented here. The DOS is projected onto bulk and interface regions of the supercell (see shaded areas in Fig. 5.8) in order to isolate the electronic states associated with the GB defects. In Fig. 5.9 the density of states for the ATGB and STGB are shown at the PBE level. Fig. 5.10a shows the DOS for the $\Sigma 5(210)[001]$ symmetric tilt GB using the HSE06 functional. The highest occupied electronic states in the supercell are associated with the GB (about 0.05 eV higher than the bulk valance band maximum). However, the most prominent feature is a wide band of states in a 2 eV (1 eV PBE) window below the bulk conduction band minimum. This effectively reduces the band gap at the GB to 5 eV (3 eV PBE), a reduction of 30% (25% PBE). For the (100)/(110)[001] asymmetric tilt GB the effects are even more striking. In this case the bulk regions of each grain are projected separately since due to the small unphysical strain in the supercell the DOS in the two bulk regions may in principle be different. However, as can be seen the difference is very small confirming that this strain has a negligible effect on predicted electronic properties. In the (100)/(110)[001] GB it is found that the highest occupied electronic states in the supercell are associated with the GB (about 0.2 eV higher than the bulk valance band maximum). However, again the most prominent feature is a wide band of states this time spanning a 3 eV (2 eV PBE) window below the bulk conduction band minimum. This reduces the band gap at the GB to 4 eV (2 eV PBE), a reduction of 45% (50% PBE). It is observed that the defect states associated with the GB closely resemble that of the HSE06 functional other than smaller band gap.
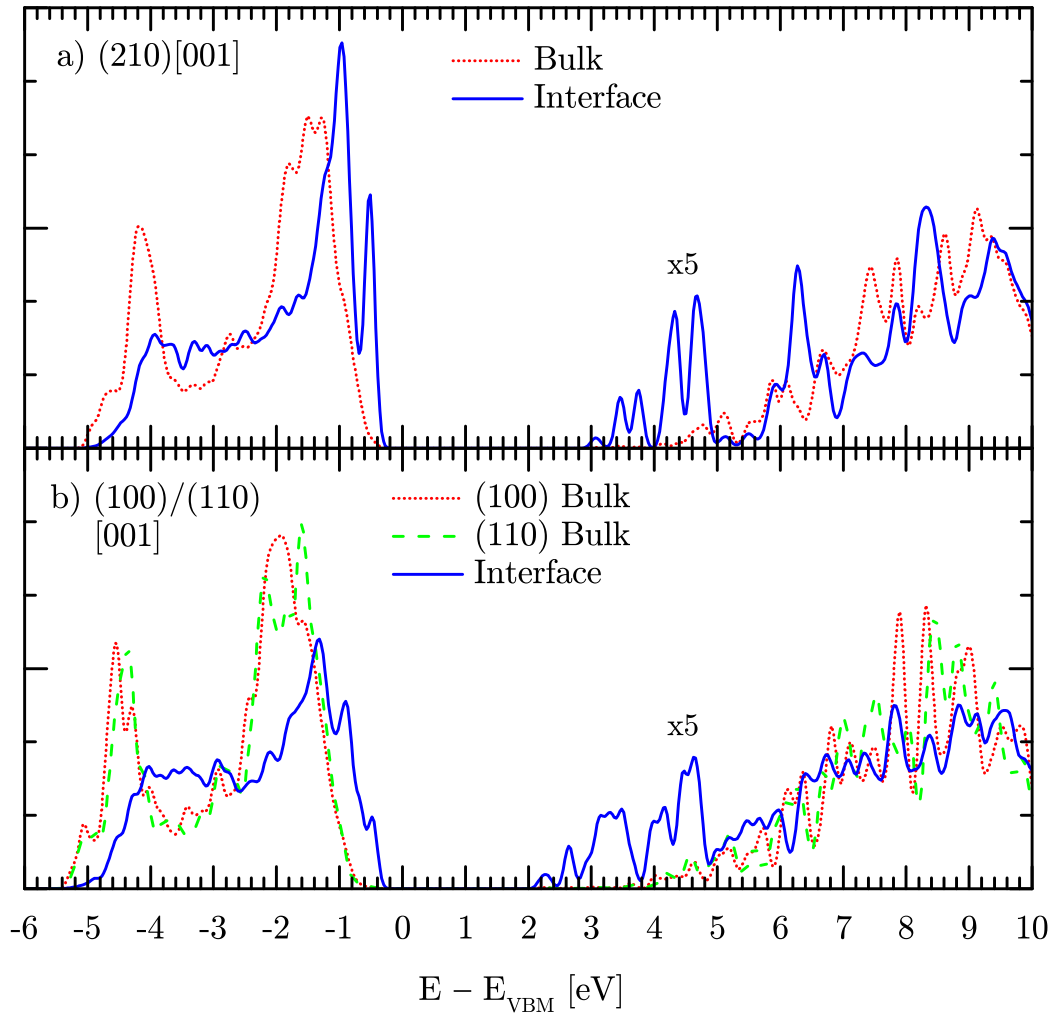
Figure 5.9: Density of states of the a) $\Sigma5(210)[001]$ symmetric tilt grain boundary and b) $(100)/(110)[001]$ asymmetric tilt grain boundary calculated using the Perdew Burke Ernzerhof functional. The density of states is projected onto bulk and interface regions. E_{VBM} is the energy of the bulk valence band maximum. The "×5" indicates the factor the density of states of the unoccupied states have been increased by to aid visualisation.
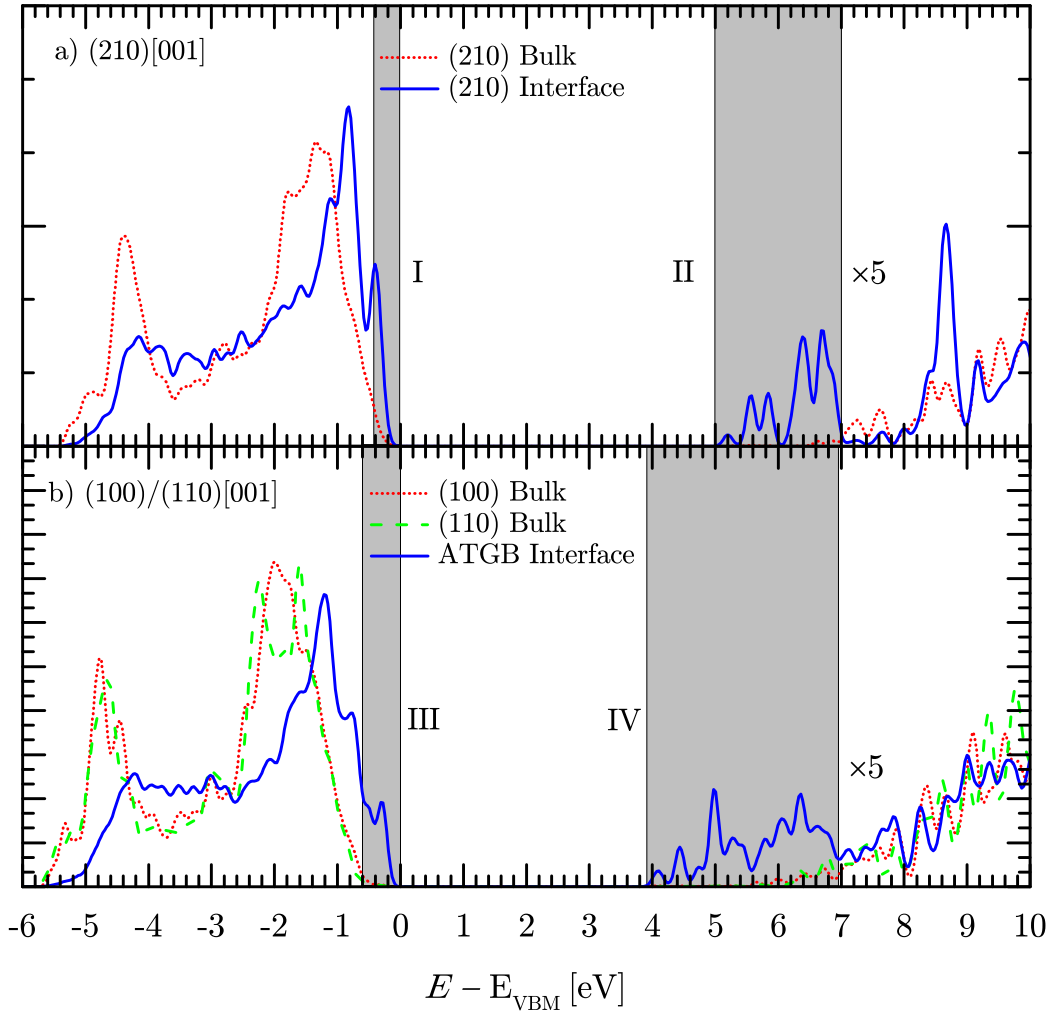
Figure 5.10: Density of states of the a) $\Sigma5(210)[001]$ symmetric tilt grain boundary and b) $(100)/(110)[001]$ asymmetric tilt grain boundary calculated using the Heyd Scuseria Ernzerhof functional. The density of states is projected onto bulk and interface regions (defined in Fig. 5.8). E_{VBM} is the energy of the bulk valence band maximum. Roman numerals indicate regions of interfacial electronic states. The "$\times5$" indicates the factor the density of states of the unoccupied states have been increased by to aid visualisation.

To provide further insight into the nature of the electronic states associated with GBs the total charge density (norm of the eigenfunctions) associated with electronic states in particular energy windows is determined. The total charge density of a selected range

106

of energies and k-points $\rho(\mathbf{r})$ is defined as follows,

$$\rho(\mathbf{r})|_{E_{min}}^{E_{max}} = \sum_{E_{min}<E_{i,k}<E_{max}} \sum_{k} |\phi_{i,k}(\mathbf{r})|^2 \tag{5.1}$$

where N is the total number of electrons, M is the total number of k-points, $\phi_{i,k}$ is the eigenfunction for electron i at each k-point and are defined such that the eigenfunctions correspond to energies between the limits of E_{max} and E_{min}. Four regions of interest within the gap of bulk MgO have been identified by shaded areas and Roman numerals in Fig. 5.10. In Fig. 5.11 the charge density isosurfaces associated with electronic states in these regions is shown. Regions I and III are associated with occupied states that are above the bulk valence band maximum in the $\Sigma5(210)[001]$ and $(100)/(110)[001]$ GBs respectively. For region I the charge density is associated primarily with five-coordinated oxygen ions near the GB while for region III it is associated with almost all interfacial oxygen ions. The states in regions II and IV fall below the bulk conduction band minimum. In both GBs they are localised inside the triangular structural units at the GB but are extended in the [001] direction (i.e. along the film normal). For the $(100)/(110)[001]$ GB it is notable that the deepest interfacial electronic states are localised preferentially in the largest structural units.
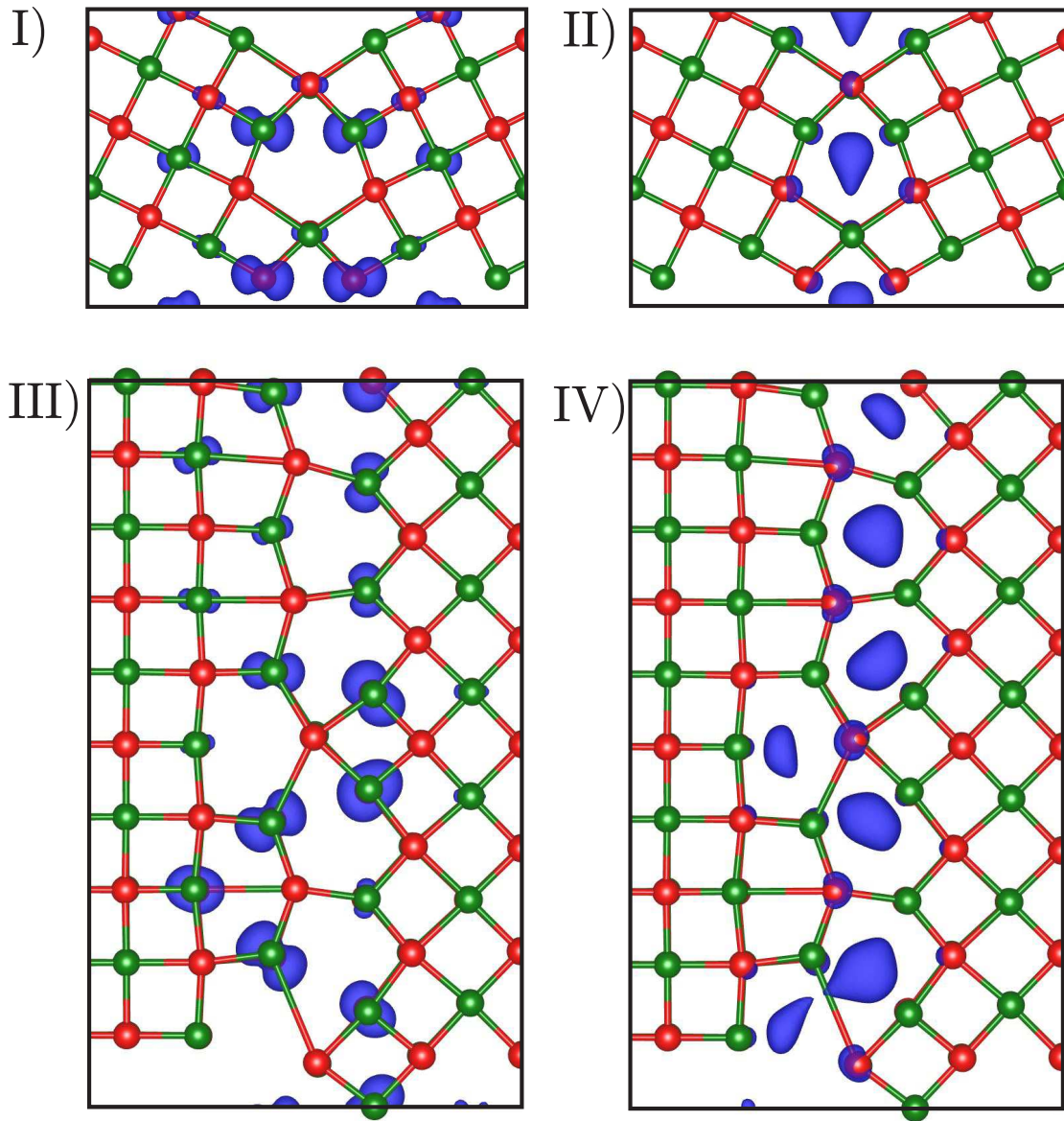
Figure 5.11: Total charge density (norm of the eigenfunctions) associated with electronic states in particular energy windows for the $\Sigma5(210)[001]$ symmetric tilt grain boundary and $(100)/(110)[001]$ asymmetric tilt grain boundary in MgO. The energy windows I−IV are highlighted in Fig. 5.10. The red and green atoms represent O and Mg respectively and the charge density is represented by the blue isosurfaces.

The above results show that electronic states associated with GBs in the MgO layer of MTJs locally reduce the band gap by up to 3 eV. This reduced gap will increase the amount of tunnelling current that is shunted through GBs rather than through the

bulk-like regions. Bulk MgO is associated with a very large magnetoresistance due to a symmetry filtering effect with values as high as 3400% predicted theoretically [55, 249]. However, due to reduced symmetry the local magnetoresistance at GBs is expected to be much lower [51, 262]. As a result of a proportion of the spin current flowing through GBs one may expect the effective TMR of a granular MgO barrier to be reduced relative to a single crystal barrier. It has been shown the variation of the TMR is dependent of the grain size [18].

5.3   Discussion

The structural and electronic properties of two representative GBs which exhibit structural units which are by far the most common as determined by a detailed analysis of ABF-STEM images have been characterised. Given the [001] texture of the films the presence of the symmetric $\Sigma 5(210)[001]$ tilt GB is consistent with its relatively low formation energy and high site coincidence. The asymmetric $(100)/(110)[001]$ tilt GB on the other hand was unexpected and is comparatively much less stable. This can be rationalised since the observed MgO microstructure is likely a result of highly non-equilibrium growth and post processing processes. The MgO films studied here are grown on amorphous FeCoB substrates which are then annealed, removing the boron and crystallising the FeCoB electrodes [17]. Interfaces between grains in the MgO film follow complex paths (Fig. 5.1) with small sections of planar GBs which are very difficult to model using first principles methods. However, since the structural units that compose these more complex GBs are similar to that in the planar GBs there is reasonable confidence that our computational model is representative. Calculations for the electronic properties of the GBs have been performed using the hybrid HSE06 functional. This approach predicts the band gap of bulk MgO within 0.6 eV of the experimental value, much better than standard local or semi-local functionals (typically underestimated by about 3 eV). Therefore, it should be a reliable approach for characterising the nature of the interface states. For both types of GB a relatively shallow splitting of interface states near the valence band maximum and a much deeper splitting of interface states below the conduction band minimum is found. This asymmetry is consistent with previous results for GBs in similar oxide materials such as HfO_2 [164, 263]. The use of PBE or HSE06 XC functionals does not change the qualitative result (i.e. that GBs locally reduce the

band gap). Here, focus has been on the electronic properties of pristine GBs however in reality it is likely that they may act as sites for the preferential segregation of intrinsic defects and impurities [177]. In general such defect segregation would increase the number of electronic states in the gap further deteriorating the insulating properties. EELS analysis on similar MTJ samples from previous work indicates that there is a not a significant concentration of impurities such as Fe, Co and B but the possibility cannot be completely excluded [16, 17]. The role of defect and impurity segregation and diffusion is an issue of interest for further study but is beyond the scope of the present work.

5.4   Conclusions

Careful preparation of MTJs allows samples of the MgO layer to be isolated. ABF-STEM imaging has been used in order to atomically resolve the granular structure of the MgO layer. The films are found to be highly textured in the [001] direction. Based on an analysis of these images commonly occurring GB structural units have been identified which have been used to construct models for first principles calculations. In this way characterisation of the electronic properties of buried GB defects inside a MTJ show that GBs locally reduce the MgO band gap by up to 3 eV. More generally this study shows that combining first principles modelling and state of the art electron microscopy can provide real insight into the structural properties of thin films. Such an approach could be expanded to films of other types to understand how the atomic structure changes with different material compositions.

Chapter 6

Structural stability of polycrystalline Fe/MgO interfaces in magnetic tunnel junctions

6.1   Introduction

In Chapter 5 the insulating properties of the MgO layer within MTJs was investigated. It was found that GBs can significantly reduce the insulating properties of the MgO. But the structure of the ferromagnetic layers is also important. It has been shown by experimental and theoretical studies that the best performing MTJs contain FeCoB as the active ferromagnet [55,56,264]. During the growth process FeCoB is amorphous when deposited and the MgO is polycrystalline [17,265]. The samples are usually annealed to crystallise the FeCoB but the complex nature of the crystallisation process is not well understood and the interfacial orientation between FeCoB and MgO is not explicitly known [18,53,54]. It has been shown using EELS measurements that the boron escapes from the FeCoB into a Ta layer during the annealing process leaving FeCo [17]. The FeCo which remains could exist in a significantly different orientational configuration relative to the MgO (see Fig. 6.1).

In general interfacial orientations could undermine the properties of any heterogeneous interface. Furthermore GBs could alter the properties of interfaces. To demonstrate the impact of different orientational configurations and GBs on heterogeneous interface Fe is considered as the electrode and MgO as the insulating barrier layer.

The simplest interface which can be constructed between Fe and MgO is an epitaxial interface where the atomic columns are in registry (see Fig. 6.6). Many previous

theoretical calculations have computed the properties of the Fe/MgO epitaxial interface but a stability analysis of different interfacial configurations of Fe and MgO is currently missing [17, 266–268].

In this chapter the orientational relationship between Fe and MgO interfaces in four distinct scenarios is explored (see Fig. 6.1). The four types are: Type A contains no GBs in either Fe or MgO, type B contains GBs in the Fe but none in MgO, type C contains GBs in the MgO but none in Fe and type D contains GBs in both Fe and MgO. The supercell approach is used to define twelve Fe/MgO interface systems spanning the four scenarios. First principles calculations are performed to compute the formation energy of each of the interfaces which are compared then ranked. Bader analysis is performed to understand whether there is any charge transfer between the two materials (see Sec. 3.2). It is concluded that certain interface configurations are intrinsically unstable and are extremely unlikely to occur while others are very stable and are likely to occur. From the results gathered in this chapter a qualitative understanding of the relationship between the grain sizes of the Fe substrate and MgO film in MTJs can be deduced.
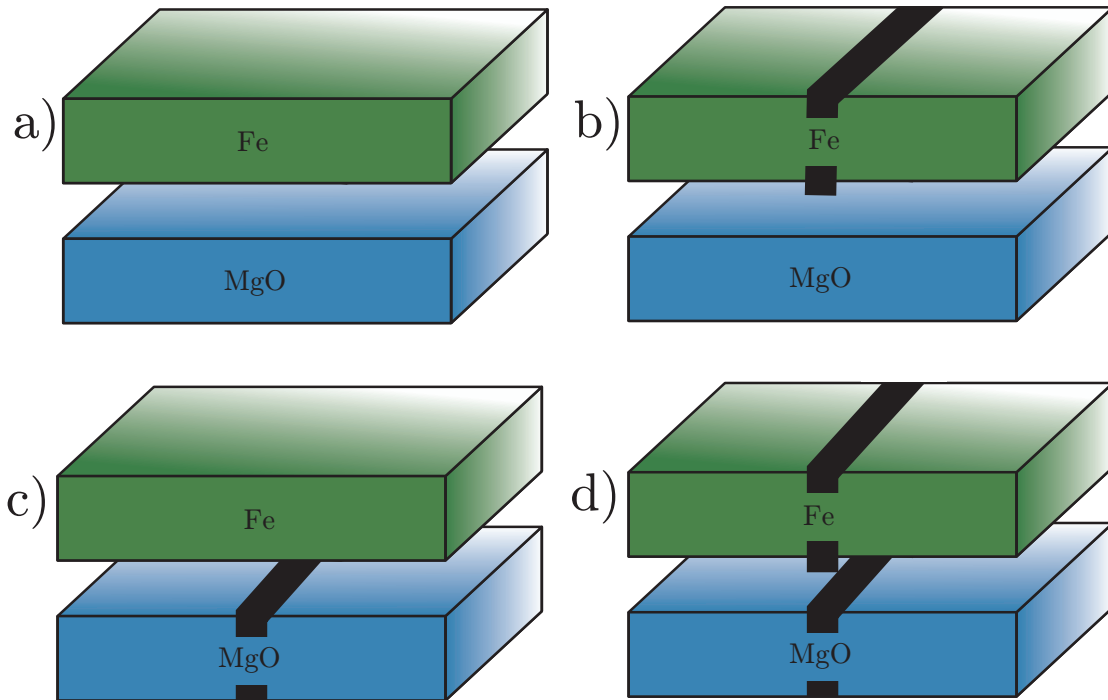
Figure 6.1: Schematic showing the types of Fe/MgO interface structure a) Type A interface (Bulk Fe and bulk MgO) b) Type B (Grain boundary in Fe and bulk MgO) c) Type C (Bulk Fe with grain boundary in MgO) d) Type D (Grain boundary in Fe and bulk MgO).

This chapter is structured in the following way. In Sec. 6.2 a mathematical notation and its shorthand used to specify the four types of interfaces is introduced along with details of the computational methods and validation used. In Sec. 6.3 the results of the stability analysis of different orientations and GB structures of Fe/MgO interfaces is given. In Sec. 6.4 the results are discussed and in Sec. 6.5 the main conclusions are presented.

6.2   Methods

Interfaces of the type B-D described in the introduction (see Fig. 6.1) which are investigated in this chapter have not yet been studied by other researchers thus no notation has been established to classify them. New notation has been defined to characterise the new interfaces. For the type A interface there is already a classification notation

established but is compatible with the new notation. The type A interface is depicted in Fig. 6.2 and is comprised of two films without GBs.

crystal I

$[m_2n_2o_2]$

$[h_2k_2l_2]$

$[h_1k_1l_1]$
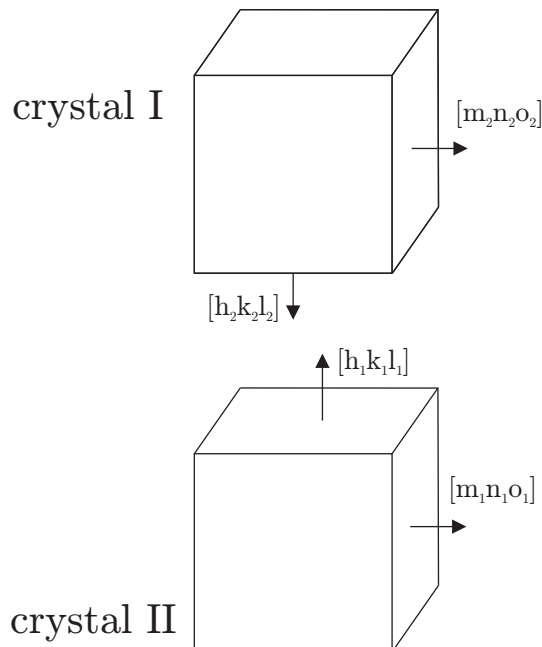
$[m_1n_1o_1]$

crystal II

Figure 6.2: Schematic showing how type A interfaces are defined mathematically.

In Fig. 6.2 the growth directions of the crystals I and II are specified by $[h_1k_1l_1]$ and $[h_2k_2l_2]$ respectively. The other directions in the crystals $[m_1n_1o_1]$ and $[m_2n_2o_2]$ are important to quantity how much twist may be present in the films. It is possible to express the type A interface in the new notation, defined below,

$$\text{Fe}(h_1k_1l_1)[m_1n_1o_1] \parallel \text{MgO}(h_2k_2l_2)[m_2n_2o_2], \tag{6.1}$$

where the first term before the parenthesis () describes the element(s) involved in the interface (and their stoichiometry e.g. Fe or $Fe_{40}Co_{60}$). The numbers in round brackets () refer to the Miller indices of the interfacial plane for crystals I and II. The numbers in the square brackets [] refer to the Miller indices of a direction perpendicular to the interface plane and $\parallel$ states the vectors $[m_1n_1o_1]$ and $[m_2n_2o_2]$ are aligned parallel. Note that it is possible to completely specify a crystal using only two lattice vectors as the third can be found using the cross product.

In the case of type B interfaces (shown in Fig. 6.3) an additional term needs to be added in the Fe film to include a GB. The additional term specifies a tilt GB about the

114

interface normal in the Fe layer.
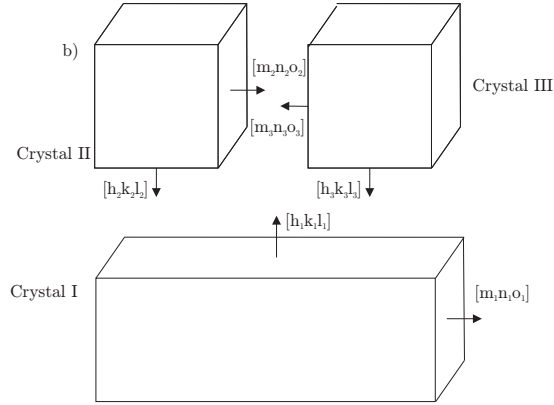
Figure 6.3: Schematic showing how type B interfaces are defined mathematically.

The film can be specified mathematically by adding the following term $Fe(h_1k_1l_1)[m_1n_1o_1]/[m_3n_3o_3]$ which describes another granular orientation $[m_3n_3o_3]$ shown in complete form,

$$Fe(h_1k_1l_1)[m_1n_1o_1]/[m_3n_3o_3] \parallel MgO(h_2k_2l_2)[m_2n_2o_2]. \qquad (6.2)$$

In using such a description crystal III is composed of two lattice vectors $[h_3k_3l_3]$ and $[m_3n_3o_3]$. A similar procedure for type C interfaces can be employed but with the additional GB term in the MgO rather than the Fe. Describing type D interfaces (see Fig 6.4) requires adding a further term to describe a GB in the MgO, given below,
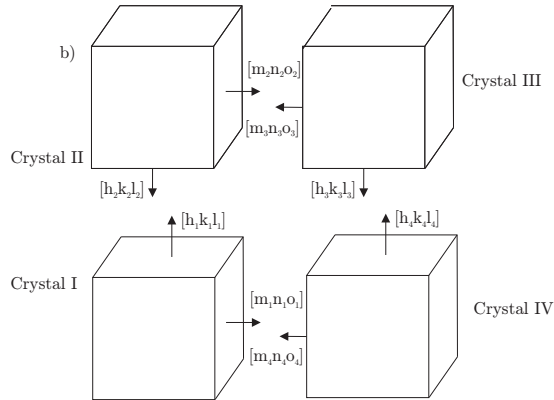
Figure 6.4: Schematic showing how type D interfaces are defined mathematically.

$$\text{Fe}(h_1k_1l_1)[m_1n_1o_1]/[m_3n_3o_3] \parallel \text{MgO}(h_2k_2l_2)[m_2n_2o_2]/[m_4n_4o_4]. \qquad (6.3)$$

In a similar way to the type C interfaces crystal IV is composed of the orthogonal vectors $(h_4k_4l_4)[m_4n_4o_4]$. Using this notation allows the complete specification of either a simple interface with no GBs (Eqn. 6.1) or specification of GBs in either or both materials comprising the interface (Eqns. 6.2 & 6.3).

First principles calculations have been performed using VASP [259] to compute the total energies of the systems explored in this chapter. The projector augmented-wave method [260] with a cut-off energy of 350 eV using the GGA functional and a MP k-point mesh of 6×6×6 for the type A systems and 1×1×1 for all the other systems. The k-points were centred at the Γ point. All atoms in the supercells were fully optimized with respect to interatomic forces to a tolerance of 0.1 eV Å^{-1}. Spin polarised calculations are performed as Fe is a magnetic material[1]. It is important to initially specify the expected approximate magnetic moment as there are different magnetic states of Fe. The total number of atoms which can be feasibly modelled is of the order 1000. See the methods chapter (Sec. 3.1.2.2) for more detail on DFT.

Interface supercells of Fe and MgO are constructed from either bulk slabs or the optimised GBs from other calculations in previous chapters. In all supercells created the strain was equally distributed in the directions perpendicular to the lattice vectors between both of the cells. When supercells which have been optimised with EAM potentials the lattice constants are rescaled with respect to the DFT bulk optimised lattice constants. Initially the calculations were performed with a vacuum gap but it is extremely difficult to optimise the surfaces of GBs. In many cases the surface becomes very disordered and does not reach an energy minimum. To resolve the lack of convergence the vacuum gap was removed and interfaces were constructed with two bulk cells. Such an approach is an approximation as the resulting formation energy will also be dependent on the degree of strain which the Fe/MgO constituent crystals. This is an approximation but it is not thought to be significant as the amount of strain induced in each crystal is likely to be less than 5%. The degree of relaxation should be relatively small in the case of the stable interfaces. Unstable interfaces will be extremely repulsive and posses a higher formation energy as a result. The formation energy (E_f) of

---

[1]In DFT the spin degree of freedom can be ignored to simplify computation. Turning off the spin degree of freedom should only be done with non-magnetic materials.

each interface was then computed by calculating the total energy difference between the supercell containing the GBs and the two separated systems. In the case of interfaces between different materials the general equation for the formation energy is a modified version of the Young-Dupre equation [269] shown below,

$$E_f = \frac{E_A + E_B - E_{AB}}{2A}, \tag{6.4}$$

where E_A is the energy of the system A, E_B is the energy of the system B, E_{AB} is the energy of the combined system and A is the surface area of the interface. The interface formation energies are used to rank the energetic stability of the four types of interfaces.

When performing calculations of this kind it must ensured that there are enough layers in each crystal to minimise finite size effects and describe the system accurately. A testing procedure was devised to understand the variation of finite size effects. It is expected that interface formation energy should converge with enough layers of Fe and MgO. For simplicity the epitaxial interface was used for this purpose (see Fig. 6.6). Supercells are constructed with different numbers of Fe and MgO layers and optimised to find the total energies. In the bulk configuration it is not possible to add single layers of Fe as these correspond to stacking faults as the Fe would not be periodic, so bi-layers are added. The results of the testing procedure are shown in Fig. 6.5. It is found that a single or double Fe bi-layer does not give a well converged interface formation energy regardless of how many MgO mono-layers are added. For all other systems the interface formation energy is well converged with respect to MgO and Fe layers. It can be concluded that since there is only a small deviation between the interface formation energies with different layers when the number of Fe bi-layers (>2). Giving confidence that 3 bi-layers of Fe and 4 layers of MgO are sufficient to accurately describe our system.
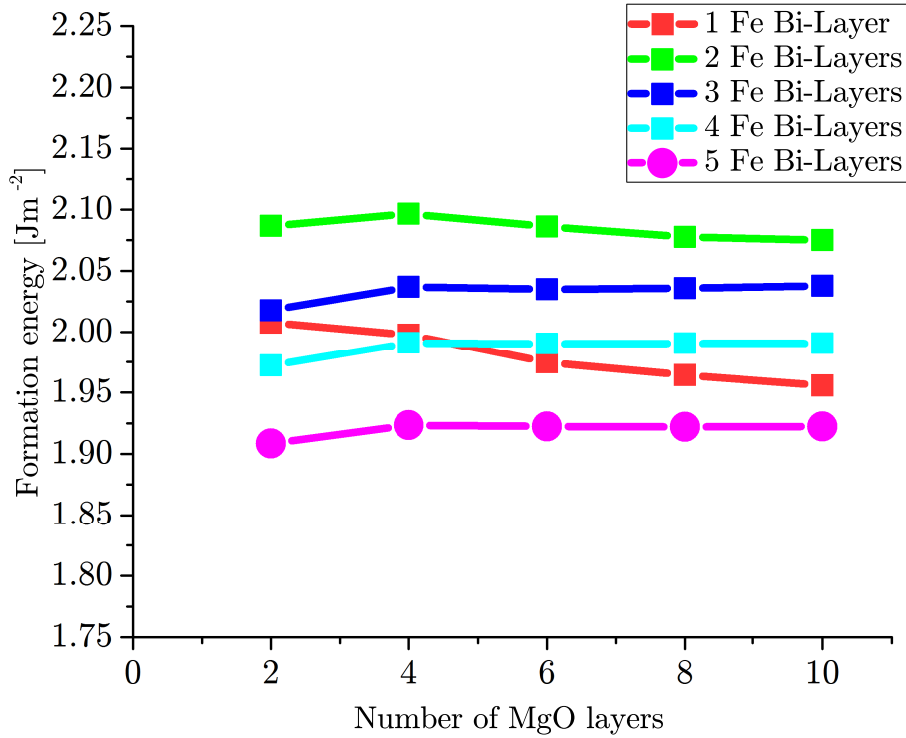
Figure 6.5: Formation energy for the Fe(001)[100] || MgO(001)[110] interface with varying thicknesses of MgO and Fe.

Although this procedure of increasing the thickness has only been performed with one interface type it is expected that the perturbation to the interface (i.e. from transfer of charge or reduction in local symmetry) should not significantly alter the number of layers required to achieve a converged interface formation energy for different orientational configurations.

6.3   Results

Type A interfaces

A total of three different type A interfaces were considered including: Fe(001)[100] || MgO(001)[110], Fe(001)[100] || MgO(001)[100] and Fe(001)[310] || MgO(001)[100]. The most stable interface is found to be the epi-

taxial interface Fe(001)[100] || MgO(001)[110] containing bcc Fe with fcc MgO rotated by 45° about the [001] axis (see Fig. 6.6a). The Fe(001)[100] || MgO(001)[110] epitaxial interface possesses a low total strain in the lattice vectors perpendicular to the interface direction ($< 3\%$). The interfaces were not optimised in the direction parallel to the interface normal as explained in the previous section. The closest bond formed between Fe and MgO is between the Fe and O atoms and the system has a formation energy of 2.0 Jm^{-2}. An alternative configuration can be found by shifting the MgO relative to the Fe such that Mg is directly bonded to Fe. When the Fe is bonded directly to the Mg atom the formation energy is 5.0 Jm^{-2} (see Fig. 6.6b). The formation energy for the alternative configuration is extremely high. It is unlikely that MgO is bound to Fe in the alternative configuration. In the alternative interface the Fe and MgO crystals become compressed in the interface normal direction by around ∼5%. The compression is also reflected in the nearest neighbour bond length between Fe-Mg (2.49 Å) compared with the Fe-O bond length in the more stable configuration (2.07 Å). Such compression is an artefact of the way in which the supercells were optimised but is small. Considering that this is the worst case scenario other simulation cells are likely to be less affected.
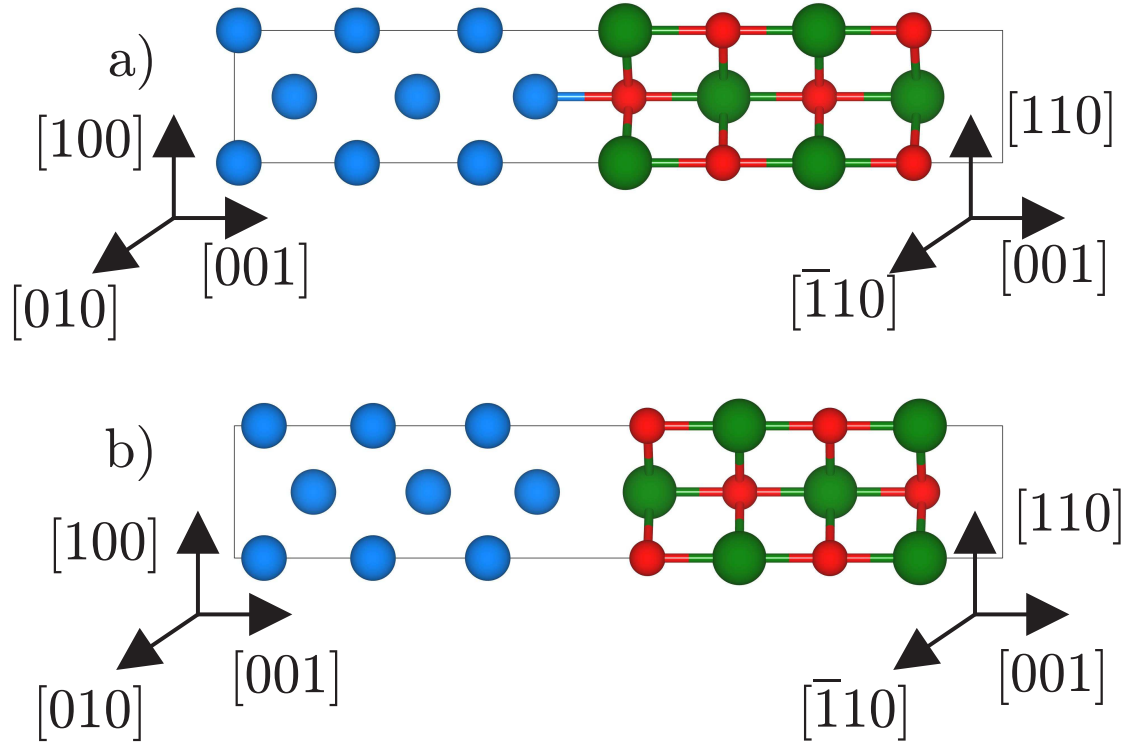
Figure 6.6: Fe(001)[100] || MgO(001)[110] epitaxial interface without a vacuum gap. Fe is shown in light blue with Mg in green and O in red. a) With Fe directly above O b) with Fe directly above Mg.

Using Bader analysis (see Sec. 3.1.2.2) it is possible to determine the degree of charge transfer between Fe and MgO. In the most stable interface (Fig.6.6a) it is found that the O atom polarises the nearest Fe atom to a charge of $+0.08e$ with the O atom being relatively unchanged with respect to the other oxygen atoms in the MgO structure $(-1.72e)$. In the case of the less stable interface (Fig. 6.6b) the Bader analysis shows that the Fe polarises negatively to $(-0.03e)$. Such small polarisations of the surface of Fe in the presence of MgO represents a small degree of charge transfer.

To further characterise the Fe/MgO interfaces the atom projected centred electrostatic potential can be calculated using the equation below,

$$U = \int V(r)\rho(r)d^3r, \tag{6.5}$$

where $V(r)$ is the electrostatic potential of the whole system at a position r and $\rho(r)$ is a spherical test charge. The test charge radii depends on the element and are Fe (1.01

Å) Mg (0.83 Å) and O (0.87 Å). The average electrostatic potential for the epitaxial interface Fe(001)[100] ‖ MgO(001)[110] is shown in Fig. 6.7. There is no significant deviation between the bulk-like regions in the centre of the crystal and the interface indicating along with the Bader analysis little or no charge transfer between Fe and MgO.
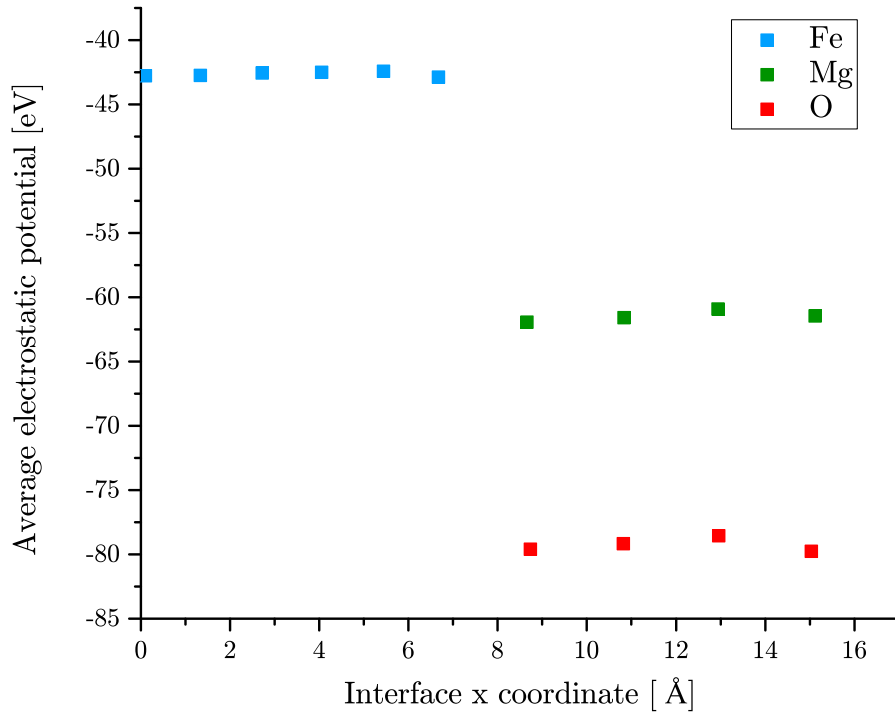
Figure 6.7: Average electrostatic potential of the epitaxial Fe(001)[100] ‖ MgO(001)[110] interface without a vacuum gap. The x-axis represents the coordinates of the supercell (in the interface normal direction) in Å.

The other type A configurations possess formation energies which are extremely high and are likely to be unfavourable (see Tab. 6.1).

Type B interfaces

The second class of interface considered (type B) are those where the MgO films composing the interface are perfect i.e. contain no GBs or other defects but there are GBs in the

Fe substrate. In the type B class of interface there are three systems which are explored. These are: Fe(001)[100]/[110] || MgO(001)[110] this is an interface with an ATGB in the Fe and bulk-like in the [110] direction in MgO, Fe(001)[100]/[110] || MgO(001)[100] which contains an ATGB in the Fe but is bulk-like in the [100] direction in the MgO and Fe(001)[310]/[$\bar{3}\bar{1}0$] || MgO(001)[100] which contains a (310) STGB in the Fe and the MgO is bulk-like in the [001] direction. Of the first two type B systems with the ATGB in the Fe Fe(001)[100]/[110] || MgO(001)[110] and Fe(001)[100]/[110] || MgO(001)[100]) it is found that the ATGB in the Fe becomes incredibly disordered and the GB is not visible. The disorder is created during the optimisation of the atomic positions. An example of the disordered structure for Fe(001)[100]/[110] || MgO(001)[110] is shown in Fig. 6.8. It can be safely inferred that this kind of interface is unlikely to exist in nature as the number of layers of both the MgO and Fe in the real system will restrict the possibility of the GB transforming in this way. The formation energy is found to be 2.1 Jm^{-2} which is low enough to be stable but it is very unlikely that a reconstruction of the GB in the Fe would occur in this way. The Fe(001)[100]/[110] || MgO(001)[100] interface undergoes a similar transformation to the Fe(001)[100]/[110] || MgO(001)[110]. The other type B interface Fe(001)[310]/[$\bar{3}\bar{1}0$] || MgO(001)[100] with the (310) STGB in the Fe and no GB in the MgO is extremely unstable with a formation energy of 3.2 Jm^{-2}. The Fe(001)[310]/[$\bar{3}\bar{1}0$] || MgO(001)[100] interface however does not undergo any reconstruction.
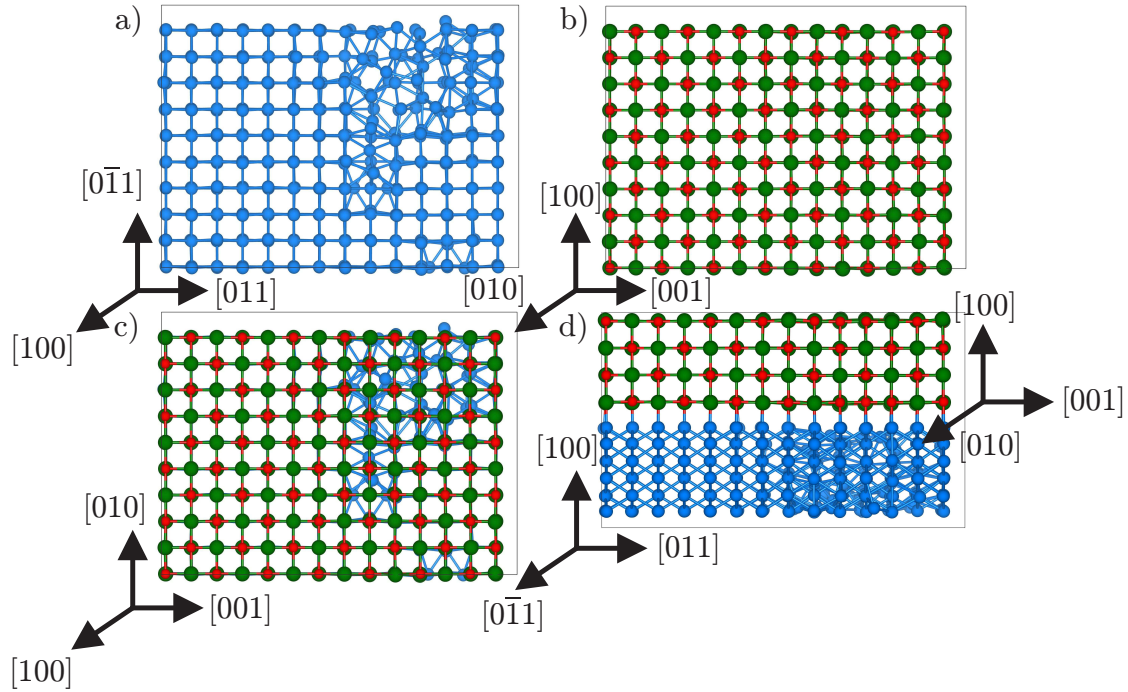
Figure 6.8: Optimised geometry of the Fe(001)[100]/[110] || MgO(001)[110] interface. Fe is shown in light blue with Mg in green and O in red. a) Fe only b) MgO only c) Top view d) Side view.

Type C interfaces

Next type C interfaces (those with GBs in the MgO but no GBs in Fe) were explored. Here four interfaces have been considered: Fe(001)[100] || MgO(001)[110]/[100], Fe(001)[110] || MgO(001)[110][100], Fe(001)[100] || MgO(001)[210]/[$\bar{2}\bar{1}0$] and Fe(001)[110] || MgO(001)[210]/[$\bar{2}\bar{1}0$]. The type C class of interfaces visually distort much less than type B but the formation energies are on average much higher with only two interfaces possessing a formation energy of less than 3.0 Jm^{-2}. The fully relaxed structures for the two stable structures Fe(001)[100] || MgO(001)[110]/[100] and Fe(001)[110] || MgO(001)[210]/[$\bar{2}\bar{1}0$] are shown in Figs. 6.9 & 6.10.
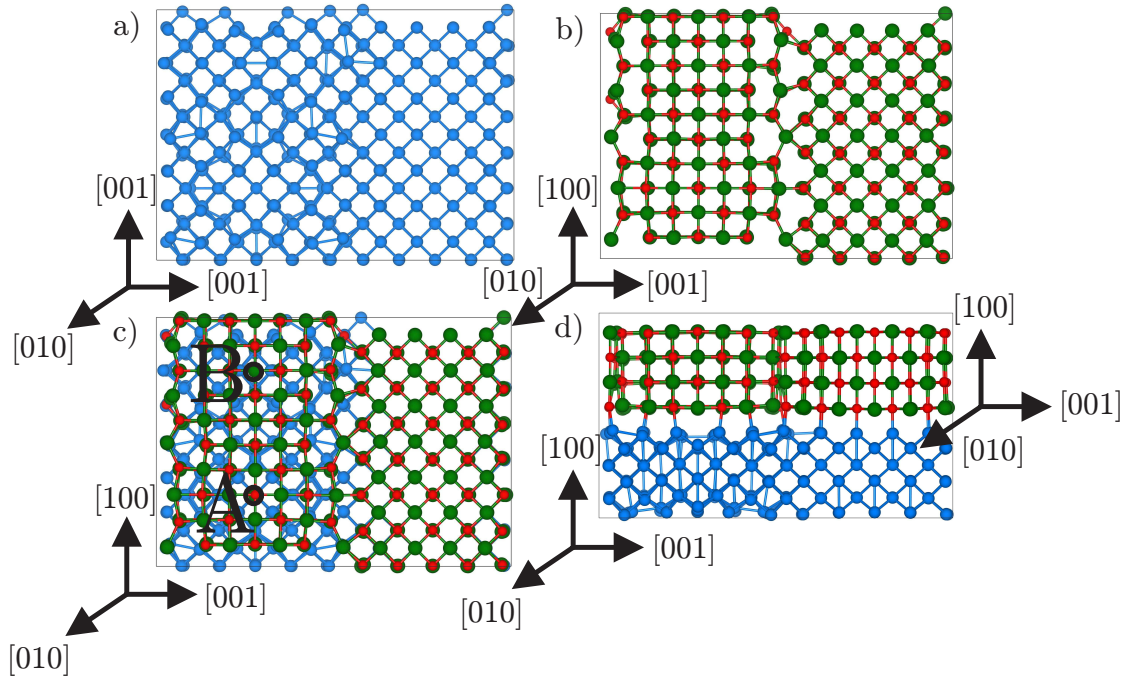
Figure 6.9: Optimised geometry of the Fe(001)[100] || MgO(001)[110]/[100] interface. Fe is shown in light blue with Mg in green and O in red. a) Fe only b) MgO only c) Top view d) Side view. Note the interesting Moiré pattern between points A and B.

For the first of the stable structures Fe(001)[100] || MgO(001)[110]/[100] the formation energy is found to be 2.5 Jm^{-2}. It is observed that the right side of the system is perfectly commensurate (corresponding to the Fe(001)[100] || MgO(001)[110] interface) but the left side contains small structural perturbations in the Fe near the interface. There is an interesting Moiré pattern of repeating points every five neighbours (between points A->B in Fig. 6.9). Finally a system containing the substrate in the (110) orientation is considered. The fact that interfaces of the type Fe(001)[100] || MgO(001)[110]/[100] are stable theoretically is explored further in Sec. 6.3.1.

The second stable structure of the type C interfaces is Fe(001)[110] || MgO(001)[210]/[$\bar{2}\bar{1}$0]. Fe(001)[110] || MgO(001)[210]/[$\bar{2}\bar{1}$0] contains a (210) STGB in MgO and no GB in the Fe (001)[110] substrate (see Fig. 6.10). The formation energy for Fe(001)[110] || MgO(001)[210]/[$\bar{2}\bar{1}$0] is found to be 2.5 Jm^{-2} which again suggests that interfaces of this kind could be found experimentally. Interestingly Fe(001)[110] || MgO(001)[210]/[$\bar{2}\bar{1}$0] does not show any significant perturbations of either the MgO or the Fe.
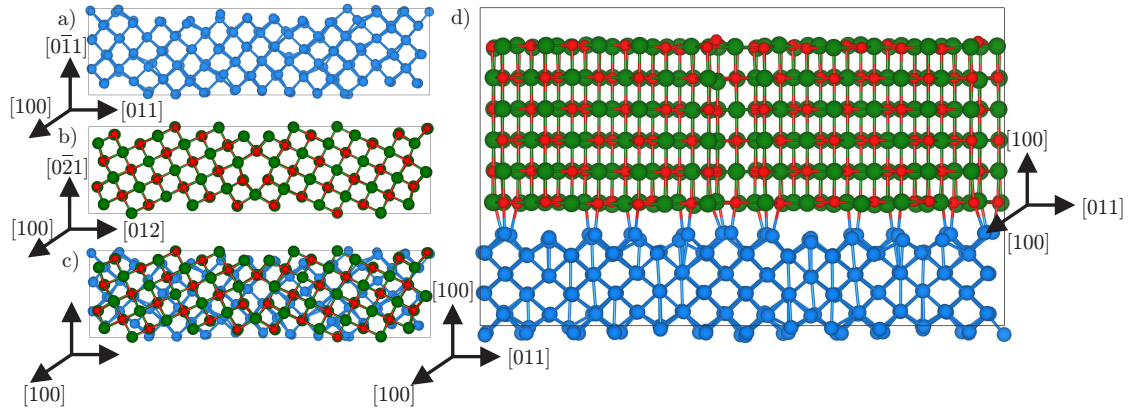
Figure 6.10: Optimised geometry of the Fe(001)[110] || MgO(001)[210]/[$\bar{2}\bar{1}0$] interface. Fe is shown in light blue with Mg in green and O in red. a) Fe only b) MgO only c) Top view d) Side view.

Type D interfaces

The final class of systems considered are those containing the same GB in both MgO and Fe (type D). Here there are only two systems which can be constructed due to the restrictions of the total numbers of atoms, these are: Fe(001)[100]/[110] || MgO(001)[110]/[100] and Fe(001)[310]/[$\bar{3}\bar{1}0$] || MgO(001)[210]/[$\bar{2}\bar{1}0$] are shown in Figs. 6.11 and 6.12 respectively.
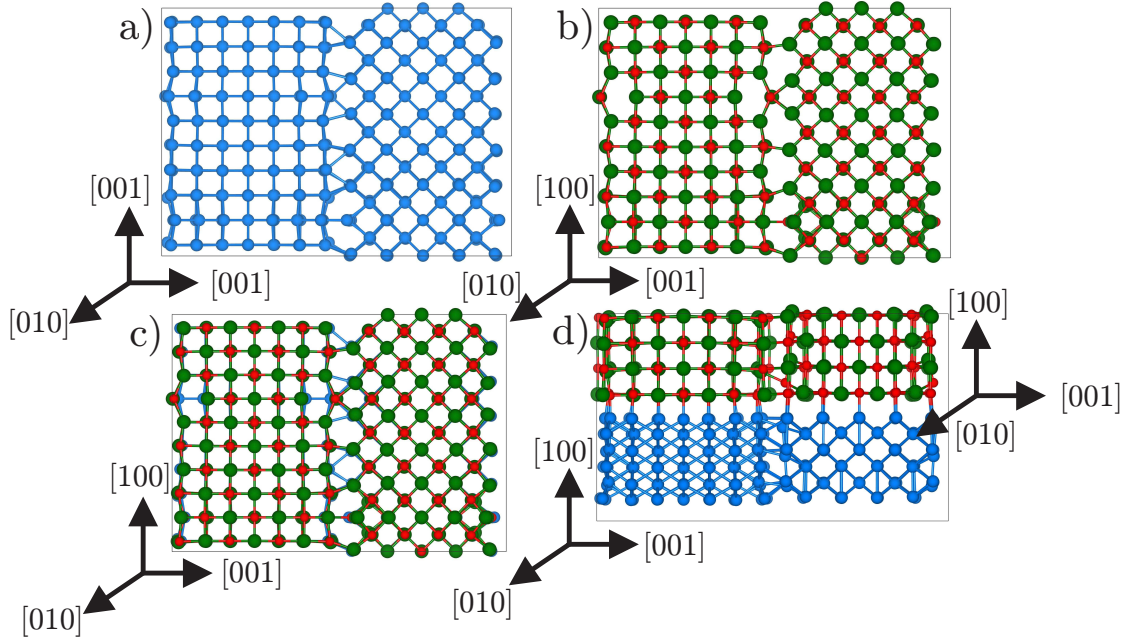
Figure 6.11: Optimised geometry of the Fe(001)[100]/[110] || MgO(001)[110]/[100] interface. Fe is shown in light blue with Mg in green and O in red. a) Fe only b) MgO only c) Top view d) Side view.

For the first interface Fe(001)[100]/[110] || MgO(001)[110]/[100] the formation energy is found to be 1.6 Jm^{-2} which is extremely energetically favourable. Analysis of the local structure in (shown in Fig. 6.11) shows that there are some structural perturbations of the MgO where some of the atoms become deflected out of the plane however the atomic columns when viewed from above are distinctly defined. An analysis of the Bader charges indicates that the Fe atoms only become weakly charged in the presence of MgO. For the other stable type D interface Fe(001)[310]/[$\bar{3}\bar{1}$0] || MgO(001)[210]/[$\bar{2}\bar{1}$0] the atomic columns are in registry between Fe and MgO and the formation energy for this system is given as 1.8 Jm^{-2} (see in Fig. 6.12). The reason for the reduced formation energy when compared to Fe(001)[100] || MgO(001)[110] (which should be the most stable) is likely due to a structural relaxation in both of the GBs which reduces the formation of the GBs in Fe and MgO for both Fe(001)[100]/[110] || MgO(001)[110]/[100] and Fe(001)[310]/[$\bar{3}\bar{1}$0] || MgO(001)[210]/[$\bar{2}\bar{1}$0].
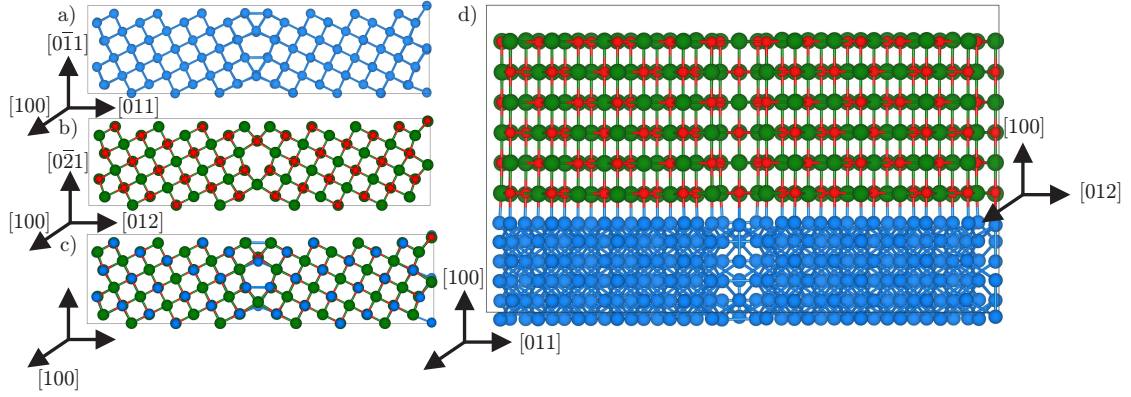
Figure 6.12: Optimised geometry of the Fe(001)[310]/[$\bar{3}\bar{1}0$] || MgO(001)[210]/[$\bar{2}\bar{1}0$] interface. Fe is shown in light blue with Mg in green and O in red. a) Top only Fe only b) Top only MgO c) Top view d) Side view.

Summary

The results for all of the interface systems are summarised in Table. 6.1. The most stable configurations are when the GBs in the MgO and Fe are in registry with each other e.g. Fe(001)[100] || MgO(001)[110], Fe(001)[100]/[110] || MgO(001)[110]/[100] and Fe(001)[310]/[$\bar{3}\bar{1}0$] || MgO(001)[210]/[$\bar{2}\bar{1}0$]. Such systems are stable because they possess the highest number of close Fe-O bonds. This is because the Fe-O interaction is attractive while Fe-Mg interaction is repulsive thus supercells with a lower average Fe-O bond length are those where there is a better lattice matching between the Fe and MgO. The Fe-Mg interaction creates additional strain in the interfacial normal direction resulting in compression. The average bond length is estimated by taking the average of the Fe-O bonds under 2.82 Å in length and dividing by the total number. A 2.82 Å cut-off was chosen as it lies between the distance between the first nearest neighbour (2.07 Å) and the second nearest neighbour (3.57 Å) in the Fe/MgO epitaxial interface. It is found that there is approximately a linear correlation between the average Fe-O bond length and the interface formation energy (see Fig. 6.13). Further to the average bond length it is possible to compare the Fe-O bond density with the interface formation energy (see Fig. 6.14). It is found that there is a broad negative correlation between close Fe-O bond density and the interface formation energy. Note that since there may be additional strain present in the interfaces due to the fact that the interfaces were not relaxed in the interface normal direction the choice of the cut-off for the Fe-O bonds is

somewhat arbitrary.
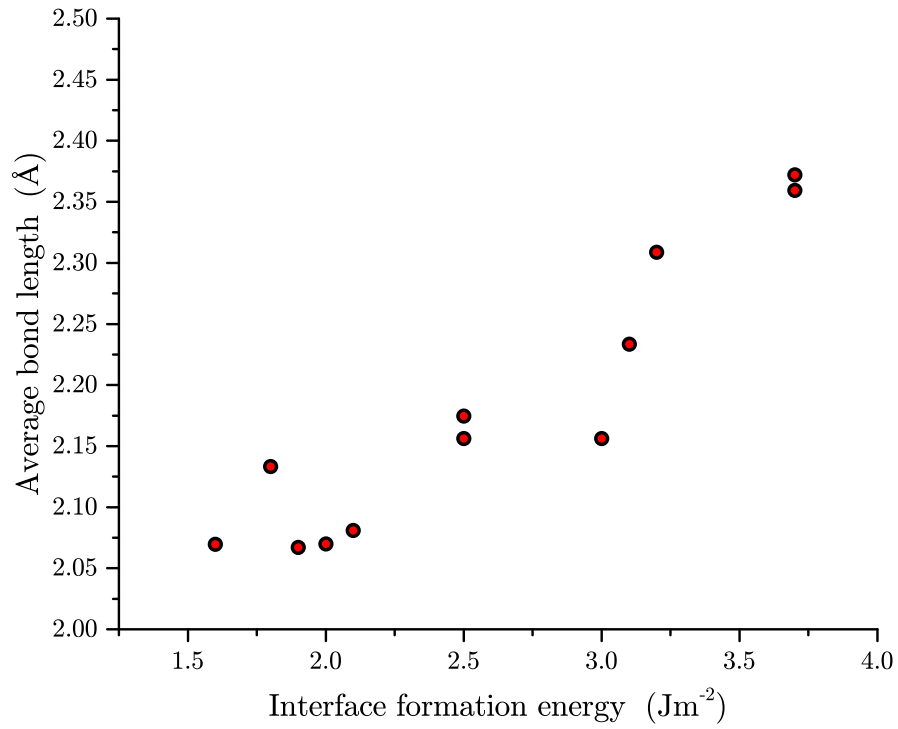
Figure 6.13: Interface formation energy (Jm^{-2}) plotted against average bond length of interface Fe-O bonds under 2.82 Å for all Fe/MgO interfaces.
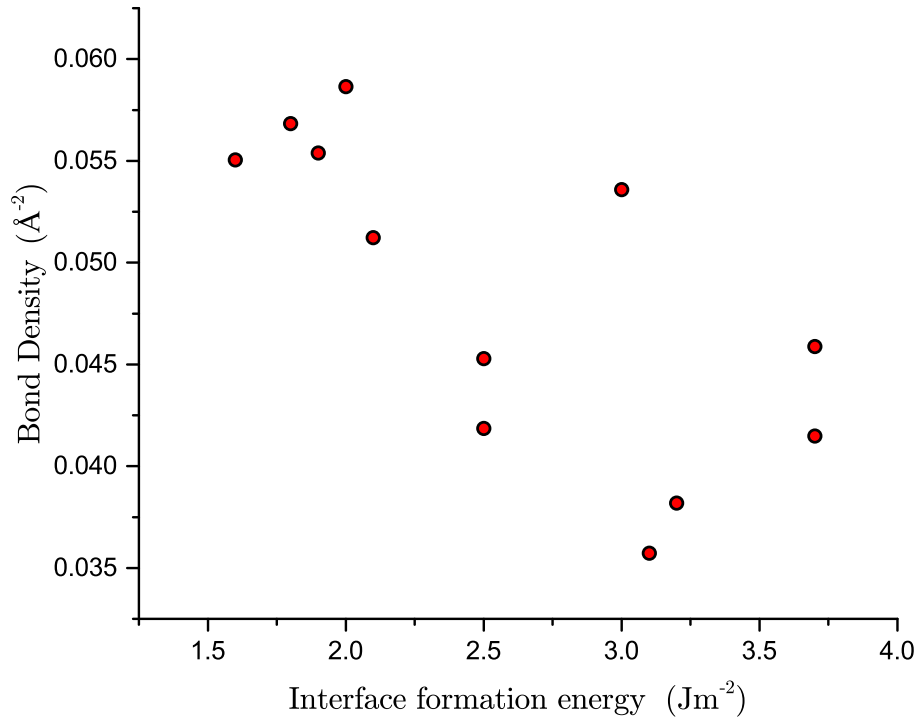
Figure 6.14: Interface formation energy (Jm^{-2}) plotted against bond density for Fe-O bonds under 2.5 Å for all Fe/MgO interfaces.

In two of the type B interfaces Fe(001)[100]/[110] || MgO(001)[110] and Fe(001)[100]/[110] || MgO(001)[100]) with an ATGB in the Fe the interfaces undergo a strong structural relaxation in the Fe such that it becomes more bulk-like with many dislocations appearing. Interfaces which have undergone such a strong relaxation to become stable are unlikely to be physical as if the number of monolayers in both Fe and MgO were to increase it would become harder for this type of structural relaxation to occur. The structural relaxation in effect occurs due to the ratio between the bond energy of the Fe-O bond (4.22 eV) and the Fe-Fe bond (1.22 eV) [270]. The system gains energy if an Fe-Fe bond is broken and an Fe-O bond is formed. Many of the other systems with formation energies which are greater and equal to 3.0 Jm^{-2} are extremely unlikely to occur. Thus it can be concluded that it is more difficult for the Fe to influence the structure of the MgO than the other way around. In the case where there is a GB

Table 6.1: Table showing E_f the formation energy (Jm^{-2}) for all interfaces and the average Fe-O bond length μ (Counted from the number of Fe-O bonds under 2.8 Å) (Å).

System	E_f	Type	μ Fe-O Bond
Fe(001)[100] || MgO(001)[110]	2.0	A	2.07
Fe(001)[100] || MgO(001)[100]	3.7	A	2.35
Fe(001)[310] || MgO(001)[110]	3.7	A	2.37
Fe(001)[100]/[110] || MgO(001)[110]	3.2	B	2.30
Fe(001)[100]/[110] || MgO(001)[100]	2.1	B	2.08
Fe(001)[310]/[$\bar{3}\bar{1}$0] || MgO(001)[100]	1.9	B	2.07
Fe(001)[100] || MgO(001)[110]/[100]	2.5	C	2.17
Fe(001)[110] || MgO(001)[110][100]	3	C	2.15
Fe(001)[100] || MgO(001)[210]/[$\bar{2}\bar{1}$0]	3.1	C	2.23
Fe(001)[110] || MgO(001)[210]/[$\bar{2}\bar{1}$0]	2.5	C	2.15
Fe(001)[100]/[110] || MgO(001)[110]/[100]	1.6	D	2.07
Fe(001)[310]/[$\bar{3}\bar{1}$0] \|\| MgO(001)[210]/[$\bar{2}\bar{1}$0]	1.8	D	2.13

in the substrate and a bulk film it will be energetically unfavourable for a GB to form within the film. But for type B interfaces Fe is very likely to undergo some structural reconstruction to accommodate the MgO.

6.3.1 Comparison to experiment

Type B and Type C interfaces are those where part or all of the Fe/MgO interface does not lattice match. It was found that interfaces Fe(001)[100] \|\| MgO(001)[110]/[100] and Fe(001)[110] \|\| MgO(001)[210]/[$\bar{2}\bar{1}$0] were stable and thus in theory could appear in MTJs. It is possible using TEM image simulations to understand what this may look like if they were to appear in the TEM images, in other words what the TEM images would look like if the atomic columns were not in registry. To explore this further TEM image simulations were performed by our collaborator Mitsuhiro Saito on the Fe(001)[100] \|\| MgO(001)[110]/[100] interface. The TEM image simulations are shown in Fig. 6.15. From analysing the all of the TEM images of the MgO film (shown in Figs. 5.4 - 5.6) no images which look similar to the pattern in Fig. 6.15 have been observed. This gives us confidence that type B and C interfaces are unlikely to be present in MTJs. To give conclusive proof that type B and C interfaces are unphysical EELS experiments need to be performed to check the chemical composition of the MgO films.
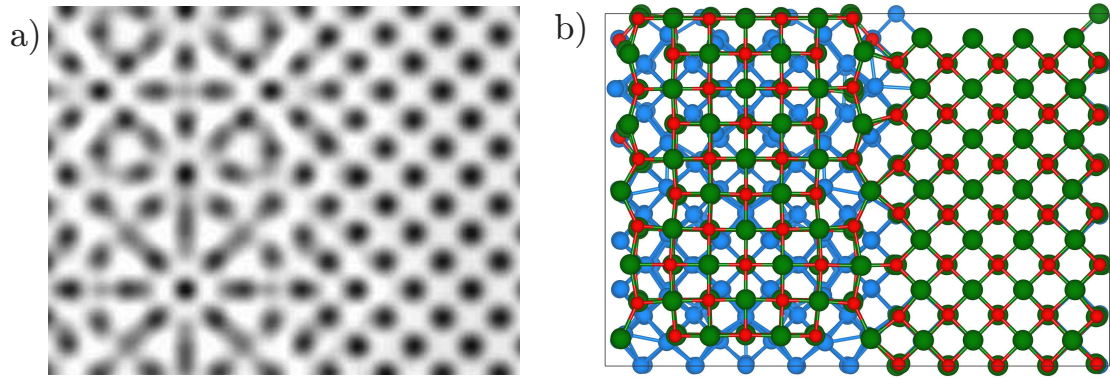
Figure 6.15: Comparison between transmission electron microscopy image simulations and theoretical models. a) A Fe(001)[100] || MgO(001)[110]/[100] interface transmission electron microscopy image simulation
b) A Fe(001)[100] || MgO(001)[110]/[100] interface theoretical model viewed from above.

6.4 Discussion

Computational power restricts the total number of initial conditions and the total number of atoms which can feasibly investigated when modelling large superstructures. This means that interface structures which have been considered only contain 4 layers of MgO and 6 layers of Fe (in some cases 6 layers of MgO and 6 layers of Fe). As GBs can become unstable at the surfaces multilayer systems are considered. Multilayer systems contain two interfaces between Fe and MgO with no vacuum gap. Upon initial inspection it may not have been prudent to construct certain supercells with a larger number of atoms in MgO for the STGBs but looking at the convergence of the formation energy with thickness there is only a difference of around 0.1 Jm^{-2} which should not significantly affect the conclusions drawn from the results.

There is a lattice mismatch of approximately 6% between the bulk optimised lattices of Fe and MgO in DFT. In this study the supercells have had the strain of MgO and Fe combined resulting in an effective strain of around 3% in each materials. In Fe the strain is tensile while in MgO the strain is compressive. From analysis of TEM images there are many epitaxial interfaces present which are in good agreement with computational models used in this chapter [17]. In real devices such a strain can result in the appearance of dislocations which have been observed experimentally [53,54]. It is possible to estimate the dislocation density from the strain which is approximately 1 per 7nm. Supercells

which are 7nm (70 Å) would be prohibitively large for DFT calculations. It may be possible to complement the DFT results by using classical interatomic potentials to model supercells on the nanometre scale. Dislocations in Fe and MgO could be studied in isolation and simple Lennard-Jones potential could be parameterised to describe the interaction between Fe and MgO. Such potential models would give some insight into how dislocations are manifested in these systems.

In all the systems explored in this chapter the strain is equally balanced between the Fe and the MgO however in real systems as MgO possesses both a large bond strength and bulk modulus most of the strain is likely to be on the Fe. Without performing computationally expensive full cell relaxations on these large systems it is difficult to determine the effect of differing degrees of strain on these systems.

The best performing MTJs (in terms of the TMR) use FeCoB as the electrode material. Modelling boron is generally not required due to its relative instability in bulk FeCo and Fe. In any case, studies have shown that boron segregates into the Ta which is not an active part of the device. Boron diffusion is not well understood but will be explored computationally in work following this thesis. Considering FeCo as the electrode material is possible but would significantly increase the computational complexity as the configurational degrees of freedom may be important. Different concentrations of Fe and Co may change the behaviour of the materials and would need to be studied. However many studies have shown that the use of different electrode materials such as Fe, Co and FeCo does not significantly change the behaviour of MTJs. Thus using Fe alone is a good approximation when modelling MTJs.

It was not possible to optimise the interfaces in the direction normal to the interfaces due to the computational complexity. Thus all the interface systems include an additional interface strain energy which is present from the repulsive forces from the interface. Unphysical interfaces are likely to posses an interface strain which will give rise to higher interface strain energies than more stable interfaces. It could be that the contribution in energy from the strain is extenuated in certain circumstances. At worst the interface strain was found to be 5% in either crystal. As the strains in the other directions due to the lattice matching differences between Fe and MgO are comparable this is unlikely to add significant artefacts to the results.

6.5 Conclusions

TEM images of FeCoB/MgO/FeCoB MTJs have revealed the polycrystallinity of the MgO layer [18]. However the orientational relationship between the FeCoB and MgO is not fully understood and cannot be easily observed experimentally. In this chapter first principles calculations were performed to gain insight into the orientation relationship between the Fe substrate and MgO film.

It is found that MgO is more likely to retain its structure in the presence of Fe with the possibility of Fe undergoing quite strong structural relaxations in order to accommodate MgO. The lack of structural relaxation of the MgO is likely due to the strong bonds between Mg-O (3.71 eV) relative to the weak bonds of Fe-Fe (1.22 eV). Epitaxial interfaces between Fe and MgO posses the lowest formation energies; such interfaces include type A and type D as defined in the methods (see Sec. 6.1). While type C interfaces may exist, type B interfaces are extremely unfavourable. It can be inferred from experiments performed by our collaborators in Japan that type B and type C interfaces are unlikely to occur in devices as they would cause a dispersion of the electron beam at the focus point resulting in blurred image. Instead well ordered atomic columns are observed suggesting an epitaxial relationship. Further experiments such as EELS could confirm or deny the possibility of type B and C interfaces via the detection of Fe in the MgO plan-view samples which were investigated in chapter 5. If Fe is present the clear atomic columns suggest that other orientational relationships between the Fe and MgO do not occur experimentally.

The average Fe-O bond length seems to be the main factor behind a strong adhesion (low formation energy) between Fe and MgO. The bond density of close Fe-O bonds appears to be negatively correlated with interface formation energy. From the results and analysis in this chapter it is predicted that after the annealing process when creating MTJs the FeCoB will have a grain size roughly greater or equal to that of the MgO as deposited (>10 - 15nm). This may mean that the GBs in the MgO as deposited will largely control the TMR in devices.

Further investigation of the properties of point defects in such systems such as oxygen vacancies and boron interstitials will make for an interesting additional study. Point defects can cause additional gap states which may further weaken the insulating properties of MgO. Segregation of Ta or B to the GBs of MgO or FeCo could be proven to

be significant in MTJs.

Chapter 7

Conclusions

In this thesis computational techniques have been employed to model polycrystalline materials. GB models have been constructed for a wide range of different systems including metals, metal-oxides and a combination of the two. Experimental techniques performed by collaborators and other researchers have been used as a benchmark to validate models, form predictions and describe experiments. It has been explicitly argued and evidenced that the combination of experiment, pen and paper theory, and computer modelling is a powerful trinity in materials physics. Although the focus has mainly been on MTJs many of the techniques can be applied to other systems and devices.

The excess volume associated with GBs has been discussed in detail. It was found that there are often large discrepancies between the excess volumes of different materials even though their lattice constants are very similar. The origin of the excess volume differences lies in the different bulk moduli of the materials in question and how the structural relaxations are localised around the interfaces.

The work on excess volume in metals has already had some effect on the field as already five non-self citations have been gathered from the first piece of published work [88]. One of the interesting follow up studies has highlighted the idea of negative excess volume [271]. A negative excess volume may mean that a material can more strongly reject segregation and embrittlement which would be an extremely useful material for use in nuclear reactors. A negative excess volume for a STGB was found in this PhD when investigating the material tungsten (bcc crystal structure). The idea of negative excess volume requires significantly more work to understand. Direct experimental observations of the excess volume in tungsten would prove or disprove the hypothesis of negative excess volume studied in the paper.

Another study has used standard results re-iterated in this work including the equations which determine the formation energy and excess volume of GBs [272]. In another paper the authors produced a sample crystal of nickel which contains different types of GBs in different directions. This so called anisotropic crystal has different mechanical properties depending on the orientation [273]. Our paper also has been cited as a source showing that there is a relationship between segregation and excess volume [274]. Our work did not do this explicitly but is implicit to the idea of excess volume and is highly intuitive. Finally a subject review on the methodologies described on the construction of GBs has been undertaken by Vitek et. al. [275]. In Vitek's work they expand on the structural unit model for GBs by adding GBs which are in metastable configurations to predict the energies of [001] and [111] tilt GBs in tungsten without performing many atomistic simulations. Further to direct scientific communication an ambitious art project around the theme of imperfection has been initiated. The idea here is to exhibit the ideas of polycrystallinity to the general public via the use of similar approaches to Atomix (see Fig. 1.3). I am currently building an extremely large version of Atomix and other installations in this regard.

The electronic properties of the metal-oxide MgO has been investigated by looking at plan-view TEM images of MgO thin films which have had the adjacent materials filed away. The plan view images are the first of their kind for imaging the MgO layer within MTJs. It was found that it is possible for GBs which would normally be ignored on the grounds of energetic instability to be present in MTJs. These ATGBs have been found to posses a significantly reduced band gap at the interface. A reduced band gap may have the effect of reducing the tunnelling magneto-resistance in these devices by creating short circuit tunnelling paths through the material. Passivating these GBs may seek to improve the resistance properties of the films. No papers have yet cited my second paper since it was only recently published (04.04.17) [18].

Knowledge from the first two results chapters (4 & 5) have been brought together to study the relationship between the metal Fe and MgO in an interface stack structure. It is found that only certain configurations of interfaces are energetically stable with many others containing too much strain or an extremely high formation energy. It is also found that it is possible for Fe to undergo significant structural reconstructions to accommodate the oxide film. It can be predicted that during the crystallisation process of the FeCoB it is likely that any GBs which form in the FeCo will be in registry with

136

GBs which already exist in the MgO film as deposited. It is further predicted that the grain size of the Fe in this structure is likely to be comparable to the MgO (10-15 nm). The calculations performed in chapter 6 are the first of their kind involving GBs within the Fe and MgO layers. The new mathematical notation which has been defined in chapter 6 could come in useful when characterising stack structures. It allows for an extremely easy method for describing a complex stack structure and the associated GBs.

There are many possible avenues for future work following results gathered in this thesis. One idea is to further study the magnetic properties of Fe/MgO interfaces. Calculations will be performed to understand the dynamics of the spins in the complex interfaces studied in chapter 6. Another idea is to study the effect of point defects within MgO thin films studied in chapter 5. The third idea is to perform transport calculations on some of the Fe/MgO systems explored in chapter 6. Such calculations would allow the computation of the magnetoresistance for these systems. If computationally feasible the results would give real-space images of where the current flows via the bond currents and/or eigenchannel scattering states. The forth idea is to systematically study the excess volume for more metals to attempt to show the trends of the periodic table, this could be further expanded to binary compounds. Calculations performed during this PhD have begun to show the effect of point defects in MgO. It was predicted that the passivating MgO GBs with group 7 elements such as Cl could restore the insulating properties of the MgO in a similar way that B and Hf are used to strengthen GBs in metals. A final idea is to attempt to understand the relationship between the excess volume and the degree of segregation which can occur in materials. Although implicitly the degree of segregation has been calculated for many materials the relationship between excess volume has not been explicitly studied.

While the field of polycrystalline materials is quite well developed there are still many more experiments and calculations which are required to understand both poly-crystallinity in general and MTJs. Specifically probing buried devices for the presence of GBs, point defects and structural phase transitions remains extremely difficult. Computational techniques are still undergoing development and many systems still can only be reliably explored at the quantum level (this of course limits the number of atoms that can be studied). In addition the vast phase space of thermodynamic effects, dislocations and many more still lack a complete understanding. The development of new methods to describe the interatomic interactions which are more accurate and faster than

current methods, time dependent DFT to study transport properties for large systems and exaflops computing are areas which are likely to catalyse scientific and industrial progress.

New discoveries are being made everyday as researchers push computational and experimental techniques further. One does predict and hope the formation of a singularity of knowledge in material science with the advent of quantum computation.

Abbreviations

ATGB Asymmetric tilt grain boundary.

CG Conjugate gradients.

COMB Charge optimised many body.

DFT Density functional theory.

EAM Embedded atom method.

EELS Electron energy loss spectroscopy.

GB Grain boundary.

GGA Generalized gradient approximation.

HF Hartree-Fock.

HSE Heyd, Scuseria and Ernzerhof.

LDA Local density approximation.

LSD Local spin density approximation.

MP Monkhorst-Pack.

MRAM Magnetic random access memory.

MTJ Magnetic tunnel junction.

PBC Periodic boundary conditions.

PBE Perdew, Burke and Ernzerhof.

SEM Scanning electron microscopy.

STEM Scanning transmission electron microscopy.

STGB Symmetric tilt grain boundary.

STM Scanning tunnelling electron microscopy.

SU Structural unit.

TEM Transmission electron microscopy.

TMR Tunnelling magneto resistance.

Symbols

a: Lattice constant

(hkl): Miller indices describing a plane

$[mno]$: Miller indices describing a direction

δV: Excess volume

E_f: Formation energy

B_0: Bulk modulus

B': First pressure derivative of the bulk modulus

E_{coh}: Cohesive energy

γ_{hkl}: Surface energy of surface (hkl)

$\hat{\mathcal{H}}$: Hamiltonian

$n(r)$: Electronic density

F: Universal functional

E_{xc}: Exchange correlation functional

σ: Strain

$N\Sigma$: Σ value (CSL)

η: Difference in strains

Ω: Atomic volume (different for bcc and fcc)

A: Area

e: Charge of an electron

q: Charge

R: Resistance

G: Conductance

E_{tot}: Total energy

X: X stereographic coordinate

Y: Y stereographic coordinate

X': X' Lambert azimuthal projection coordinate

Y': Y' Lambert azimuthal projection coordinate

Bibliography

[1] "Nobel Prizes in Chemistry." `https://www.nobelprize.org/nobel_prizes/chemistry/laureates/`. Accessed: 2017-07-21.

[2] "Nobel Prizes in Physics." `https://www.nobelprize.org/nobel_prizes/physics/laureates/`. Accessed: 2017-07-21.

[3] "ONS R&D Spending." `https://www.ons.gov.uk/businessindustryandtrade/business/businessinnovation`. Accessed: 2017-07-21.

[4] "UK R&D Spending." `https://www.strategyand.pwc.com/uk/home/press_contacts/displays/2016-global-innovation1000-study-uk`. Accessed: 2017-07-21.

[5] "Global R&D Spending." `https://www.strategyand.pwc.com/innovation1000#GlobalKeyFindingsTabs3`. Accessed: 2017-07-21.

[6] S. R. Elliott, *Physics of amorphous materials*. Longman, 1984.

[7] E. O. Hall, "The Deformation and Ageing of Mild Steel: III Discussion of Results," *Proc. Phys. Soc. Sect. B*, vol. 64, no. 9, pp. 747–753, 1951.

[8] W. Sylwestrowicz and E. O. Hall, "The Deformation and Ageing of Mild Steel," *Proc. Phys. Soc. Sect. B*, vol. 64, no. 6, pp. 495–502, 1951.

[9] E. O. Hall, "The Deformation and Ageing of Mild Steel: II Characteristics of the Lüders Deformation," *Proc. Phys. Soc. Sect. B*, vol. 64, no. 9, pp. 742–747, 1951.

[10] N. J. Petch, "The cleavage strength of polycrystals," *J. Iron Steel Inst.*, vol. 174, pp. 25–28, 1953.

[11] C. E. Carlton and P. J. Ferreira, "What is behind the inverse Hall-Petch effect in nanocrystalline materials?," *Acta Mater.*, vol. 55, no. 11, pp. 3749–3756, 2007.

[12] A. R. Marder, "Metallurgy of zinc-coated steel," *Prog. Mater. Sci.*, vol. 45, no. 3, pp. 191–271, 2000.

[13] R. H. Nuttall, "The First Microscope of Henry Clifton Sorby," *Technol. Cult.*, vol. 22, no. 2, p. 275, 1981.

[14] W. H. Wilcockson, "The Geological Work Of Henry Clifton Sorby," *Proc. Yorksh. Geol. Soc.*, vol. 27, no. 1, pp. 1–22, 1947.

[15] P. D. Nellist, "Direct Sub-Angstrom Imaging of a Crystal Lattice," *Science*, vol. 305, no. 5691, pp. 1741–1741, 2004.

[16] Z. Wang, M. Saito, K. P. McKenna, L. Gu, S. Tsukimoto, A. L. Shluger, and Y. Ikuhara, "Atom-resolved imaging of ordered defect superstructures at individual grain boundaries," *Nature*, vol. 479, no. 7373, pp. 380–383, 2011.

[17] Z. Wang, M. Saito, K. P. McKenna, S. Fukami, H. Sato, S. Ikeda, H. Ohno, and Y. Ikuhara, "Atomic-Scale Structure and Local Chemistry of CoFeB-MgO Magnetic Tunnel Junctions," *Nano Lett.*, vol. 16, no. 3, pp. 1530–1536, 2016.

[18] J. J. Bean, M. Saito, S. Fukami, H. Sato, S. Ikeda, H. Ohno, Y. Ikuhara, and K. P. McKenna, "Atomic structure and electronic properties of MgO grain boundaries in tunnelling magnetoresistive devices," *Sci. Rep.*, vol. 7, no. January, p. 45594, 2017.

[19] P. D. Gorsuch, "On the crystal perfection of Iron whiskers," *J. Appl. Phys.*, vol. 30, no. 6, pp. 837–842, 1959.

[20] H. J. Dai, N. D'Souza, and H. B. Dong, "Grain Selection in Spiral Selectors During Investment Casting of Single-Crystal Turbine Blades: Part I. Experimental Investigation," *Metall. Mater. Trans. A*, vol. 42, no. 11, pp. 3430–3438, 2011.

[21] H. J. Dai, H. B. Dong, N. D'Souza, J.-C. Gebelin, and R. C. Reed, "Grain Selection in Spiral Selectors During Investment Casting of Single-Crystal Components: Part II. Numerical Modeling," *Metall. Mater. Trans. A*, vol. 42, no. 11, pp. 3439–3446, 2011.

[22] H. Bhadeshia, "Harry Bhadeshia On Space Elevators." `https://www.youtube.com/watch?v=y8VGQdBTVsA`. Accessed: 2017-07-21.

[23] D. Kalderon, "Steam Turbine Failure at Hinkley Point 'A'," *Proc. Inst. Mech. Eng.*, vol. 186, no. 1, pp. 341–377, 1972.

[24] M. P. Seah, "Grain boundary segregation and the T-t dependence of temper brittleness," *Acta Metall.*, vol. 25, pp. 345–357, 1977.

[25] P. Lejček and S. Hofmann, "Thermodynamics and structural aspects of grain boundary segregation," *Crit. Rev. Solid. State.*, vol. 20, no. 1, pp. 1–85, 1995.

[26] A. Y. Lozovoi, A. T. Paxton, and M. W. Finnis, "Structural and chemical embrittlement of grain boundaries by impurities: A general theory and first-principles calculations for copper," *Phys. Rev. B*, vol. 74, no. 15, p. 155416, 2006.

[27] K. Felkins, H. P. Leigh, and A. Jankovic, "The Royal Mail Ship Titanic: Did a Metallurgical Failure Cause a Night to Remember?," *Journal of the Minerals, Metals and Materials Society*, vol. 50, no. 1, pp. 12–18, 1998.

[28] T. Foecke, "Metallurgy of the RMS Titanic," *Metallurgy Division*, p. 18.

[29] M. S. Daw and M. I. Baskes, "Semiempirical, quantum mechanical calculation of hydrogen embrittlement in metals," *Phys. Rev. Lett.*, vol. 50, no. 17, pp. 1285–1288, 1983.

[30] M. W. Finnis and J. E. Sinclair, "A simple empirical n-body potential for transition metals," *Philos. Mag. A*, vol. 50, no. February 2014, pp. 45–55, 1984.

[31] G. Ackland, G. Tichy, V. Vitek, and M. Finnis, "Simple n-body potentials for the noble metals and nickel," *Philos. Mag. A*, vol. 56, no. 6, pp. 735–756, 1987.

[32] F. Cleri and V. Rosato, "Tight-binding potentials for transition metals and alloys," *Phys. Rev. B*, vol. 48, no. 1, pp. 22–33, 1993.

[33] A. P. Sutton and J. Chen, "Long-range finnis–sinclair potentials," *Philos. Mag. Lett.*, vol. 61, no. 3, pp. 139–146, 1990.

[34] G. J. Ackland, D. J. Bacon, A. F. Calder, and T. Harry, "Computer simulation of point defect properties in dilute FeCu alloy using a many-body interatomic potential," *Philos. Mag. A*, vol. 75, no. 3, pp. 713–732, 1997.

[35] T. Liang, T.-R. Shan, Y.-T. Cheng, B. D. Devine, M. Noordhoek, Y. Li, Z. Lu, S. R. Phillpot, and S. B. Sinnott, "Classical atomistic simulations of surfaces and heterogeneous interfaces with the charge-optimized many body (COMB) potentials," *Mater. Sci. Eng. R Rep.*, vol. 74, no. 9, pp. 255–279, 2013.

[36] K. Lejaeghere, G. Bihlmayer, T. Björkman, P. Blaha, S. Blügel, V. Blum, D. Caliste, I. E. Castelli, S. J. Clark, A. Dal Corso, S. de Gironcoli, T. Deutsch, J. K. Dewhurst, I. Di Marco, C. Draxl, M. Dułak, O. Eriksson, J. A. Flores-Livas, K. F. Garrity, L. Genovese, P. Giannozzi, M. Giantomassi, S. Goedecker, X. Gonze, O. Grånäs, E. K. U. Gross, A. Gulans, F. Gygi, D. R. Hamann, P. J. Hasnip, N. A. W. Holzwarth, D. Iuan, D. B. Jochym, F. Jollet, D. Jones, G. Kresse, K. Koepernik, E. Küçükbenli, Y. O. Kvashnin, I. L. M. Locht, S. Lubeck, M. Marsman, N. Marzari, U. Nitzsche, L. Nordström, T. Ozaki, L. Paulatto, C. J. Pickard, W. Poelmans, M. I. J. Probert, K. Refson, M. Richter, G.-M. Rignanese, S. Saha, M. Scheffler, M. Schlipf, K. Schwarz, S. Sharma, F. Tavazza, P. Thunström, A. Tkatchenko, M. Torrent, D. Vanderbilt, M. J. van Setten, V. Van Speybroeck, J. M. Wills, J. R. Yates, G.-X. Zhang, and S. Cottenier, "Reproducibility in density functional theory calculations of solids.," *Science*, vol. 351, no. 6280, p. aad3000, 2016.

[37] C.-K. Skylaris, "A benchmark for materials simulation," *Science*, vol. 351, no. 6280, pp. 1394–1395, 2016.

[38] T. Mütschele and R. Kirchheim, "Segregation and diffusion of hydrogen in grain boundaries of palladium," *Scr. Metall.*, vol. 21, no. c, pp. 135–140, 1987.

[39] A. Mayadas and M. Shatzkes, "Electrical-resistivity model for polycrystalline films: the case of arbitrary reflection at external surfaces," *Phy. Rev. B*, vol. 1, no. 4, p. 1382, 1970.

[40] J. P. Hirth, "The Influence of Grain Boundaries," *Metall. Trans.*, vol. 3, no. 12, pp. 3047–3067, 1972.

[41] C. T. Liu, C. L. White, and J. A. Horton, "Effect of boron on grain-boundaries in Ni3Al," *Acta Metall.*, vol. 33, no. 2, pp. 213–229, 1985.

[42] E.-M. Steyskal, B. Oberdorfer, W. Sprengel, M. Zehetbauer, R. Pippan, and R. Würschum, "Direct Experimental Determination of Grain Boundary Excess Volume in Metals," *Phys. Rev. Lett.*, vol. 108, no. 5, p. 055504, 2012.

[43] B. Oberdorfer, D. Setman, E.-M. Steyskal, A. Hohenwarter, W. Sprengel, M. Zehetbauer, R. Pippan, and R. Würschum, "Grain boundary excess volume and defect annealing of copper after high-pressure torsion," *Acta Mater.*, vol. 68, no. 100, pp. 189–195, 2014.

[44] D. Wolf, "Correlation between the energy and structure of grain boundaries in b.c.c. metals I. Symmetrical boundaries on the (110) and (100) planes," *Philos. Mag. Part B*, vol. 59, no. 6, pp. 667–680, 1989.

[45] S. S. P. Parkin, K. P. Roche, M. G. Samant, P. M. Rice, R. B. Beyers, R. E. Scheuerlein, E. J. O'Sullivan, S. L. Brown, J. Bucchigano, D. W. Abraham, Y. Lu, M. Rooks, P. L. Trouilloud, R. a. Wanner, and W. J. Gallagher, "Exchange-biased magnetic tunnel junctions and application to nonvolatile magnetic random access memory (invited)," *J. Appl. Phys.*, vol. 85, no. 8, pp. 5828–5833, 1999.

[46] S. Tehrani, J. M. Slaughter, E. Chen, M. Durlam, J. Shi, and M. Deherrera, "Progress and outlook for mram technology," *IEEE Trans. Magn.*, vol. 35, no. 5 PART 1, pp. 2814–2819, 1999.

[47] E. Y. Tsymbal, O. N. Mryasov, and P. R. LeClair, "Spin-dependent tunnelling in magnetic tunnel junctions," *J. Phys. Condens. Matter.*, vol. 15, no. 4, pp. R109–R142, 2003.

[48] X. Dong, X. Wu, G. Sun, Y. Xie, H. Li, and Y. Chen, "Circuit and microarchitecture evaluation of 3D stacking magnetic RAM (MRAM) as a universal memory replacement," *Proceedings - Design Automation Conference*, pp. 554–559, 2008.

[49] W. H. Butler, "Tunneling magnetoresistance from a symmetry filtering effect," *Sci. Technol. Adv. Mater.*, vol. 9, no. 1, p. 014106, 2008.

147

[50] J. Zhu and C. Park, "Magnetic tunnel junctions," *Mater. Today*, vol. 9, no. 11, pp. 36–45, 2006.

[51] M. Julliere, "Tunneling between ferromagnetic films," *Physics Letters A*, vol. 54, no. 3, pp. 225–226, 1975.

[52] S. Van Dijken, X. Jiang, and S. S. P. Parkin, "Room temperature operation of a high output current magnetic tunnel transistor," *Appl. Phys. Lett.*, vol. 80, no. 18, pp. 3364–3366, 2002.

[53] S. S. P. Parkin, C. Kaiser, A. Panchula, P. M. Rice, B. Hughes, M. Samant, and S.-H. Yang, "Giant tunnelling magnetoresistance at room temperature with MgO (100) tunnel barriers," *Nat. Mater.*, vol. 3, no. 12, pp. 862–867, 2004.

[54] S. Yuasa, T. Nagahama, A. Fukushima, Y. Suzuki, and K. Ando, "Giant room-temperature magnetoresistance in single-crystal Fe/MgO/Fe magnetic tunnel junctions," *Nat. Mater.*, vol. 3, no. 12, pp. 868–871, 2004.

[55] X. G. Zhang and W. H. Butler, "Large magnetoresistance in bcc Co/MgO/Co and FeCo/MgO/FeCo tunnel junctions," *Phys. Rev. B*, vol. 70, pp. 1–4, 2004.

[56] S. Ikeda, J. Hayakawa, Y. Ashizawa, Y. M. Lee, K. Miura, H. Hasegawa, M. Tsunoda, F. Matsukura, and H. Ohno, "Tunnel magnetoresistance of 604% at 300 K by suppression of Ta diffusion in CoFeBMgOCoFeB pseudo-spin-valves annealed at high temperature," *Appl. Phys. Lett.*, vol. 93, no. 8, pp. 39–42, 2008.

[57] J.-B. Michel, Y. K. Shen, A. P. Aiden, A. Veres, M. K. Gray, J. P. Pickett, D. Hoiberg, D. Clancy, P. Norvig, J. Orwant, S. Pinker, M. A. Nowak, and E. L. Aiden, "Quantitative Analysis of Culture Using Millions of Digitized Books," *Science*, vol. 331, no. 6014, pp. 176–182, 2011.

[58] R. Archer, "Development of grain boundaries in heat treated alloy steels," *Trans. Amer. Inst. Métal. Eng*, vol. 62, pp. 754–760, 1920.

[59] R. Miller, "Influence of a grain boundary on the deformation of a single crystal of zinc," *Trans. AIME*, vol. 111, p. 135, 1934.

[60] C. Zener, "Theory of the elasticity of polycrystals with viscous grain boundaries," *Phys. Rev.*, vol. 60, no. 12, p. 906, 1941.

[61] N. Mott, "Slip at grain boundaries and grain growth in metals," *Proc. of the Phys. Soc.*, vol. 60, no. 4, p. 391, 1948.

[62] S. Benedetti, P. Myrach, A. Di Bona, S. Valeri, N. Nilius, and H. J. Freund, "Growth and morphology of metal particles on MgO/Mo(001): A comparative STM and diffraction study," *Phys. Rev. B*, vol. 83, no. 12, pp. 1–10, 2011.

[63] A. P. Sutton and R. W. Balluffi, *Interfaces in crystalline materials.* Clarendon Press, 1995.

[64] N. W. Ashcroft and N. D. Mermin, "Introduction to solid state physics," *Saunders, Philadelphia*, 1976.

[65] D. Wolf, "On the Energy of $< 100 >$ Coincidence Twist Boundaries in Transition Metal Oxides," *Le Journal de Physique Colloques*, vol. 41, no. C6, pp. C6–142–C6–145, 1980.

[66] D. M. Duffy and P. W. Tasker, "A General Structure for Coincidence Twist Grain Boundaries in Rock-Salt-Structured Oxides," *Journal of the American Ceramic Society*, vol. 67, no. 9, pp. C–176–C–177, 1984.

[67] D. C. Sayle, T. X. T. Sayle, S. C. Parker, J. H. Harding, and C. R. A. Catlow, "The stability of defects in the ceramic interfaces, MgO/MgO and CeO_2/Al_2O_3," *Surf. Sci.*, vol. 334, no. 1-3, pp. 170–178, 1995.

[68] S. Von Alfthan, P. D. Haynes, K. Kaski, and A. P. Sutton, "Are the structures of twist grain boundaries in silicon ordered at 0 K?," *Phys. Rev. Lett.*, vol. 96, no. 5, p. 055505, 2006.

[69] N. A. Benedek, A. L. S. Chua, C. Elsässer, A. P. Sutton, and M. W. Finnis, "Interatomic potentials for strontium titanate: An assessment of their transferability and comparison with density functional theory," *Physical Review B - Condensed Matter and Materials Physics*, vol. 78, no. 6, pp. 1–13, 2008.

[70] M. R. Hestenes and E. Stiefel, "Method of conjugate gradients for solving linear systems," *J. Res. Nat. Bur. Stand.*, vol. 49, no. 6, pp. 409–436, 1952.

[71] E. A. Holm, D. L. Olmsted, and S. M. Foiles, "Comparing grain boundary energies in face-centered cubic metals: Al, Au, Cu and Ni," *Scr. Mater.*, vol. 63, no. 9, pp. 905–908, 2010.

[72] S. Ratanaphan, D. L. Olmsted, V. V. Bulatov, E. A. Holm, A. D. Rollett, and G. S. Rohrer, "Grain boundary energies in body-centered cubic metals," *Acta Mater.*, vol. 88, pp. 346–354, 2015.

[73] S. Ranganathan, "On the geometry of coincidence-site lattices," *Acta Crystallogr.*, vol. 21, no. 2, pp. 197–199, 1966.

[74] G. W. Watson, E. T. Kelsey, N. H. de Leeuw, D. J. Harris, and S. C. Parker, "Atomistic simulation of dislocations, surfaces and interfaces in MgO," *Journal of the Chemical Society, Faraday Transactions*, vol. 92, no. 3, p. 433, 1996.

[75] H. Aaron and G. Bolling, "Free volume as a criterion for grain boundary models," *Surf. Sci.*, vol. 31, pp. 27–49, 1972.

[76] R. I. Masel, *Principles of adsorption and reaction on solid surfaces*, vol. 3. John Wiley & Sons, 1996.

[77] J. Snyder, *Map Projections—A Working Manual.* U.S. Geological Survey professional paper, 1987.

[78] W. T. Read and W. Shockley, "Dislocation models of crystl grain boundaries," *Phys. Rev.*, vol. 78, pp. 275–289, 1950.

[79] D. Brandon, "The structure of high-angle grain boundaries," *Acta Metall.*, vol. 14, no. 11, pp. 1479–1484, 1966.

[80] S. Darby, T. V. Mortimer-Jones, R. L. Johnston, and C. Roberts, "Theoretical study of CuAu nanoalloy clusters using a genetic algorithm," *J. Chem. Phys.*, vol. 116, no. 4, pp. 1536–1550, 2002.

[81] J.-Y. Yi, D. J. Oh, and J. Bernholc, "Structural distortions in metal clusters," *Phys. Rev. Lett.*, vol. 67, no. 12, pp. 1594–1597, 1991.

[82] K. Michaelian, N. Rendón, and I. L. Garzón, "Structure and energetics of Ni, Ag, and Au nanoclusters," *Phys. Rev. B*, vol. 60, no. 3, pp. 2000–2010, 1999.

[83] C. Woodward, B. I. Min, R. Benedek, and J. Garner, "Electronic-structure calculation for metals by local optimization," *Phys. Rev. B*, vol. 39, no. 8, pp. 4853–4861, 1989.

[84] D. Wolf, "Correlation between the energy and structure of grain boundaries in b.c.c. metals. II. Symmetrical tilt boundaries," *Philos. Mag. A*, vol. 62, no. 4, pp. 447–464, 1990.

[85] J. Rittner and D. Seidman, "$\langle 110 \rangle$ Symmetric Tilt Grain-Boundary Structures in Fcc Metals With Low Stacking-Fault Energies," *Phys. Rev. B*, vol. 54, no. 10, pp. 6999–7015, 1996.

[86] D. Spearot, M. Tschopp, K. Jacob, and D. Mcdowell, "Tensile strength of $\langle 100 \rangle$ and $\langle 110 \rangle$ tilt bicrystal copper interfaces," *Acta Mater.*, vol. 55, no. 2, pp. 705–714, 2007.

[87] S. Ogata, H. Kitagawa, Y. Maegawa, and K. Saitoh, "Ab-initio analysis of aluminum $\Sigma = 5$ grain boundaries - fundamental structures and effects of silicon impurity," *Comput. Mater. Sci.*, vol. 7, no. 3, pp. 271–278, 1997.

[88] J. Bean and K. McKenna, "Origin of differences in the excess volume of copper and nickel grain boundaries," *Acta Mater.*, vol. 110, pp. 246–257, 2016.

[89] M. S. Daw, S. M. Foiles, and M. I. Baskes, "The embedded-atom method: a review of theory and applications," *Mater. Sci. Reports*, vol. 9, no. 7, pp. 251–310, 1993.

[90] R. Wu, A. J. Freeman, and G. B. Olson, "First principles determination of the effects of phosphorus and boron on iron grain boundary cohesion.," *Science*, vol. 265, no. 5170, pp. 376–80, 1994.

[91] I. Dawson, P. P. Bristowe, M. M.-H. M. M.-H. Lee, M. Payne, J. White, and M. Segall, "First-principles study of a tilt grain boundary in rutile," *Phys. Rev. B*, vol. 54, no. 19, pp. 13727–13733, 1996.

[92] R. J. Kurtz and H. L. Heinisch, "The effects of grain boundary structure on binding of He in Fe," *J. Nucl. Mater.*, vol. 329-333, pp. 1199–1203, 2004.

[93] K. P. McKenna, F. Hofer, D. Gilks, V. K. Lazarov, C. Chen, Z. Wang, and Y. Ikuhara, "Atomic-scale structure and properties of highly stable antiphase boundary defects in Fe_3O_4," *Nat. Commun.*, vol. 5, p. 5740, 2014.

[94] J. A. Moriarty, J. F. Belak, R. E. Rudd, P. Söderlind, F. H. Streitz, and L. H. Yang, "Quantum-based atomistic simulation of materials properties in transition metals," *J. Phys. Condens. Matter*, vol. 14, no. 11, pp. 2825–2857, 2002.

[95] M. A. Tschopp, G. J. Tucker, and D. L. McDowell, "Structure and free volume of $\langle 110 \rangle$ symmetric tilt grain boundaries with the E structural unit," *Acta Mater.*, vol. 55, no. 11, pp. 3959–3969, 2007.

[96] Y. Mishin, M. Asta, and J. Li, "Atomistic modeling of interfaces and their impact on microstructure and properties," *Acta Mater.*, vol. 58, no. 4, pp. 1117–1151, 2010.

[97] D. Bouchet and L. Priester, "Grain boundary plane and intergranular segregation in nickel-sulfur system," *Scr. Metall.*, vol. 21, no. 4, pp. 475–478, 1987.

[98] Y. Kuru, M. Wohlschlögel, U. Welzel, and E. J. Mittemeijer, "Large excess volume in grain boundaries of stressed, nanocrystalline metallic thin films: Its effect on grain-growth kinetics," *Appl. Phys. Lett.*, vol. 95, no. 16, p. 163112, 2009.

[99] L. Zhang, X. Shu, S. Jin, Y. Zhang, and G.-h. Lu, "First-principles study of He effects in a bcc Fe grain boundary: site preference, segregation and theoretical tensile strength.," *J. Phys. Condens. Matter*, vol. 22, no. 37, p. 375401, 2010.

[100] L. Zhang, C. C. Fu, and G. H. Lu, "Energetic landscape and diffusion of He in α-Fe grain boundaries from first principles," *Phys. Rev. B*, vol. 87, pp. 1–11, 2013.

[101] W.-T. Geng, A. J. Freeman, G. B. Olson, Y. Tateyama, and T. Ohno, "Hydrogen-Promoted Grain Boundary Embrittlement and Vacancy Activity in Metals: Insights from Ab Initio Total Energy Calculatons," *Mater. Trans.*, vol. 46, no. 4, pp. 756–760, 2005.

[102] M. Yamaguchi, K. I. Ebihara, M. Itakura, T. Kadoyoshi, T. Suzudo, and H. Kaburaki, "First-principles study on the grain boundary embrittlement of metals by solute segregation: Part II. metal (Fe, Al, Cu)-hydrogen (H) systems," *Metall. Mater. Trans. A Phys. Metall. Mater. Sci.*, vol. 42, no. 2, pp. 330–339, 2011.

[103] K. N. Solanki, M. A. Tschopp, M. A. Bhatia, and N. R. Rhodes, "Atomistic investigation of the role of grain boundary structure on hydrogen segregation and embrittlement in α-Fe," *Metall. Mater. Trans. A Phys. Metall. Mater. Sci.*, vol. 44, no. 3, pp. 1365–1375, 2013.

[104] T. Suzudo, M. Yamaguchi, and T. Tsuru, "Atomistic modeling of He embrittlement at grain boundaries of α -Fe: a common feature over different grain boundaries," *Model. Simul. Mater. Sci. Eng.*, vol. 21, no. 8, p. 085013, 2013.

[105] N. Baluc, R. Schäublin, P. Spätig, and M. Victoria, "On the potentiality of using ferritic/martensitic steels as structural materials for fusion reactors," *Nucl. Fusion*, vol. 44, no. 1, pp. 56–61, 2003.

[106] V. Chernov, M. Leonteva-Smirnova, M. Potapenko, N. Budylkin, Y. Devyatko, A. Ioltoukhovskiy, E. Mironova, A. Shikov, A. Sivak, G. Yermolaev, A. Kalashnikov, B. Kuteev, A. Blokhin, N. Loginov, V. Romanov, V. Belyakov, I. Kirillov, T. Bulanova, V. Golovanov, V. Shamardin, Y. Strebkov, A. Tyumentsev, B. Kardashev, O. Mishin, and B. Vasiliev, "Structural materials for fusion power reactorsthe RF R&D activities," *Nucl. Fusion*, vol. 47, no. 8, pp. 839–848, 2007.

[107] A. D. L. Claire, "The analysis of grain boundary diffusion measurements," *Br. J. Appl. Phys.*, vol. 14, no. 6, pp. 351–356, 1963.

[108] M. A. Meyers, A. Mishra, D. J. Benson, Meyers M.A., Mishra A., and B. D.J., "Mechanical properties of nanocrystalline materials," *Prog. Mater. Sci.*, vol. 51, no. 4, pp. 427–556, 2006.

[109] L. Priester, *Grain boundaries: from theory to engineering*, vol. 172. Springer Science & Business Media, 2012.

[110] L. Reimer, *Transmission electron microscopy: physics of image formation and microanalysis*, vol. 36. Springer, 2013.

[111] Y. Ivanisenko, R. Z. Valiev, and H. J. Fecht, "Grain boundary statistics in nano-structured iron produced by high pressure torsion," *Mater. Sci. Eng. A*, vol. 390, no. 1-2, pp. 159–165, 2005.

[112] X. Molodova, A. Khorashadizadeh, G. Gottstein, M. Winning, and R. J. Hellmig, "Thermal stability of ECAP processed pure Cu and CuZr," *Int. J. Mater. Res.*, vol. 98, pp. 269–275, 2007.

[113] C. Schmidt, M. W. Finnis, F. Ernst, and V. Vitek, "Theoretical and experimental investigations of structures and energies of $\Sigma = 3$, [112] tilt grain boundaries in copper," *Philos. Mag. A*, vol. 77, no. 5, pp. 1161–1184, 1998.

[114] O. H. Duparc, S. Poulat, A. Larere, J. Thibault, and L. Priester, "High-resolution transmission electron microscopy observations and atomic simulations of the structures of exact and near $\Sigma = 11$, {332} tilt grain boundaries in nickel," *Philos. Mag. A*, vol. 80, no. 4, pp. 853–870, 2000.

[115] D. A. Muller, "Structure and bonding at the atomic scale by scanning transmission electron microscopy," *Nat. Mater.*, vol. 8, no. 4, pp. 263–270, 2009.

[116] V. Randle, G. S. Rohrer, H. M. Miller, M. Coleman, and G. T. Owen, "Five-parameter grain boundary distribution of commercially grain boundary engineered nickel and copper," *Acta Mater.*, vol. 56, no. 10, pp. 2363–2373, 2008.

[117] J. Li, S. J. Dillon, and G. S. Rohrer, "Relative grain boundary area and energy distributions in nickel," *Acta Mater.*, vol. 57, no. 14, pp. 4304–4311, 2009.

[118] H. Beladi and G. S. Rohrer, "The distribution of grain boundary planes in interstitial free steel," *Metall. Mater. Trans. A Phys. Metall. Mater. Sci.*, vol. 44, no. 1, pp. 115–124, 2013.

[119] H. W. Fuller and M. E. Hale, "Determination of magnetization distribution in thin films using electron microscopy," *J. Appl. Phys.*, vol. 31, no. 2, pp. 238–248, 1960.

[120] J. Stöhr, "X-ray magnetic circular dichroism spectroscopy of transition metal thin films," *J. Electron Spectros. Relat. Phenomena*, vol. 75, no. C, pp. 253–272, 1995.

[121] P. Schattschneider, S. Rubino, M. Stoeger-Pollach, C. Hbert, J. Rusz, L. Calmels, and E. Snoeck, "Energy loss magnetic chiral dichroism: A new technique for the study of magnetic properties in the electron microscope (invited)," *J. Appl. Phys.*, vol. 103, no. 7, 2008.

[122] M. P. Seah and E. D. Hondros, "Grain Boundary Segregation," *Proc. R. Soc. A Math. Phys. Eng. Sci.*, vol. 335, no. 1601, pp. 191–212, 1973.

[123] N. Gokon and M. Kajihara, "Occurrence of Faceting for [110] Symmetric Tilt Boundaries in Cu Doped with Bi," *Mater. Trans.*, vol. 49, no. 11, pp. 2584–2590, 2008.

[124] A. Atkinson and R. I. Taylor, "Ni along grain boundaries in nickel oxide," *Philos. Mag. A*, vol. 43, no. 4, pp. 979–998, 1981.

[125] E. Budke, T. Surholt, S. Prokofjev, L. Shvindlerman, and C. Herzig, "Tracer diffusion of Au and Cu in a series of near Σ=5 (310)[001] symmetrical Cu tilt grain boundaries," *Acta Mater.*, vol. 47, no. 2, pp. 385–395, 1999.

[126] H. L. Tuller, "Ionic conduction in nanocrystalline materials," *Solid State Ionics*, vol. 131, pp. 143–157, 2000.

[127] Y. R. Kolobov, A. G. Lipnitskii, I. V. Nelasov, and G. P. Grabovetskaya, "Investigations and computer simulations of the intergrain diffusion in submicro-and nanocrystalline metals," *Russ. Phys. J.*, vol. 51, no. 4, pp. 385–399, 2008.

[128] M. I. Buckett and K. L. Merkle, "Determination of grain boundary volume expansion by HREM," *Ultramicroscopy*, vol. 56, no. 1-3, pp. 71–78, 1994.

[129] U. Dahmen, S. Paciornik, I. G. Solorzano, and J. B. Vandersande, "HREM analysis of structure and defects in a Σ5 (210) grain boundary in rutile," *Interface Sci.*, vol. 2, pp. 125–136, 1994.

[130] B. Lamprecht, J. R. Krenn, G. Schider, H. Ditlbacher, M. Salerno, N. Felidj, A. Leitner, F. R. Aussenegg, and J. C. Weeber, "Surface plasmon propagation in microscale metal stripes," *Appl. Phys. Lett.*, vol. 79, no. 1, pp. 51–53, 2001.

[131] S.-H. Chang, S. K. Gray, and G. C. Schatz, "Surface plasmon generation and light transmission by isolated nanoholes and arrays of nanoholes in thin metal films," *Opt. Express*, vol. 13, no. 8, p. 3150, 2005.

[132] R. A. Catlow, W. C. Mackrodt, M. J. Norgett, and A. M. Stoneham, "The basic atomic processes of corrosion I. Electronic conduction in MnO, CoO, NiO," *Philos. Mag. A*, vol. 35, no. 1, pp. 177–187, 1977.

[133] C. R. A. Catlow, K. M. Diller, and M. J. Norgett, "Interionic potentials for alkali halides," *J. Phys. C*, vol. 10, no. 9, pp. 1395–1412, 1977.

[134] C. R. A. Catlow, C. M. Freeman, M. S. Islam, R. A. Jackson, M. Leslie, and S. M. Tomlinson, "Interatomic potentials for oxides," *Philos. Mag. A*, vol. 58, pp. 123–141, 1988.

[135] J. D. Gale, "Empirical potential derivation for ionic materials," *Philos. Mag. B*, vol. 73, no. 1, pp. 3–19, 1996.

[136] J. Gale, "GULP (General Utility Lattice Program)," *R. Institution, London*, 1992.

[137] C. J. Pickard and R. J. Needs, "Ab initio random structure searching," *J. Phys. Condens. Matter*, vol. 23, no. 5, p. 053201, 2011.

[138] R. J. Nicholls, N. Ni, S. Lozano-Perez, A. London, D. W. McComb, P. D. Nellist, C. R. Grovenor, C. J. Pickard, and J. R. Yates, "Crystal Structure of the ZrO Phase at Zirconium/Zirconium Oxide Interfaces," *Adv. Eng. Mater.*, vol. 17, no. 2, pp. 211–215, 2015.

[139] G. Schusteritsch and C. J. Pickard, "Predicting interface structures: From Sr-TiO3 to graphene," *Physical Review B - Condensed Matter and Materials Physics*, vol. 90, no. 3, pp. 1–7, 2014.

[140] P. W. Tasker and D. M. Duffy, "On the structure of twist grain boundaries in ionic oxides," *Phil. Mag. A*, vol. 47, pp. L45–L48, 1983.

[141] P. W. Duffy, D. M.; Tasker, "Computer simulation of 001 tilt grain boundaries in nickel oxide," *Philos. Mag. A*, vol. 47, pp. 817–825, 1983.

[142] P. W. Duffy, D. M.; Tasker, "Computer simulation of 001 tilt grain boundaries in nickel oxide," *Philos. Mag. A*, vol. 47, pp. 817–825, 1983.

[143] J. Harding and C. Noguera, "Empirical and ab initio local-density approximation studies of an MgO(100) twist grain boundary," *Philos. Mag. Lett.*, vol. 77, no. 6, pp. 315–320, 1998.

[144] J. Harding, D. Harris, and S. Parker, "Computer simulation of general grain boundaries in rocksalt oxides," *Phys. Rev. B*, vol. 60, no. 4, pp. 2740–2746, 1999.

[145] D. J. Harris, G. W. Watson, and S. C. Parker, "Atomistic simulation of the effect of temperature and pressure on the [001] symmetric tilt grain boundaries of MgO," *Philos. Mag. A*, vol. 74, no. 2, pp. 407–418, 1996.

[146] B. B. Karki, L. Stixrude, S. J. Clark, M. C. Warren, G. J. Ackland, and J. Crain, "Structure and elasticity of MgO at high pressure," *American Mineralogist*, vol. 82, no. 1-2, pp. 51–60, 1997.

[147] J. Jaffe, J. Snyder, Z. Lin, and A. Hess, "LDA and GGA calculations for high-pressure phase transitions in ZnO and MgO," *Phys. Rev. B*, vol. 62, no. 3, pp. 1660–1665, 2000.

[148] X.-Y. Sun, V. Taupin, P. Cordier, C. Fressengeas, and B. Karki, "Influence of pressure on dislocation, disclination, and generalized-disclination structures of a {310}/[001] tilt grain boundary in MgO," *Journal of Materials Research*, vol. 31, no. 20, 2016.

[149] D. Harris, G. Watson, and S. Parker, "Vacancy migration at the {410}/[001] symmetric tilt grain boundary of MgO: An atomistic simulation study," *Phys. Rev. B*, vol. 56, no. 18, pp. 11477–11484, 1997.

[150] B. P. Uberuaga, X.-M. Bai, P. P. Dholabhai, N. Moore, and D. M. Duffy, "Point defectgrain boundary interactions in MgO: an atomistic study," *J. Phys. Condens. Matter.*, vol. 25, no. 35, p. 355001, 2013.

[151] D. Sayle, C. Catlow, N. Dulamita, M. Healy, S. Maicaneanu, B. Slater, and G. Watson, *Molecular Simulation*, vol. 28. Taylor and Francis, 2002.

[152] D. C. Sayle and G. W. Watson, "The atomistic structure of an MgO cluster, supported on BaO, synthesized using simulated amorphization and recrystallization," *J. Phys. Chem. B*, vol. 106, no. 15, pp. 3916–3925, 2002.

[153] D. C. Sayle and G. W. Watson, "Structural exploration of thin-film oxide interfaces via 'simulated amorphization and recrystallization'," *Surf. Sci.*, vol. 473, no. 1-2, pp. 97–107, 2001.

[154] D. C. Sayle, "The predicted 3-D atomistic structure of an interfacial screwedge dislocation," *J. Mater. Chem.*, vol. 9, no. 12, pp. 2961–2964, 1999.

[155] S. M. Woodley, P. D. Battle, J. D. Gale, and C. Richard A. Catlow, "The prediction of inorganic crystal structures using a genetic algorithm and energy minimisation," *Phys. Chem. Chem. Phys.*, vol. 1, no. 10, pp. 2535–2542, 1999.

[156] A. L.-S. Chua, N. A. Benedek, L. Chen, M. W. Finnis, and A. P. Sutton, "A genetic algorithm for predicting the structures of interfaces in multicomponent systems," *Nat. Mater.*, vol. 9, no. 5, pp. 418–422, 2010.

[157] F. Ercolessi and J. B. Adams, "Interatomic Potentials from First-Principles Calculations :," *Europhys. Lett.*, vol. 26, no. 8, pp. 583–588, 1994.

[158] J. Sarsam, M. W. Finnis, and P. Tangney, "Atomistic force field for alumina fit to density functional theory," *Journal of Chemical Physics*, vol. 139, no. 20, 2013.

[159] J. Purton, D. M. Bird, S. C. Parker, and D. W. Bullett, "Comparison of atomistic simulations and pseudopotential calculations of the MgO{100}/Ag{100} and MgO{110}/Ag{110} interfaces," *The Journal of Chemical Physics*, vol. 110, no. 16, pp. 8090–8097, 1999.

[160] T. Bredow and A. Gerson, "Effect of exchange and correlation on bulk properties of MgO, NiO, and CoO," *Phys. Rev. B*, vol. 61, no. 8, pp. 5194–5201, 2000.

[161] H. Guhl, H.-S. Lee, P. Tangney, W. Foulkes, A. H. Heuer, T. Nakagawa, Y. Ikuhara, and M. W. Finnis, "Structural and electronic properties of $\Sigma 7$ grain boundaries in α-Al2O3," *Acta Mater.*, vol. 99, pp. 16–28, 2015.

[162] S. K. Wallace and K. P. McKenna, "Grain boundary controlled electron mobility in polycrystalline titanium dioxide," *Adv. Mater. Interfaces*, vol. 1, no. 5, p. 1400078, 2014.

[163] K. McKenna and A. Shluger, "The interaction of oxygen vacancies with grain boundaries in monoclinic HfO_2," *Appl. Phys. Lett.*, vol. 95, no. 22, pp. 8–11, 2009.

[164] K. P. McKenna and A. L. Shluger, "Microelectronic Engineering Electronic properties of defects in polycrystalline dielectric materials," *Microelectronic Engineering*, vol. 86, no. 7-9, pp. 1751–1755, 2009.

[165] S. Benedetti, P. Torelli, S. Valeri, H. M. Benia, N. Nilius, and G. Renaud, "Structure and morphology of thin MgO films on Mo(001)," *Phys. Rev. B*, vol. 78, no. 19, pp. 1–8, 2008.

[166] H. Benia, P. Myrach, N. Nilius, and H.-J. Freund, "Structural and electronic characterization of the MgO/Mo(001) interface using STM," *Surf. Sci.*, vol. 604, no. 3-4, pp. 435–441, 2010.

[167] S. Fischer, A. W. Munz, K. D. Schierbaum, and W. Göpel, "The geometric structure of intrinsic defects at TiO_2(110) surfaces: an STM study," *Surface Science*, vol. 337, no. 1-2, pp. 17–30, 1995.

[168] H. Onishi and Y. Iwasawa, "STM-imaging of formate intermediates adsorbed on a TiO_2(110) surface," *Chem. Phys. Lett.*, vol. 226, no. 1-2, pp. 111–114, 1994.

[169] F. H. Jones, K. Rawlings, J. S. Foord, R. G. Egdell, J. B. Pethica, B. M. R. Wanklyn, S. C. Parker, and P. M. Oliver, "An STM study of surface structures on WO3(001)," *Surf. Sci.*, vol. 359, no. 13, pp. 107–121, 1996.

[170] C. P. Sun and R. W. Balluffi, "Observation of intrinsic and extrinsic secondary grain boundary dislocations in [001] high angle twist boundaries in MgO," *Scripta Metallurgica*, vol. 13, no. 8, pp. 757–761, 1979.

[171] H. Mykura, P. S. Bansal, and M. H. Lewis, "Coincidence-site-lattice relations for MgO-CdO interfaces," *Philos. Mag.*, vol. 42, no. 2, pp. 225–233, 1980.

[172] C. P. Sun and R. W. Balluffi, "Secondary grain boundary dislocations in [001] twist boundaries in MgO II. Extrinsic structures," *Philos. Mag. A*, vol. 46, no. 1, pp. 63–73, 1982.

[173] M. Arita, Y. Okubo, K. Hamada, and Y. Takahashi, "Tunnel current measurement of MgO and MgO/Fe/MgO nanoregions during TEM observation," *Superlattices Microstruct.*, vol. 44, no. 4-5, pp. 633–640, 2008.

[174] V. Harnchana, A. T. Hindmarch, A. P. Brown, R. M. Brydson, and C. H. Marrows, "TEM investigation of MgO thin films for magnetic tunnel junction application," *J. Phys. Conf. Ser.*, vol. 241, p. 012039, 2010.

[175] V. Serin, S. Andrieu, R. Serra, F. Bonell, C. Tiusan, L. Calmels, M. Varela, S. J. Pennycook, E. Snoeck, M. Walls, and C. Colliex, "TEM and EELS measurements of interface roughness in epitaxial Fe/MgO/Fe magnetic tunnel junctions," *Phys. Rev. B*, vol. 79, no. 14, pp. 1–7, 2009.

[176] R. F. Egerton, "Electron energy-loss spectroscopy in the TEM," *Rep. Prog. Phys.*, vol. 72, no. 1, p. 016502, 2008.

[177] Y. Yan, M. Chisholm, G. Duscher, A. Maiti, S. Pennycook, and S. Pantelides, "Impurity-Induced Structural Transformation of a MgO Grain Boundary," *Phys. Rev. Lett.*, vol. 81, no. 17, pp. 3675–3678, 1998.

[178] H. L. Meyerheim, R. Popescu, J. Kirschner, N. Jedrecy, M. Sauvage-Simkin, B. Heinrich, and R. Pinchaux, "Geometrical and Compositional Structure at Metal-Oxide Interfaces: MgO on Fe(001)," *Phys. Rev. Lett.*, vol. 87, no. 7, p. 076102, 2001.

[179] S. G. Wang, G. Han, G. H. Yu, Y. Jiang, C. Wang, A. Kohn, and R. C. C. Ward, "Evidence for FeO formation at the Fe/MgO interface in epitaxial TMR structure by X-ray photoelectron spectroscopy," *J. Magn. Magn. Mater.*, vol. 310, no. 2 SUPPL. PART 3, pp. 1935–1936, 2007.

[180] M. James and T. Hibma, "Thickness-dependent relaxation of NiO(001) overlayers on MgO(001) studied by X-ray diffraction," *Surf. Sci.*, vol. 433-435, pp. 718–722, 1999.

[181] L. B. Levitin and T. Toffoli, "Fundamental limit on the rate of quantum dynamics: The unified bound is tight," *Phys. Rev. Lett.*, vol. 103, no. 16, pp. 1–4, 2009.

[182] P. Bauer, A. Thorpe, and G. Brunet, "The quiet revolution of numerical weather prediction," *Nature*, vol. 525, no. 7567, pp. 47–55, 2015.

[183] M. W. Macy and R. Willer, "From Factors to Factors: Computational Sociology and Agent-Based Modeling," *Annu. Rev. Sociol.*, vol. 28, no. 1, pp. 143–166, 2002.

[184] L. Tesfatsion, "Agent-Based Computational Economics Growing Economies from the Bottom Up," *Artificial Life*, no. 2002, pp. 1–5, 2002.

[185] V. Brázdová and D. R. Bowler, *Atomistic computer simulations: a practical guide*. John Wiley & Sons, 2013.

[186] J. Aarons, "A New CASTEP and ONETEP Geometry Optimiser," *Numerical Algorithms Group*, pp. 1–22, 2011.

[187] J. E. Jones, "On the Determination of Molecular Fields. II. From the Equation of State of a Gas," *Proc. R Soc. Lond. A Math. Phys. Sci.*, vol. 106, no. 738, pp. 463–477, 1924.

[188] J. E. Jones, "On the Determination of Molecular Fields. I. From the Variation of the Viscosity of a Gas with Temperature," *Proc. R Soc. Lond. A Math. Phys. Sci.*, vol. 106, no. 738, pp. 441–462, 1924.

[189] J. E. Jones, "On the Determination of Molecular Fields. III. From Crystal Measurements and Kinetic Theory Data," *Proc. R Soc. Lond. A Math. Phys. Sci.*, vol. 106, no. 740, pp. 709–718, 1924.

[190] T. Haliciolu and G. M. Pound, "Calculation of Potential Energy Parameters from Crystalline State Properties," *Physica Status Solidi. A Appl. Res.*, vol. 30, p. 619, 1975.

[191] D. V. Matyushov and R. Schmid, "Calculation of Lennard-Jones energies of molecular fluids," *Journal of Chemical Physics*, vol. 104, pp. 8627–8638, 1996.

[192] G. Lewis and C. Catlow, "Potential models for ionic oxides," *J. Phys. C*, vol. 1149, 1985.

[193] C. R. A. Catlow and M. J. Norgett, "Shell model calculations of the energies of formation of point defects in alkaline earth fluorides," *J. Phys. C*, vol. 6, no. 8, pp. 1325–1339, 1973.

[194] J. D. Gale, "Empirical potential derivation for ionic materials," *Philos. Mag. B*, vol. 73, no. 1, pp. 3–19, 1996.

[195] C. R. A. Catlow, K. M. Diller, and M. J. Norgett, "Interionic potentials for alkali halides," *J. Phys. C*, vol. 10, no. 9, pp. 1395–1412, 1977.

[196] G. V. Lewis and C. R. a. Catlow, "Potential models for ionic oxides," *J. Phys. C*, vol. 18, no. 6, pp. 1149–1161, 2000.

[197] F. Jensen, *Introduction to computational chemistry.* John Wiley & sons, 2017.

[198] P. Hohenberg and W. Kohn, "The Inhomogeneous Electron Gas," *Phys. Rev.*, vol. 136, p. B864, 1964.

[199] W. Kohn and L. J. Sham, "Self Consistent Equations Including Exchange and Correlation Effects," *Phys. Rev.*, vol. 385, pp. A1133–A1138, 1965.

[200] J. P. Perdew, K. Burke, and M. Ernzerhof, "Generalized gradient approximation made simple," *Phys. Rev. Lett.*, vol. 77, no. 18, p. 3865, 1996.

[201] J. Heyd, G. E. Scuseria, and M. Ernzerhof, "Hybrid functionals based on a screened Coulomb potential," *Journal of Chemical Physics*, vol. 118, no. 18, pp. 8207–8215, 2003.

[202] J. Paier, M. Marsman, K. Hummer, G. Kresse, I. C. Gerber, and J. G. Angyán, "Screened hybrid density functionals applied to solids," *Journal of Chemical Physics*, vol. 124, no. 15, 2006.

[203] S. Clark, "Complex Structures In Tetrahedrally Bonded Semiconductors," 1994.

[204] P. Monachesi, A. Marini, G. Onida, M. Palummo, and R. Del Sole, "All-electron versus pseudopotential calculation of optical properties: The case of GaAs," *Physica Status Solidi. A Appl. Res.*, vol. 184, no. 1, pp. 101–104, 2001.

[205] R. F. Bader, *Atoms in molecules.* Wiley Online Library, 1990.

[206] S. J. Clark, M. D. Segall, C. J. Pickard, P. J. Hasnip, M. I. J. Probert, K. Refson, and M. C. Payne, "First principles methods using CASTEP," *Zeitschrift fur Krist.*, vol. 220, pp. 567–570, 2005.

[207] G. Kresse and J. Hafner, "Ab initio molecular dynamics for liquid metals," *Phys. Rev. B*, vol. 47, no. 1, pp. 558–561, 1993.

[208] S. Plimpton, "Fast Parallel Algorithms for Short-Range Molecular Dynamics," *Journ. Comp. Phys.*, vol. 117, no. June 1994, pp. 1–19, 1995.

[209] "National institute of standards and technology." `http://www.ctcms.nist.gov/potentials/`. Accessed: 2013-12-30.

[210] K. Momma and F. Izumi, "Vesta 3 for three-dimensional visualization of crystal, volumetric and morphology data," *J. Appl. Crystallogr.*, vol. 44, no. 6, pp. 1272–1276, 2011.

[211] W. Humphrey, A. Dalke, and K. Schulten, "VDM: visual molecular dynamics.," *J. Mol. Graph.*, vol. 14, no. 1, pp. 33–8, plates, 27–28, 1996.

[212] G. Henkelman, A. Arnaldsson, and H. Jónsson, "A fast and robust algorithm for Bader decomposition of charge density," *Comp. Mater. Sci.*, vol. 36, no. 3, pp. 354–360, 2006.

[213] H. Bolt, V. Barabash, W. Krauss, J. Linke, R. Neu, S. Suzuki, and N. Yoshida, "Materials for the plasma-facing components of fusion reactors," *J. Nucl. Mater.*, vol. 329-333, pp. 66–73, 2004.

[214] I. Bergenti, V. Dediu, M. Cavallini, E. Arisi, A. Riminucci, and C. Taliani, "Properties of thin manganite films grown on semiconducting substrates for spintronics applications," *Curr. Appl. Phys.*, vol. 7, no. 1, pp. 47–50, 2007.

[215] B. Poudel, Q. Hao, Y. Ma, Y. Lan, A. Minnich, B. Yu, X. Yan, D. Wang, A. Muto, D. Vashaee, X. Chen, J. Liu, M. S. Dresselhaus, G. Chen, and Z. Ren, "High-thermoelectric performance of nanostructured bismuth antimony telluride bulk alloys.," *Science*, vol. 320, no. 5, pp. 634–638, 2008.

[216] S. J. Zinkle and J. T. Busby, "Structural materials for fission & fusion energy," *Mater. Today*, vol. 12, no. 11, pp. 12–19, 2009.

[217] M. Shiga, M. Yamaguchi, and H. Kaburaki, "Structure and energetics of clean and hydrogenated Ni surfaces and symmetrical tilt grain boundaries using the embedded-atom method," *Phys. Rev. B*, vol. 68, no. 24, p. 245402, 2003.

[218] F. Birch, "Finite elastic strain of cubic crystals," *Phys. Rev.*, vol. 71, no. 11, pp. 809–824, 1947.

[219] S. J. Clark, M. D. Segall, C. J. Pickard, P. J. Hasnip, M. I. J. Probert, K. Refson, and M. C. Payne, "First principles methods using CASTEP," *Zeitschrift für Krist.*, vol. 220, pp. 567–570, 2005.

[220] R. H. Byrd, J. Nocedal, and R. B. Schnabel, "Representations of quasi-Newton matrices and their use in limited memory methods," *Math. Program.*, vol. 63, pp. 129–156, 1994.

[221] C. Kittel, "Introduction to Solid State Physics," *Am. J. Phys.*, vol. 35, no. 6, p. 547, 1967.

[222] W. B. Pearson, *A handbook of lattice spacings and structures of metals and alloys*. Elsevier (Republished 2013), 1967.

[223] W. Gale and T. Totemeier, *Smithells metals reference book*. Butterworth-Heinemann, 2003.

[224] H. Ledbetter and E. Naimon, "Elastic properties of metals and alloys. ii. copper," *J. Phys. HYS Chem. Ref. Data.*, vol. 3, no. 4, pp. 897–935, 1974.

[225] H. Ledbetter and R. P. Reed, "Elastic properties of metals and alloys, i. iron, nickel, and iron-nickel alloys," *J. Phys. HYS Chem. Ref. Data.*, vol. 2, no. 3, pp. 531–618, 1973.

[226] J. Rayne and B. Chandrasekhar, "Elastic constants of iron from 4.2 to 300 K," *Phys. Rev.*, vol. 122, no. 1960, pp. 1714–1716, 1961.

[227] P. Taylor, "Erratum," *Philos. Mag. A*, vol. 53, no. 1, pp. 161–161, 1986.

[228] M. I. Mendelev, S. Han, D. J. Srolovitz, G. J. Ackland, D. Y. Sun, and M. Asta, "Development of new interatomic potentials appropriate for crystalline and liquid iron," *Philos. Mag.*, vol. 83, no. 35, pp. 3977–3994, 2003.

[229] R. A. Johnson, "Analytic nearest-neighbor model for fcc metals," *Phys. Rev. B*, vol. 37, no. 8, pp. 3924–3931, 1988.

[230] H. Jang and D. Farkas, "Interaction of lattice dislocations with a grain boundary during nanoindentation simulation," *Mater. Lett.*, vol. 61, no. 3, pp. 868–871, 2007.

[231] F. Berthier, B. Legrand, and G. Tréglia, "New structures and atomistic analysis of the polymorphism for the $\Sigma = 5$ (210) [001] tilt boundary," *Interface Sci.*, vol. 8, pp. 55–69, 2000.

[232] M. Sørensen, Y. Mishin, and A. Voter, "Diffusion mechanisms in Cu grain boundaries," *Phys. Rev. B*, vol. 62, no. 6, pp. 3658–3673, 2000.

[233] A. Suzuki and Y. Mishin, "Atomistic modeling of point defects and diffusion in copper grain boundaries," *Interface Sci.*, vol. 11, pp. 131–148, 2003.

[234] N. Gao, C. C. Fu, M. Samaras, R. Schäublin, M. Victoria, and W. Hoffelner, "Multiscale modelling of bi-crystal grain boundaries in bcc iron," *J. Nucl. Mater.*, vol. 385, no. 2, pp. 262–267, 2009.

[235] D. Terentyev and X. He, "Dimensionality of interstitial He migration in $\langle 110 \rangle$ tilt grain boundaries in α-Fe," *Comput. Mater. Sci.*, vol. 49, no. 4, pp. 858–864, 2010.

[236] T. Frolov, D. L. Olmsted, M. Asta, and Y. Mishin, "Structural phase transformations in metallic grain boundaries," *Nat. Commun.*, vol. 4, p. 1899, 2013.

[237] D. L. Olmsted, S. M. Foiles, and E. A. Holm, "Survey of computed grain boundary properties in face-centered cubic metals: I. Grain boundary energy," *Acta Mater.*, vol. 57, no. 13, pp. 3694–3703, 2009.

[238] L. Lim and R. Raj, "On the distribution of Σ for grain boundaries in polycrystalline nickel prepared by strainannealing technique," *Acta Metall.*, vol. 32, no. 8, pp. 1177–1181, 1984.

165

[239] V. Y. Gertsman, M. Janecek, and K. Tangri, "Grain boundary ensembles in polycrystals," *Acta Mater.*, vol. 44, no. 7, pp. 2869–2882, 1996.

[240] D. M. Saylor, B. S. El Dasher, A. D. Rollett, and G. S. Rohrer, "Distribution of grain boundaries in aluminum as a function of five macroscopic parameters," *Acta Mater.*, vol. 52, no. 12, pp. 3649–3655, 2004.

[241] E. A. Holm, G. S. Rohrer, S. M. Foiles, A. D. Rollett, H. M. Miller, and D. L. Olmsted, "Validating computed grain boundary energies in fcc metals using the grain boundary character distribution," *Acta Mater.*, vol. 59, no. 13, pp. 5250–5256, 2011.

[242] L. L. Kazmerski, "Photovoltaics: A review of cell and module technologies," *Renewable and Sustainable Energy Reviews*, vol. 1, no. 1-2, pp. 71–170, 1997.

[243] G. n. Steinmeyer, "A review of ultrafast optics and optoelectronics," *J. Opt. A: Pure and Applied Optics*, vol. 5, pp. R1–R15, 2002.

[244] A. Kolmakov and M. Moskovits, "Chemical Sensing and Catalysis By One-Dimensional Metal-Oxide Nanostructures," *Annu. Rev. Mater. Res.*, vol. 34, no. 1, pp. 151–180, 2004.

[245] S. E. Thompson and S. Parthasarathy, "Moore's law: the future of Si microelectronics," *Mater. Today*, vol. 9, no. 6, pp. 20–25, 2006.

[246] S. Ziegler, R. C. Woodward, H. H.-C. Iu, and L. J. Borle, "Current Sensing Techniques: A Review," *IEEE Sensors Journal*, vol. 9, no. 4, pp. 354–376, 2009.

[247] S. Bader and S. Parkin, "Spintronics," *Annu. Rev. Conden. Ma. P.*, vol. 1, no. 1, pp. 71–88, 2010.

[248] W. J. Gallagher and S. S. P. Parkin, "Development of the magnetic tunnel junction MRAM at IBM: From first junctions to a 16-Mb MRAM demonstrator chip," *IBM Journal of Research and Development*, vol. 50, no. 1, pp. 5–23, 2006.

[249] W. Butler, X.-G. Zhang, T. Schulthess, and J. MacLaren, "Spin-dependent tunneling conductance of Fe—MgO—Fe sandwiches," *Phys. Rev. B*, vol. 63, no. 5, pp. 1–12, 2001.

[250] V. Sokalski, D. M. Bromberg, M. T. Moneck, E. Yang, and J. G. Zhu, "Increased perpendicular TMR in FeCoB/MgO/FeCoB magnetic tunnel junctions by seed-layer modifications," *IEEE Trans. Magn.*, vol. 49, no. 7, pp. 4383–4385, 2013.

[251] D. D. Djayaprawira, K. Tsunekawa, M. Nagai, H. Maehara, S. Yamagata, N. Watanabe, S. Yuasa, Y. Suzuki, and K. Ando, "230% room-temperature magnetoresistance in CoFeB/MgO/CoFeB magnetic tunnel junctions," *Appl. Phys. Lett.*, vol. 86, no. 9, pp. 1–3, 2005.

[252] J. Mathon and A. Umerski, "Theory of tunneling magnetoresistance of an epitaxial Fe/MgO/Fe(001) junction," *Phys. Rev. B*, vol. 63, no. 22, p. 220403, 2001.

[253] Y. Lu, C. Deranlot, A. Vauré, F. Petroff, J. M. George, Y. Zheng, and D. Demailles, "Effects of a thin Mg layer on the structural and magnetoresistance properties of CoFeB/MgO/CoFeB magnetic tunnel junctions," *Appl. Phys. Lett.*, vol. 91, no. 22, pp. 2005–2008, 2007.

[254] R. Ishikawa, E. Okunishi, H. Sawada, Y. Kondo, F. Hosokawa, and E. Abe, "Direct imaging of hydrogen-atom columns in a crystal by annular bright-field electron microscopy.," *Nat. Mater.*, vol. 10, no. 4, pp. 278–281, 2011.

[255] S. D. Findlay, N. Shibata, H. Sawada, E. Okunishi, Y. Kondo, and Y. Ikuhara, "Dynamics of annular bright field imaging in scanning transmission electron microscopy," *Ultramicroscopy*, vol. 110, no. 7, pp. 903–923, 2010.

[256] R. W. G. Wyckoff, *Crystal Structures*, vol. 3. Interscience Publishers, 1961.

[257] J. N. Plendl, S. S. Mitra, and P. J. Gielisse, "Compressibility, Cohesive Energy, and Hardness of Non???Metallic Solids," *Phys. Status Solidi B Basic Solid State Phys.*, vol. 12, no. 1, pp. 367–374, 1965.

[258] O. L. Anderson and P. Andreatch, "Pressure Derivatives of Elastic Constants of SingleCrystal MgO at 23 and 195.8C," *Journal of the American Ceramic Society*, vol. 49, no. 8, pp. 404–409, 1966.

[259] G. Kresse, "Efficient iterative schemes for ab initio total-energy calculations using a plane-wave basis set," *Phys. Rev. B*, vol. 54, no. 16, pp. 11169–11186, 1996.

[260] P. E. Blöchl, "Projector augmented-wave method," *Phys. Rev. B*, vol. 50, no. 24, pp. 17953–17979, 1994.

[261] D. M. Roessler and W. C. Walker, "Electronic spectrum and ultraviolet optical properties of crystalline MgO," *Phys. Rev.*, vol. 159, no. 3, pp. 733–738, 1967.

[262] D. J. Monsma and S. S. P. Parkin, "Spin polarization of tunneling current from ferromagnet/Al_2O_3 interfaces using copper-doped aluminum superconducting films," *Appl. Phys. Lett.*, vol. 77, no. 5, p. 720, 2000.

[263] K. P. McKenna and A. L. Shluger, "Electron-trapping polycrystalline materials with negative electron affinity.," *Nat. Mater.*, vol. 7, no. 11, pp. 859–62, 2008.

[264] S. Yuasa, A. Fukushima, H. Kubota, Y. Suzuki, and K. Ando, "Giant tunneling magnetoresistance up to 410% at room temperature in fully epitaxial Co/MgO/Co magnetic tunnel junctions with bcc Co(001) electrodes," *Appl. Phys. Lett.*, vol. 89, no. 4, pp. 87–90, 2006.

[265] S. Yuasa and D. D. Djayaprawira, "Giant tunnel magnetoresistance in magnetic tunnel junctions with a crystalline MgO(001) barrier," *J. Phys. D*, vol. 40, no. 21, pp. R337–R354, 2007.

[266] B. D. Yu and J. S. Kim, "Ab initio study of ultrathin MgO films on Fe(001): Influence of interfacial structures," *Phys. Rev. B*, vol. 73, no. 12, pp. 2–5, 2006.

[267] D. Waldron, V. Timoshevskii, Y. Hu, K. Xia, and H. Guo, "First principles modeling of tunnel magnetoresistance of Fe/MgO/Fe trilayers," *Phys. Rev. Lett.*, vol. 97, no. 22, pp. 1–4, 2006.

[268] X. Feng, O. Bengone, M. Alouani, S. Lebègue, I. Rungger, and S. Sanvito, "Effects of structural relaxation on calculations of the interface and transport properties of Fe/MgO(001) tunnel junctions," *Phys. Rev. B*, vol. 79, no. 17, pp. 1–5, 2009.

[269] M. E. Schrader, "Young-Dupre Revisited," *Langmuir*, vol. 11, no. 9, pp. 3585–3589, 1995.

[270] Y. Luo and J. Kerr, "Bond dissociation energies," *CRC Handbook of Chemistry and Physics*, pp. 65–98, 2007.

[271] J.-l. Cao, S. Ogata, and W. T. Geng, "Volume Contraction at a Grain Boundary in Vanadium," *Unpublished*, vol. C, pp. 1–14, 2016.

[272] C. Y. Wang, H. Han, D. Wickramaratne, W. Zhang, H. Wang, X. X. Ye, Y. L. Guo, K. Shao, and P. Huai, "Diffusion of tellurium at nickel grain boundaries: a first-principles study," *RSC Adv.*, vol. 7, no. 14, pp. 8421–8428, 2017.

[273] J. A. Kotzurek, W. Sprengel, M. Krystian, S. Simic, P. Pölt, A. Hohenwarter, R. Pippan, and R. Würschum, "Structural anisotropy in equal-channel angular extruded nickel revealed by dilatometric study of excess volume," *Int. J. Mater. Res.*, vol. 108, no. 2, pp. 81–88, 2017.

[274] X. Wu, X.-S. Kong, Y.-W. You, W. Liu, C. S. Liu, J.-L. Chen, and G.-N. Luo, "Effect of transition metal impurities on the strength of grain boundaries in vanadium," *J. Appl. Phys.*, vol. 120, no. 9, p. 095901, 2016.

[275] J. Han, V. Vitek, and D. J. Srolovitz, "The grain-boundary structural unit model redux," *Acta Mater.*, vol. 133, pp. 186–199, 2017.

Physics Family Tree

Below is a pictorial representation of PhD supervisors who are connected to me.

Friedrich Leibniz (German: 1597- 1652) [University of Leipzig]

Jakob Thomasius (German: 27.08.1622 - 9.09.1684) [University of Leipzig]

Otto Mencke (German: 22.03.1644 - 18.01.1707) [University of Leipzig]

Johann Christoph Wichmannshausen (German: 1663 - 1727) [University of Wittenberg]

Christian August Hausen (German: 1693 - 1743) [University of Leipzig]

Abraham Gotthelf Kästner (German: 27.09.1719 - 20.06.1800) [University of Göttingen]

Johann Friedrich Pfaff (German: 22.12.1765 - 21.04.1825) [Halle University]

Carl Friedrich Gauss (German: 30.04.1777 - 23.02.1855) [University of Göttingen]

Christoph Gudermann (German: 25.03.1798 - 25.09.1852) [Münster Academy]

Karl Weierstrass (German: 31.10.1815 - 19.02.1897) [Gewerbeinstitut]

Carl Runge (German: 30.08.1856 - 03.01.1927) [University of Göttingen (1904-1925)]

Max Born (German: 11.12.1882 - 05.01.1970) [University of Edinburgh]

Maria Goeppert-Mayer

Pascual Jordan

Friedrich Hund

Robert Oppenheimer

Anatole Abragam

John Clive Ward

Maurice Pryce [British: 24.01.1913 - 24.07.2003] [University of Oxford]

Roger Elliot

Kenneth Stevens [British: 17.09.1922 - 16.07.2010] [University of Nottingham]

Jaime Keller

John Ziman [New Zealander: 16.05.1925 - 2.01.2005] [University of Bristol]

Brian Hickey

Gwynne Morgan [British: ? - Now] [University of Leeds]

Adam Kerrigan

Bazak El-Mashmure

Keith McKenna [British: ? - Now] [University of York]

Shibi Isnan

Jonathan Bean

Figure 7.1: My Physics PhD family :)